Chapter 3

VERTICAL LOADING OF SKIRTED FOUNDATIONS IN SAND

Abstract

The study of the relationship between the vertical load and the vertical displacement in soil-footing interaction problems is essential, not only from the vertical capacity point of view but, also to solve combined loading capacity problems. The bearing capacity formulation is used to analyse the failure of skirted footings tested under pure vertical load. It was found that bearing capacity increases with the length of the footing skirt. Axial symmetric bearing capacity factors for flat footings were used. The depth effect did not affect significantly the surcharge bearing capacity factor N_q for caisson aspect ratios below one. However, the weight bearing capacity factor N_γ increased considerably with the caisson aspect ratio. Finally, the development of a hardening law was pursued, proving that the use of a three term hyperbola gives a good agreement with experimental results in loose sand. For dense sands a formulation is proposed, which is able to reproduce hardening after peak and softening response.

3.1 INTRODUCTION

The investigation of the vertical capacity of skirted footings has two main objectives. The first is the determination of the ultimate bearing capacity under pure vertical load, and the second is the formulation of a hardening law for plasticity analysis. Although low vertical loads are expected owing to the light weight of wind turbines, as explained in Chapter 1, smaller caissons as part of tripod or tetrapod configurations can experience much larger vertical loads than in monopod caissons. Furthermore, in this study it was of particular interest to provide a complete insight into the different phases of loading that a skirted footing undergoes under the application of a monotonically increasing vertical load until failure and beyond.

A series of tests performed to investigate the load-penetration response of seven skirted footings on dry sand, covering loose and dense samples, is presented in Villalobos *et al.* (2003a). A preliminary analysis of these experimental results was carried out Byrne *et al.* (2003). Figure 3.1 shows two test results as examples where it is possible to define three phases in the $h - V'$ curves. The upper curve corresponds to caisson F_5 which is loaded into a dense sample of Leighton Buzzard sand. The lower curve corresponds to the same caisson, but in a very loose sample of Dogs Bay sand. Phase A represents the *installation* of the caisson, in which only the end bearing forces over the tip and the frictional forces along the external and internal walls of the caisson skirt are involved. Phase B corresponds to the development of the *bearing capacity* of the whole caisson, *i.e.* after the skirt wall inside the footing has fully penetrated the ground and simultaneously the caisson lid contacts the soil. The departure from phase A to B can be clearly observed in both curves, where dashed circles show the contact penetration h_c and the contact load V_c. Note that the onset of phase B differs, whilst for the caisson in a loose sample the *contact penetration*, occurred at a value close to the skirt length $h_c = L$, of 51 mm, for the caisson in the dense sample this occurred for h_c of 42 mm (though inside the caisson the skirt is embedded a depth L). This difference is caused by the formation of a soil plug which in dense sands raises above the mudline level during skirt penetration.

The penetration forces the dense packing of grains (low specific volume) around the skirt to rearrange. Due to the rearrangement grains shear each other to a level that dilates the sand, therefore, the initial low specific volume increases. Moreover, the phenomenon of dilatancy becomes more pronounced at low stresses. Subsequently, Figure 3.1 shows that in the dense sample *failure* can be recognised as a peak load is reached, whereas for the caisson in the loose sample the definition of failure is not straightforward. A dashed circle indicates a section where failure is assumed due to foundation stiffness reduction (definition and determination is presented in section §3.3.1). Finally, phase C defines *post failure* behaviour of the foundation where, despite previous failure, capacity increases as additional large penetration occurs. Note the complex response sequence after the peak load; further grains arrangements cause a short relaxation and softening followed by a final hardening.

The installation part (phase A) will be the subject of Chapter 4, whereas parts B and C are the theme of this chapter. However, measured heave caused by pushed installation has been included.

An initial interest in the study of bearing capacity was to assess the proximity of the vertical load required to install a caisson V_c, to the failure load. Despite the very different type of sands chosen, Figure 3.1 shows that in the dense sand the caisson failed at a load almost seven times V_c, and in the loose sand failure occurred at a load almost four times V_c.

Bearing capacity calculations of 'rigid' flat footings are based on the assumption of failure mechanisms. The same type of failure mechanisms may be assumed for skirted footings. But, the soil enclosed by the skirt acts as a flexible 'cushion' instead of being a rigid block. However, there are not as yet analytical solutions for this particular case, therefore, the bearing capacity has to be obtained from calculation procedures for rigid flat footings. Even though solutions for the flat footing problem, proposed by Terzaghi (1943), Meyerhof (1963), Brinch Hansen (1970) and Vesic (1975), are available in the majority of foundation engineering textbooks (Bowles, 1996; Craig, 1998; McCarthy, 1998; Tom-

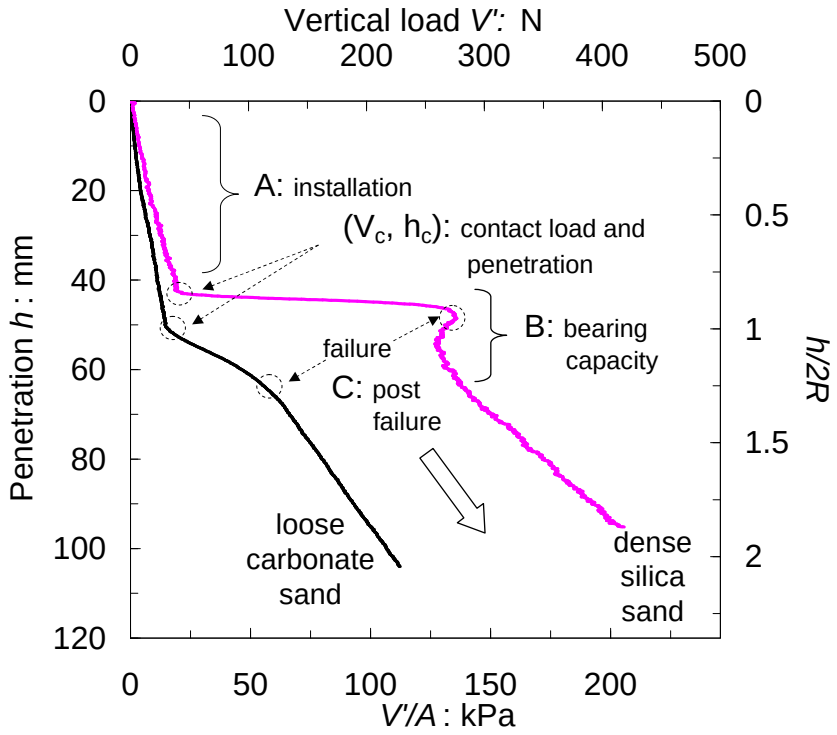

Figure 3.1: Measured vertical load-displacement curves of test FV55 in a $R_d = 88\%$ silica sand, and test FV65 in a $R_d = 26\%$ carbonate sand, using caisson model F_5, $2R = L = 51$ mm and $\frac{L}{2R} = 1$

linson, 1999; Das, 2003) there are still unresolved issues. Using the stress characteristic method the bearing capacity problem in triaxial or plane conditions can be solved without the superposition of cohesive, surcharge and weight components (Bolton and Lau, 1993; Cassidy and Houlsby, 2002). Research is still in course to solve bearing capacity problems without the superposition effect (Ukritchon *et al.*, 2003; Zhu *et al.*, 2003; Kumar, 2003; Hjiaj *et al.*, 2004, 2005; Kobayashi, 2005; Osman and Bolton, 2005; Tsukamoto, 2005; Smith, 2005; Przewlócki, 2005; Lee *et al.*, 2005). Exact bearing capacity calculations are claimed to be achieved by means of the stress characteristic method using remeshing in the computer program ABC developed by Martin (2005). In addition, the validity of proposed empirical factors to account for footing shape, embedment, footing and load inclination are still being studied (Salgado *et al.*, 2004; Lee and Salgado, 2005; Zhu and Michalowski, 2005; Edwards *et al.*, 2005; Honjo and Amatya, 2005; Gourvenec *et al.*, 2006; Cerato and Lutenegger, 2006). Furthermore, the classical bearing capacity theory does not include calculation of settlements.

From preliminary calculations caissons taken as a rigid flat footing of depth $D = L$, can significantly increase the bearing capacity compared with the case when the skirt is ignored $D = L = 0$. However, there is still doubt whether the softening effect of the soil plug may modify significantly the bearing capacity. Therefore, research is needed to know how to assess the bearing capacity of skirted footings.

Returning to the second objective of this investigation, to solve the combined loading problem within the framework of plasticity theory as described in the introductory chapter, it is necessary to define a hardening law. In the study of the combined loading response of shallow foundations Martin (1994), Gottardi *et al.* (1999) and Houlsby and Cassidy (2002), have found that the hardening law relationship is mainly given by the vertical load penetration response. However, predictions of footing response have been improved when hardening becomes a function not only of the plastic vertical displacement, but also of the plastic rotational and plastic horizontal displacements (Houlsby and Byrne, 2001; Cassidy *et al.*, 2002). Bienen *et al.* (2006) extended the hardening law formulation including the six components of plastic displacement. Furthermore, one of the conclusions of Nguyen-Sy (2006) is that the value of the parameter V_o (interpreted as bearing capacity within plasticity models) has significant repercussions on the prediction of monotonic and cyclic combined loading response of suction caissons using hyperplasticity theory.

The present chapter will present experimental results from bearing capacity tests. A brief review of the bearing capacity formulation is given with the intention of showing the expressions later used in the analysis. Study of the hardening law is presented at the end of the chapter.

3.2 BEARING CAPACITY OF SHALLOW FOUNDATIONS

Theoretical and experimental research has been carried out for more than eighty years to resolve rigorously the bearing capacity of shallow foundations on sand. There are available solutions for flat strip and flat circular footings as well as for conical footings, but not yet for skirted footings. Since a flat footing is a particular case of a skirted footing with no skirt, the study of flat footings is a natural starting point for the subsequent study of skirted footings.

By means of a combination of lower and upper bound theorems and empiricism Terzaghi (1943) developed a general bearing capacity formulation which has been widely used in engineering practice. For a strip footing of width B and length L ($A = BL$) on a soil with angle of friction ϕ', cohesion c, and surcharge σ'_v the bearing capacity V_o can be written as:

$$\frac{V_o}{A} = cN_c + \sigma'_v N_q + \frac{1}{2}\gamma' B N_\gamma \tag{3.1}$$

where N_c, N_q and N_γ are the bearing capacity factors. By analysing the punch of a strip metal tool on the surface of a metal mass (assumed cohesive but weightless), Prandtl (1920) determined the exact solution for N_c, which correspond to the first squared brackets in the following expression:

$$\frac{V_o}{A} = c\left[\cot\phi'\left\{\tan^2\left(\frac{\pi}{4}+\frac{\phi'}{2}\right)e^{\pi\tan\phi'}-1\right\}\right] + \sigma_v\left[\tan^2\left(\frac{\pi}{4}+\frac{\phi'}{2}\right)e^{\pi\tan\phi'}\right] \tag{3.2}$$

The second squared brackets in (3.2) correspond to N_q, which was determined by Reissner (1924) from the analysis of a strip metal embedded in a metal mass (assumed frictional but cohesionless and weightless). In geotechnical engineering expression (3.2) has been adopted to solve bearing capacity problems, where N_c and N_q are expressed as:

$$N_c = (N_q - 1)\cot\phi' \tag{3.3}$$

$$N_q = \tan^2\left(\frac{\pi}{4} + \frac{\phi'}{2}\right) e^{\pi \tan \phi'} \tag{3.4}$$

For a soil with weight there is not yet a unique formula for N_γ. Brinch Hansen (1970) among others, proposed the following formula for rough soil-footing contact:

$$N_\gamma = 1.5(N_q - 1)\tan \phi' \tag{3.5}$$

This simple semi-empirical expression is useful in the sense that it gives values which are close to the analytically calculated values by Bolton and Lau (1993), Cassidy and Houlsby (2002) and Martin (2005).

Terzaghi's formulation (3.1) has been subject to several adjustments, not just for the self-weight bearing capacity factor N_γ, but also for the inclusion of shape factors for footing geometries different from the strip case. Shape factors are no longer required for circular footings since values of N_q and N_γ are now available. Exact values of the axisymmetric N_q can be found in Bolton and Lau (1993).

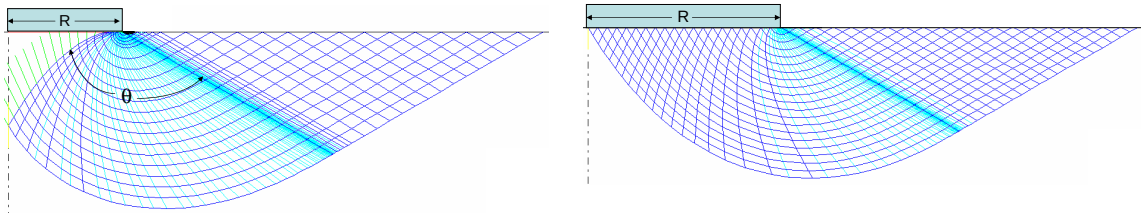

(a) Prandtl mechanism for rough footing (b) Hill mechanism for smooth footing

Figure 3.2: General shear failure mechanisms (Martin, 2005)

The development of a general shear failure mechanism is assumed as a condition *sine qua non* in bearing capacity analysis. In fact, Prandtl and Hill mechanisms of shear failure, shown in Figures 3.2(a) and 3.2(b), correspond to the case of general shear failure for rough and perfectly smooth footing-soil contact respectively. Alternatively, Vesić (1975) defined three possible symmetric failure mechanisms depending on the relative density R_d of the soil: general shear failure, local shear failure and punching failure. The bearing capacity analysis of skirted footings has the difficulty that the soil properties initially measured may change during installation since the rim of the skirt causes shearing of the soil

with a deep failure mechanism (Meyerhof, 1951). In addition, more significant changes are expected during phase B (Figure 3.1) where much higher loads develop. Consequently, the stress level increases considerably below the caisson lid leading to different consequences depending on the soil packing state. For a loose sand a contractile response induces an increase of the soil density and hence an increase of the angle of friction mobilised during failure. On the other hand, for a dense sand a dilative response during installation and before failure causes the angle of friction mobilised to reduce.

The bearing capacity of a caisson foundation can be calculated using bearing capacity theory as follows:

$$V_o = 2\pi R_o \int_0^h \tau_o dz + (\sigma'_v N_q + \gamma' R_o N_\gamma) A_o \tag{3.6}$$

where the subscript $_o$ identifies the radius, shear stress and area of the outside of the caisson as opposed to the inside, h is the caisson penetration, and N_q and N_γ are the bearing capacity factors for circular footings. The first term in (3.6) is the friction force which acts only on the outside skirt wall.

3.3 EXPERIMENTAL RESULTS

A total of 45 vertical loading tests using model scaled skirted footings were conducted. The skirted footings represent suction caisson foundations. The tests were performed using caissons F_{1-7} which were loaded with the VMH loading rig on sands of different mineralogies and densities (see Chapter 2 for description of the rig, model footings and soil samples used). The main series of tests, 36 in all, were carried out on a dry Leighton Buzzard sand at four different densities. A second set of tests, 9 in total, were carried out on a very loose dry Dogs Bay carbonate sand.

Displacement controlled tests were carried out under a constant velocity of penetration $\dot{h} = 0.05$ mm/s. In Table 3.1 each test is identified by two digits; the first indicates the sample number (or tank number) and the second the test number for that sample. The

tests are labelled from FV21 to FV59 for the Leighton Buzzard sand and from FV61 to FV69 for the Dogs Bay sand. The first tank series was a trial run. Each block in Table 3.1 corresponds to a caisson F with aspect ratio $\frac{L}{2R}$, tested in a soil with relative density R_d. V_c and h_c represent the soil-caisson lid *contact* load and penetration, as shown in Figure 3.1, where contact can also be understood as the end of installation. V_y and h_y represent the load and penetration at *yield*. The word yield is used in this particular loading condition to classify the foundation *failure* or collapse as indicated in Figure 3.1. Yield in a broader context is an irreversible phenomenon of deformation or displacement which can be present or not depending on the loading path applied.

Table 3.2 presents the values of the soil unit weight γ_d, specific volume υ, and peak friction angle ϕ'_{peak}. The only parameter directly measured was γ_d, thereby the specific volume was obtained as $\upsilon = \frac{G_s\gamma_w}{\gamma_d}$, where $\gamma_w = 9.8$ kN/m^3. The calculation method to determine ϕ'_{peak} was presented in section §2.2.4.

3.3.1 Loose sand samples

The series of tests on Dogs Bay sand and Leighton Buzzard sand are shown in Figures 3.3(a), 3.3(b) and 3.3(c). Similar load-displacement curves can be observed in the sense explained in Figure 3.1, *i.e.* phases A, B and C are present (except phase A for the flat footing). Yield loads V_y (circles) were determined as the intersection of two straight lines fitted to phase B and phase C respectively (determination of yield loads will be again touched on in Chapter 5). By superposing the theoretical bearing capacity curves obtained from a constant angle of friction ϕ' (equation (3.6)) on the experimental curves, the mobilised ϕ'_{mob} can be identified in Figures 3.3(a), 3.3(b) and 3.3(c). The friction outside the caisson was calculated by solving the integral for a linear distribution of stresses:

$$2\pi R_o \int_0^h \tau_o dz = \pi R_o \gamma_d (K\tan\delta)_o h^2 \tag{3.7}$$

For the range of ϕ'_{mob} values of the loose sands a lateral earth pressure coefficient $K \approx 2$ was adopted (see beginning of Chapter 4 for the expression of K used), and assuming a

Table 3.1: Summary of vertical loading tests

Caisson, $\frac{L}{2R}$	Test	R_d: %	V_c: N	h_c: mm	V_y: N	h_y: mm
	FV61	26			32	6.3
	FV27	40			18	3.0
F_1, 0	FV41	47	n.a.	n.a.	26	3.5
	FV31	83			118	4.0
	FV51	88			105	1.5
	FV62	26	7.3	13.1	64	28.0
	FV21	40	6.0	13.4	32	17.5
F_2, 0.26	FV49	47	5.2	12.0	44	16.4
	FV39	83	10.4	11.3	180	16.5
	FV52	88	14.8	10.7	153	13.0
	FV63	26	75	13.6	25.4	38.5
	FV22	40	52	30.5	10.5	23.4
F_3, 0.51	FV43	47	8.5	22.1	64	27.2
	FV33	83	19.2	20.6	236	30.0
	FV53	88	18.1	21.2	225	24.5
	FV64	26	21.3	39.1	96	54.5
	FV29	40	16.9	36.6	80	44
F_4, 0.76	FV44	47	16.4	33.7	82	41
	FV34	83	35.1	32.0	265	39
	FV59	88	32.8	31.1	275	35
	FV65	26	29.9	50.5	112	63.5
	FV24	40	27.1	48.6	90	57
F_5, 1	FV45	47	23.8	45.6	104	54.5
	FV58	88	50.0	42.8	335	50
	FV35	83	50.5	42.2	330	46
	FV66	26	40.0	76.2	154	95.5
	FV25	40	38.3	70.9	130	79.5
F_6, 1.51	FV46	47	42.1	69.8	155	78
	FV36	83	86.7	63.6	416	71
	FV56	88	69.9	64.2	415	69
	FV68	26	63.2	103.1	173	118
	FV26	40	67.0	97.8	170	107
F_7, 2.01	FV47	47	61.1	95.0	225	106.6
	FV37	83	136.1	86.0	450	98
	FV38	83	123.2	87.2	700	100
	FV57	88	129.4	87.0	560	92

skirt-soil interface angle of friction $\delta = 16°$ results $(K \tan\delta)_o \approx 0.6$. Nevertheless, values of the outside friction (3.7) are practically negligible compared with the other terms in expression (3.6). Values of the exact bearing capacity factors (N_q from Bolton and Lau, 1993, and N_γ from Martin, 2005) were adopted considering a smooth soil-caisson contact according to section §2.3. The installation sequence shown in Figure 2.14, in which the

Table 3.2: Values used in bearing capacity calculations

Sand	R_d: %	γ_d: kN/m^3	υ	ϕ'_{peak}
Dogs Bay	26	10.34	2.609	40.3
Leighton Buzzard	40	15.69	1.657	35.9
	47	15.89	1.636	36.9
	83	17.00	1.529	42.2
	88	17.16	1.515	43.5

soil inside the caisson rests at the same level of the soil outside the caisson, was practically true for the caissons installed into the very loose Dogs Bay sand. Conversely, in the loose Leighton Buzzard sand this was not the case due to soil plug heave (heave is further discussed in section §3.3.5).

Bearing capacity of caisson foundations is clearly overestimated if ϕ'_{peak} is used in the calculations. This overestimation increases with the aspect ratio $\frac{L}{2R}$. It is worth noting, however, that bearing capacity is reasonably well predicted for the flat footing using ϕ'_{peak}. Observing again Figure 3.3(a), yield occurs after a considerable settlement of the caisson. This considerable compression has been also reported for a calcareous sand from Western Australia by Byrne and Houlsby (2001) for tests with a flat footing of diameter 150 mm. After a settlement of almost half of the diameter they could not determine yield. It is possible that due to this high soil compressibility a critical state condition may not be reached. For instance, Nutt (1993) determined a value of $\phi' = 37.1°$ from direct shear tests on a very loose Dogs Bay sand under $\sigma'_v = 40$ kPa. Luzziani and Coop (2002) and Coop *et al.* (2004) also determined that the critical state is reached for shear strains higher than 20% as observed in Figure 3.4. Therefore, in very loose sands since the punching shear mechanism prevents from the spread of failure surfaces (Vesić, 1975), ϕ'_{mob} is likely to not reach the value in critical state ϕ'_{cs}. Indeed, values between 35° and 38° are mobilised at yield according to Figure 3.3(a).

On the other hand, for the tests in silica sand, a local shear mechanism forms truncated failure surfaces, which can extend only along the spiral fan shown in Figure 3.2(b). As a consequence, the assumption of a ϕ'_{peak} in the calculations also overestimates bearing

capacity although not as much as for the calcareous sand. In fact, a clear critical state condition occurred at yield as can be observed in Figure 3.3(b) since a value of ϕ'_{cs} is mobilised. After yield ϕ'_{mob} increases due to compaction caused by further settlement, but yet ϕ'_{peak} is not reached. Figure 3.3(c) shows that soil dilation, though little, is restricted to develop only in the spiral fan and ϕ'_{mob} does not reach ϕ'_{peak} either. Therefore, to calculate bearing capacity of a caisson foundation in loose sand the *mobilised* angle of friction ϕ'_{mob} is unlikely to reach ϕ'_{peak}. It is important to know that the use of a single ϕ'

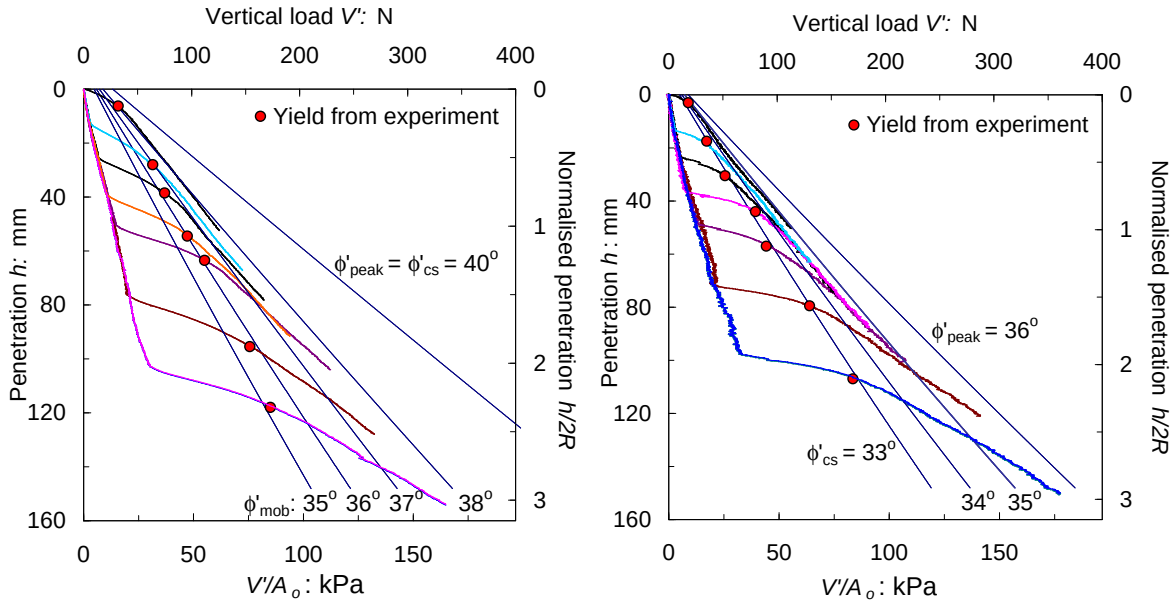

(a) Dogs Bay sand, $R_d = 26\%$ (b) Leighton Buzzard sand, $R_d = 40\%$

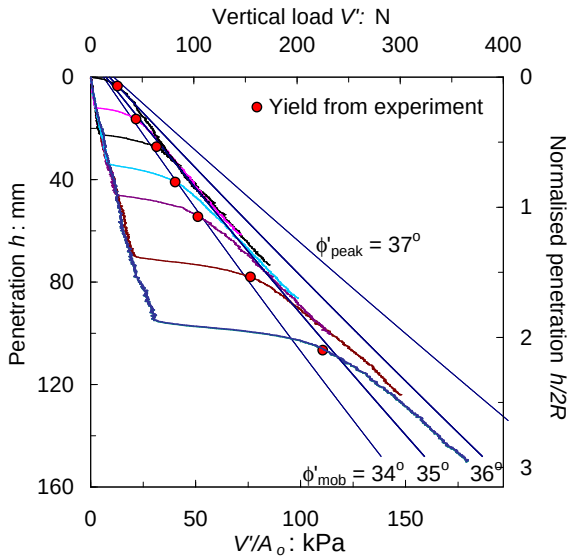

(c) Leighton Buzzard sand, $R_d = 47\%$

Figure 3.3: Measured vertical load-displacement curves and calculated bearing capacity for caissons with seven different $\frac{L}{2R}$

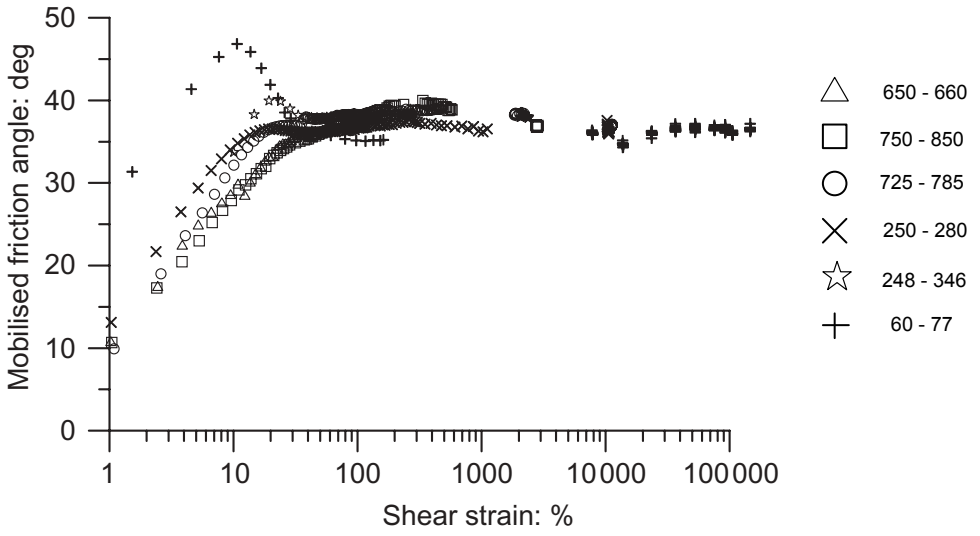

Figure 3.4: Mobilised angle of shear resistance with shear strain of Dogs Bay sand. Numbers next to symbols correspond to the net σ'_v during shearing (taken from Coop *et al.*, 2004)

should be treated as an attempt to represent an average value of the zones in failure.

3.3.2 Dense sand samples

The results of tests in dense sand are shown in Figures 3.5(a) and 3.5(b). In loose sample tests yield loads were found always at displacements $h_y > L$, whereas for dense samples $h_y \leq L$ (except in tests FV39 and FV33). It can be observed that a much higher increase of load with displacement leads to higher bearing capacity presented in the form of peaks. This peak load demonstrates that the soil dilated considerably as a consequence of shearing. Dilative behaviour was observed as heave of the soil surface around the caisson, which indicates the development of a general shear mechanism (see Figure 3.2(a) in Vesić, 1975). Because the tests were displacement controlled, it was possible to record beyond the peak a short load relaxation followed by a softening response that lasted until a settlement of around 20% of the diameter. The additional surcharge gained with subsequent settlement caused the final hardening response.

Since a general shear mechanism is expected to occur owing to the high values of R_d (Vesić, 1975), ϕ'_{peak} should be used. By superposing the theoretical curves on the experimental curves, it is observed that for flat footings bearing capacity calculation with

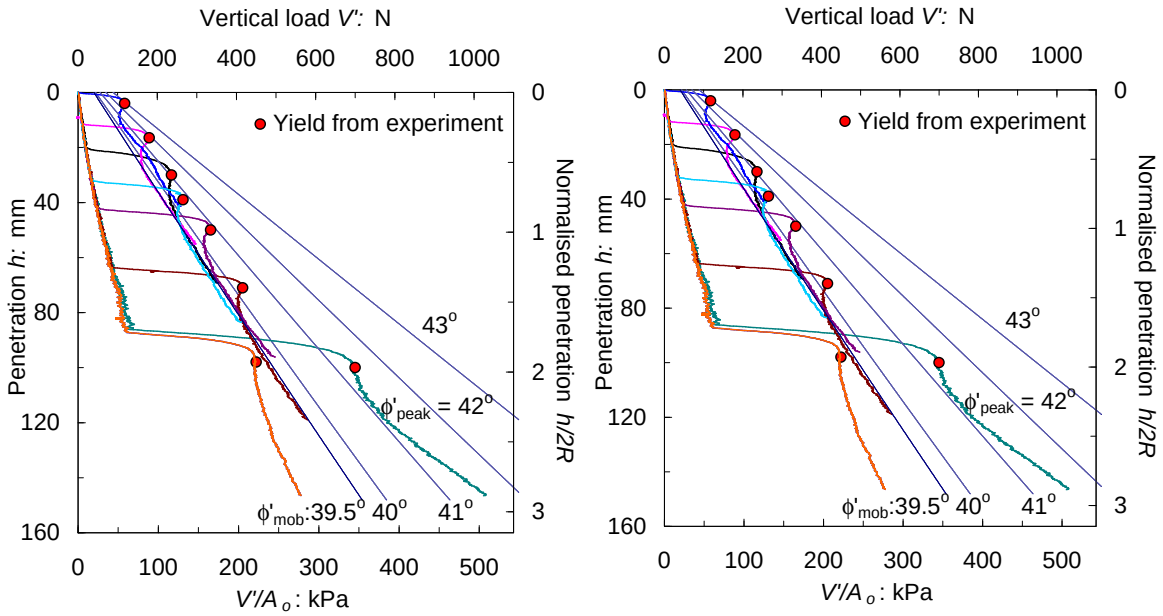

(a) Leighton Buzzard sand, $R_d = 83\%$ (b) Leighton Buzzard sand, $R_d = 88\%$

Figure 3.5: Measured vertical load-displacement curves and calculated bearing capacity for caissons with seven different $\frac{L}{2R}$

ϕ'_{peak} gives good predictions, nevertheless, for skirted footings the predictions are overestimated. The discrepancy may be seen as not so significant, however, since the values of ϕ'_{mob} are high, one or two degrees can represent a big difference in bearing capacity. The reduction from ϕ'_{peak} to ϕ'_{mob} may be due to higher stresses developed with depth (increase in surcharge), which were not possible to account for in the calculation of ϕ'_{peak}. As a consequence, soil dilation was then restricted from developing completely. Alternatively, installation effects may reduce the initial soil strength. Although the soil plug is compressed during bearing capacity (phase B), there is irrecoverable deformation due to softening of the soil during installation caused by previous soil dilation in the plug, at the tip and next to the skirt outside the caisson. Soil dilation was reduced even more after yield, reaching a stage of strength where bearing capacity increases mobilising a lower ϕ'_{mob} between 39° and 40°.

3.3.3 The axisymmetric bearing capacity coefficient N_q

From the $h - V$ plots presented in Figures 3.3(a) to 3.5(b) it is clear that bearing capacity increases with settlement. Experimental data shown in Figure 3.6 confirms that N_q increases with $\frac{L}{2R}$ and R_d. The calculation of N_q was done along phase C, where

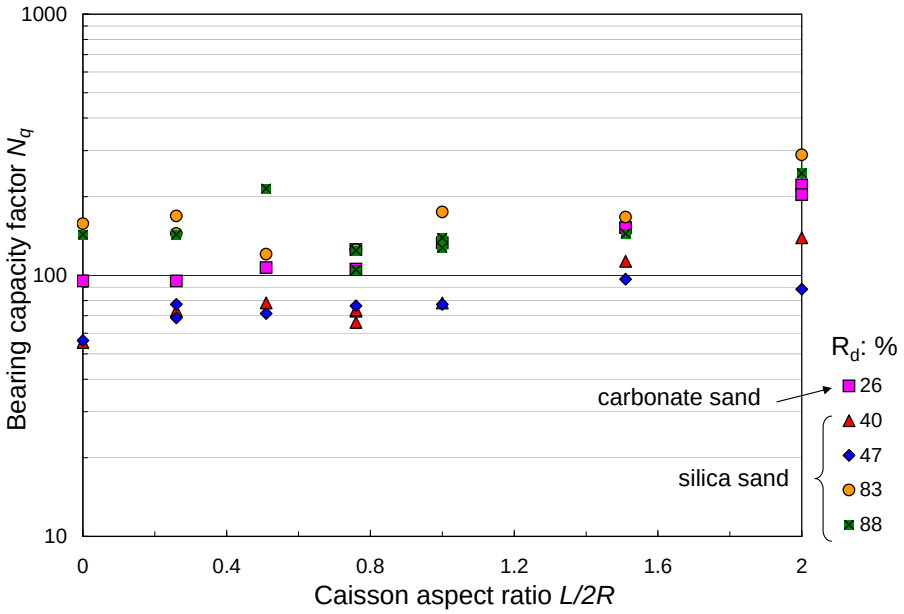

Figure 3.6: Experimental values of axisymmetric N_q

the component of surcharge is more predominant than self-weight. This occurs for large displacements when the footing has settled more than 20% of its diameter (plus h_c). The points plotted in Figure 3.6 were calculated from expression (3.1) using the following equation:

$$\frac{V'}{\pi R^2} = \gamma' w N_q + \frac{1}{2}\gamma'(2R)N_\gamma \tag{3.8}$$

where V' is the mobilised bearing capacity. For sufficiently large settlements the surcharge component predominates over the weight component, thus N_q can be expressed as:

$$N_q = \frac{1}{\gamma'\pi R^2}\frac{\Delta V'}{\Delta w} \qquad \text{for} \quad w > h_c + 0.4R \tag{3.9}$$

Despite the scatter it can be observed in Figure 3.6 that for aspect ratios less than one N_q is practically constant for a certain level of relative density, and for aspect ratios 1 $< \frac{L}{2R} < 2$, N_q slightly increases.

Friction around the skirt wall was not considered in equation (3.9). To evaluate friction effects it will be assumed that the friction force per unit of penetration can be obtained by means of:

$$\Delta F = \gamma'(K \tan\delta)\pi 2R_o h \Delta h \tag{3.10}$$

where F is the friction force, $(K\tan\delta)$ is the coefficient of lateral earth pressure K multiplied by a friction coefficient $\tan\delta$, R_o is the exterior radius, and h is the penetration, *i.e.* $h = h_c + w$, where h_c is the contact penetration between the soil plug and the caisson lid. Expression (3.10) can also be derived as the increase in lateral earth pressure due to the extra settlement Δw as follows:

$$F + \Delta F = \gamma'(K\tan\delta)\pi 2R_o\left[\frac{1}{2}(h_c+\Delta w)^2 - \frac{\Delta w^2}{2}\right] = \gamma'(K\tan\delta)\pi 2R_o\left[\frac{1}{2}h_c^2 + h_c\Delta w\right] \tag{3.11}$$

Thus N_q is given by:

$$N_q = \frac{\Delta V'}{\Delta h}\frac{1}{\gamma'\pi R^2} - 2(K\tan\delta)\frac{h}{R} \approx \frac{\Delta V'}{\Delta h}\frac{1}{\gamma'\pi R^2} - \frac{h}{R} \tag{3.12}$$

The evaluation of the second term in (3.12) gives the reduction in the N_q value caused by the friction on the external skirt wall, which can be approximated to the penetration radius ratio $\frac{h}{R}$. Because of the small magnitude of $\frac{h}{R}$ the effect of friction can be neglected.

3.3.4 The axisymmetric bearing capacity coefficient N_γ

The values of N_γ were determined directly from the V_y loads in the $h-V$ curves, and the friction force F developed during installation was subtracted from V_y in the following

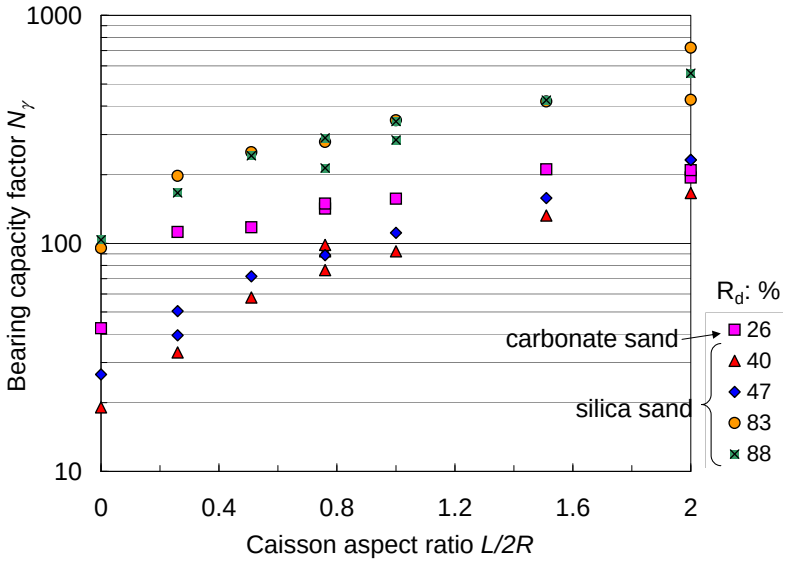

Figure 3.7: Experimental values of axisymmetric N_γ

form:

$$N_\gamma = \frac{V_y - F}{\gamma' \pi R^3} \tag{3.13}$$

A considerable increase of N_γ appears with relative density and with caisson aspect ratio. Since surcharge has not been accounted for in the N_γ analysis, it is clear that the N_γ increase is strongly related to the depth increase for a given relative density.

3.3.5 Soil plug heave

Heave of the soil-plug caused during installation is a concern because caisson design must be modified. It is necessary to evaluate the proportion of heave in order to include it in subsequent calculations.

Heave was determined as the subtraction of the penetration h_c to the skirt length L. Values of h_c are listed in Table 3.1 and heave is plotted in Figure 3.8(a) as a ratio of the diameter ($\frac{L-h_c}{2R}$) and in Figure 3.8(b) as ratio of the skirt length ($1 - \frac{h_c}{L}$). It is clearly observed that the onset of contact between the soil and caisson lid occurs always before full penetration L is completed ($h_c < L$), with the exception of tests in very loose carbonate sand. Caissons in dense silica sand generated a steady increase of heave with the aspect ratio, as shown in Figure 3.8(a). However, for loose samples there was a limit between $\frac{L}{2R}$ = 1.5 and $\frac{L}{2R}$ = 2. Figure 3.8(b) shows that heave had a maximum at $\frac{L}{2R}$ = 0.5 reducing for other aspect ratios.

Heave can be calculated assuming that the soil displaced is equivalent to the volume of skirt wall penetrated.

$$h_{heave} = L - h_c = \left[\left(\frac{R}{R - 2t} \right)^2 - 1 \right] h_c \tag{3.14}$$

This simple equation offers a reasonable solution for the loosest silica sand as shown in Figure 3.8(a). For dense soils, it could be argued that the vertical stresses of the soil inside the caisson are higher than outside the caisson due to arching (Chapter 4). Consequently

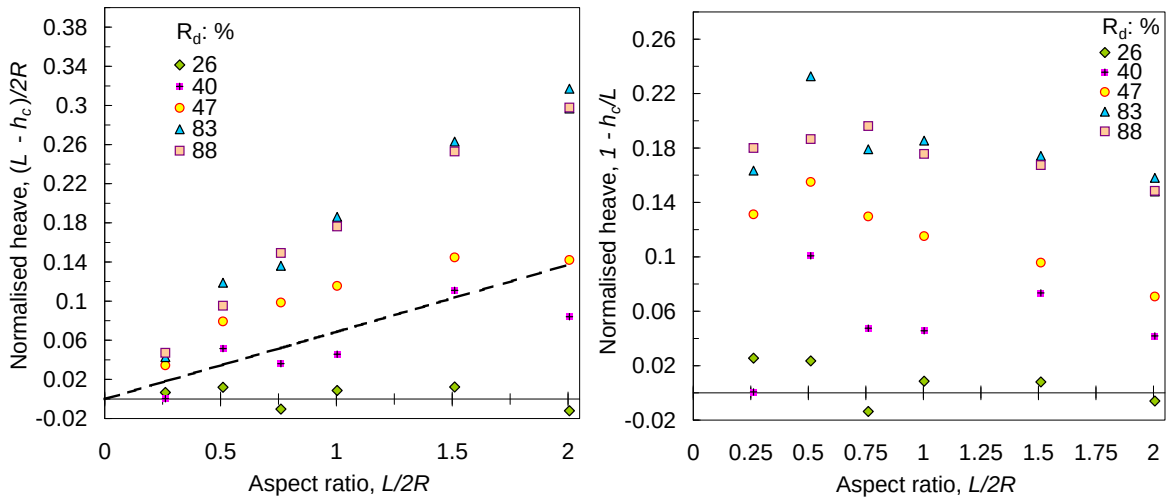

Figure 3.8: Heave found at the end of the installation for skirted footings pushed into the ground as a ratio of the (a) diameter, and the (b) length

the soil is removed completely outwards and the heave would be caused only by dilation of the sand. More importantly, dilation of dense sands can cause heave as high as 2.5 times that given by expression (3.14).

3.4 HARDENING LAW

As pointed out in the introduction, the determination of a hardening law is vital for the development of a hyperplasticity model to study the combined loading problem of caisson foundations. Construction of the hardening law requires modelling of the relationship between the vertical load and the vertical displacement. Looking at Figure 3.1, the part of the hardening law corresponding to phase B and C will be developed in the following. Phase A (installation) will be considered in Chapter 4.

Nova and Montrasio (1991) performed purely vertical load-controlled tests on loose sand. They removed the soil whilst the footing penetrated the ground to keep the surface at the same level as the footing base. Although an unrealistic procedure, it is useful in determining a clear maximum vertical load, which make modelling easier. An expression

suggested by Butterfield (1980) can be used to reproduce that response,

$$\frac{V'}{V_y} = 1 - e^{-\frac{aw}{V_y}} \tag{3.15}$$

where V_y is the asymptote of the curve (failure load) and a the initial slope of the load-settlement curve. Because the surcharge exists, especially for caissons, it is necessary to find an expression that is not forced to have a horizontal asymptote, but an inclined asymptote. de Santa Maria (1988) proposed a three-parameter hyperbola which is able to achieve an inclined asymptote.

$$V' = \frac{w}{\frac{1}{a} + \frac{w}{b+cw}} \tag{3.16}$$

Firstly, the parameter a is the initial slope of the curve which for a rigid circular foundation can be modelled as a static spring with a constant stiffness, K_V given by (Boussinesq, 1878):

$$a = K_V = \frac{4GR}{1-\nu} \tag{3.17}$$

where G and ν are the soil elastic shear modulus and the soil Poisson's ratio respectively.

Secondly, the parameter c can be deduced from the curve slope after failure (hardening in phase C), which is given by $\gamma' N_q \pi R^2$ for a geostatic vertical stress σ'_v distribution with depth (see equation (3.9)). Then c can be obtained from the curve slope during hardening and the elastic stiffness coefficient as follows:

$$c = \frac{\gamma' N_q \pi R^2 K_V}{K_V - \gamma' N_q \pi R^2} \tag{3.18}$$

Finally, the last parameter to predict the $w - V'$ response is b, which is related to the bearing capacity of a footing without surcharge, *i.e.* $\frac{1}{2}\gamma' N_\gamma (2R) \pi R^2$. Then the expression for b results in:

$$b = \frac{\gamma' N_\gamma \pi R^3 K_V}{K_V - \gamma' N_q \pi R^2} \tag{3.19}$$

Equation (3.19) has the same denominator as (3.18), and the numerator differs only in the exponent of R and the change of N_q by N_γ. Figure 3.9 depicts the measured and calculated $w - V'$ curves using (3.16) for a flat footing tested on loose sand. The calculated curves were fitted using the 'Solver' procedure within MS Excel to obtain the parameters a, b and c. The properties of the soil can be obtained using equations (3.17), (3.18) and (3.19), knowing *a priori* a, b and c from the tests.

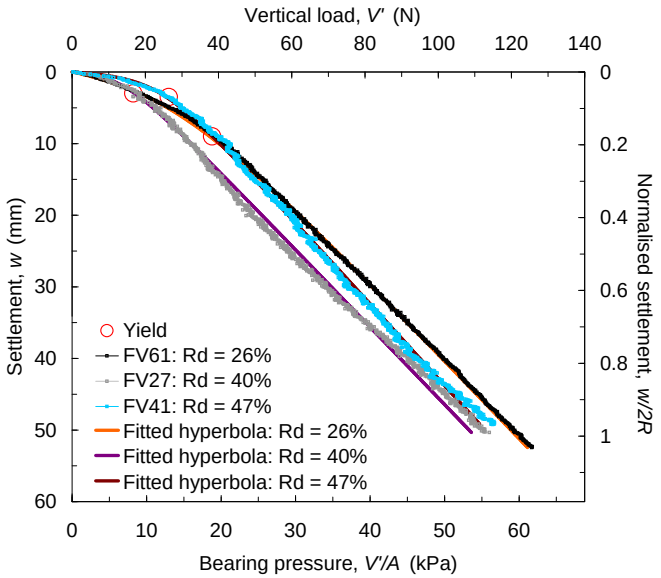

Figure 3.9: Experimental and calculated vertical load-displacement curves

$$G = a\frac{1-\nu}{4R} \tag{3.20}$$

$$N_q = \frac{1}{\gamma'\pi R^2}\frac{ac}{a+c} \tag{3.21}$$

$$N_\gamma = \frac{1}{\gamma'\pi R^3}\frac{ab}{a+c} \tag{3.22}$$

$$w_y = \frac{b}{a+c} \tag{3.23}$$

Table 3.3 shows values of vertical stiffness K_V, shear moduli G, N_q, N_γ and settlement during yield w_y obtained using equations (3.20), (3.21) and (3.22). ν has been assumed to be equal to 0.2.

Equation (3.15) can be used as a first approximation of the $w - V'$ response in the

Table 3.3: Parameters fitted with a hyperbola for the loose sand test results

Test	K_V N/mm	G kPa	N_q	N_γ	$w_y/2R$ %
FV61	9.3	73	87	71	8.05
FV27	18.4	144	59	21	1.79
FV41	28.3	222	55	32	1.84

case of dense sand, but it is not able to predict beyond yield (V_y, w_y). Gottardi *et al.* (1999) introduced an empirical expression - used to fit the data of vertical loading tests performed on dense silica sand (yellow Leighton Buzzard sand), which can provide a fit after a peak yield. This expression is:

$$V' = \frac{K_V w^p}{1 + \left[\frac{K_V w_y}{V_y} - 2\right] \frac{w^p}{w_y} + \left[\frac{w^p}{w_y}\right]^2} \tag{3.24}$$

where this time K_V is an initial plastic stiffness , w^p is the plastic component of the vertical displacement w, V_y and w_y are the peak value of the vertical load and vertical displacement. The use of plastic displacement refers to the fact that the elastic component must be subtracted from the total displacement. In practice the elastic component is very small compared with the plastic displacement, therefore, it can be neglected. Subsequently, Cassidy (1999) and Houlsby and Cassidy (2002) added the possibility of modifying the post-peak softening behaviour introducing a dimensionless constant f_p to 'lift' the curve avoiding V' becoming zero when w^p increases to large values. The expression is:

$$V' = \frac{K_V w^p + \frac{f_p}{1-f_p}\left[\frac{w^p}{w_y}\right]^2 V_y}{1 + \left[\frac{K_V w_y}{V_y} - 2\right] \frac{w^p}{w_y} + \frac{1}{1-f_p}\left[\frac{w^p}{w_y}\right]^2} \quad w < 0.4R \tag{3.25}$$

Equation (3.25) equals (3.24) for $f_p = 0$. The experimental results presented here agree well with equations (3.24) or (3.25) until softening occurs. The hardening behaviour that appears after softening can not be well simulated. To include a peak response, softening and final hardening the following expression is proposed:

$$V' = \frac{aw + cw^3}{b^2 + w^2} \tag{3.26}$$

where a and c retain the same meaning as initial and final stiffness, but b is now related not only to the peak bearing capacity, but also to the minimum bearing capacity that occurs after the peak. The vertical displacement at peak is given by:

$$w_y = \sqrt{\frac{1}{2}\left(\frac{a}{c} - 3b^2\right) - \frac{1}{2}\sqrt{\left(\frac{a}{c} - 3b^2\right)^2 - \frac{4ab^2}{c}}} \tag{3.27}$$

and the vertical displacement at the end of softening and beginning of hardening is giving by:

$$w_s = \sqrt{\frac{1}{2}\left(\frac{a}{c} - 3b^2\right) + \frac{1}{2}\sqrt{\left(\frac{a}{c} - 3b^2\right)^2 - \frac{4ab^2}{c}}} \tag{3.28}$$

An iterative procedure is required to find b using equations (3.26) and (3.27) for $V' = V_y = \frac{1}{2}\gamma' N_\gamma (2R)\pi R^2$. Figure 3.10 shows an example of the improvement of the estimation of the $w - V'$ curve after peak and especially after the relaxation and softening. The further hardening is possible to reproduce using equation (3.26) in contrast with the expressions (3.24) by Gottardi *et al.* (1999) or (3.25) by Houlsby and Cassidy (2002) where the softening occurs *ad infinitum*.

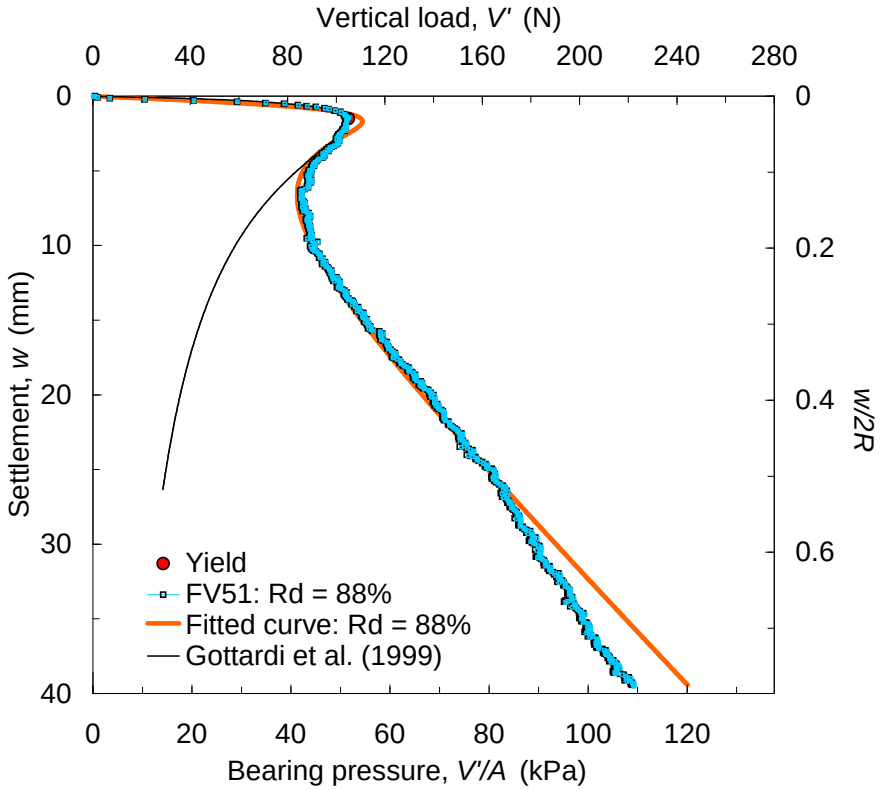

Figure 3.10: Experimental and theoretical vertical load-displacement curve for dense sand

3.5 CONCLUSIONS

Bearing capacity increases with the length of the caisson skirt. It was found that bearing capacity calculations of skirted footings require the choice of a mobilised angle of friction ϕ'_{mob}, because the use of a peak angle of friction ϕ'_{peak} leads to overestimations. In a very loose carbonate Dogs Bay sand critical state was not reached leading to values of ϕ'_{mob} less than ϕ'_{cs}, giving evidence of a punching failure mechanism. In the case of loose silica Leighton Buzzard sand, critical state was reached, hence $\phi'_{mob} = \phi'_{cs}$, which suggests the development of a local shear failure mechanism. In dense silica sand, dilation controlled the foundation response. The caisson installation (skirt penetration) formed a soil plug that rose inside the caisson above the mudline. This phenomenon is believed to reduce the ϕ'_{mob} below ϕ'_{peak} owing to progressive failure, since a general shear failure mechanism occurred.

Experimental values of N_q were obtained during the hardening response after failure. Increase of N_q with skirt length demonstrated the effect of surcharge. Experimental values of N_γ increased for $\frac{L}{2R} > 0$ reflecting the superposition effect of the surcharge.

A three term hyperbola proved to be a good hardening law expression for non-dilative sands. It was possible to interpret the physical meaning of the hyperbola parameters which allows for the determination of soil properties. For dilative sands expressions proposed by Gottardi *et al.* (1999) and by Cassidy and Houlsby (2002) were able to predict unlimited softening response. An expression capable to reproduce hardening observed after peak and softening is proposed.

Chapter 4

INSTALLATION OF SUCTION CAISSONS IN SAND

Abstract

This chapter is devoted to the study of the installation of caissons in sand by pushing and by suction. Experiments were planned and performed to asses the variables involved in the process of caisson installation. The experimental results are analysed based on the theory proposed by Houlsby and Byrne (2005b). Comparisons between measured and calculated results are extensively pursued. The use of suction reduces drastically the net vertical load required to install a caisson in dense sand due to the hydraulic gradients created by the suction. It was found that calculations of the required suction for installation of caissons were highly dependent on the permeability ratio used.

4.1 INTRODUCTION

Experiments using model caissons installed by pushing into dry sands were performed as part of testing programmes to study vertical loading response (Chapter 3) and moment loading response (Chapter 5). The analysis for estimating the penetration resistance of pushed caissons is based mostly on methods derived for driven open end piles. Although in suction caisson aspect ratios are significantly shorter than in piles, the analysis consid-

ers the same approach assessing friction on the skirt and bearing capacity at the tip.

The installation of a caisson by suction is possible due to the application of a differential pressure between the interior chamber of the caisson and the exterior at the same datum. In practice this differential pressure is obtained by pumping water out of the caisson, which may or may not be submerged. For a submerged caisson the external pressure is hydrostatic, *i.e.* it varies linearly with the fluid height above the caisson. This differential pressure creates a negative pressure relative to hydrostatic or *suction* that forces the caisson skirt to penetrate into the ground. There are several factors that need to be considered to make this method of installation successful, *e.g.* sealing between the soil and the caisson skirt wall, availability, magnitude and limits of the suction, weight of the structure, geometry of the caisson and verticality of the caisson.

Houlsby and Byrne (2005b) include the 'arching effect' or 'silo effect' in the analysis of suction caisson installation. Soil arching has been recognised in several geotechnical problems such as buried pipes, underground cavities (Terzaghi, 1943), retaining walls (Handy, 1985) and plugging in open ended piles (Randolph *et al.*, 1991; de Nicola and Randolph, 1997; Jardine *et al.*, 2005). From these studies it is well known that the distribution of stresses with depth may not be linear and may be much higher than the geostatic. It is important to verify and calibrate this feature in the theory. The importance of modelling accurately the load-penetration response of a suction caisson is not only fundamental to estimate the installation response, but also for further modelling of the combined loading response. Additionally, results from pushed installation tests need to be compared with results from suction installation tests, in terms of the net load required to install similar caissons into similar soils. Moreover, as it will be subsequently evident calculation of the suction relies undoubtedly on the predicted pushing penetration resistance.

A unique feature of this type of foundation is the installation process aided by suction. In consequence, analysis of the feasibility of suction application is important as well as the limits of the suction. These issues are covered by the theory (Houlsby and Byrne

(2005b) calculation procedure is referred throughout this chapter as 'the theory' unless the contrary is mentioned), but they need to be verified and calibrated against physical evidence. Normally not all the caisson skirt penetrates into the ground under the structure's own weight. In light structures such as wind turbines, small penetration of the skirt into the ground will occur by own weight, approximately 10% or 20% of the skirt length L. However, this initial penetration is fundamental to create a seal capable of preventing the occurrence of an unconfined flow failure, *i.e.* piping failure. Once piping is developed erosion of the soil occurs, stopping the caisson penetration because of the drastic drop of the suction.

Houlsby and Byrne (2005b) found that predictions of the vertical load and the suction depend significantly on the value of the combined effect of lateral earth pressure K and friction coefficient $\tan\delta$, expressed as $K\tan\delta$. Although a range of values obtained from back calculated examples is given by Houlsby and Byrne (2005b), it is not yet clear how to chose a certain value from this range or more importantly how to calculate K for different conditions than the examples presented. Moreover, although the formulation to obtain expressions for non-linear stress distribution is presented, explicit expressions to obtain the vertical load and the suction are not shown by the above authors. This chapter progresses from the simple case of pushing installation in dry and loose sand, to pushing installation in saturated and dense sand to finally study the suction installation in dense sands.

4.2 THEORETICAL ANALYSIS

4.2.1 Pushing penetration

A general formulation to calculate the penetration load of caissons can be obtained considering skin friction and base resistance as for driven open ended piles. This formulation involves a shear stress distribution along the caisson skirt $\tau(z)$ and a normal stress distribution around the caisson tip σ'_{end}. Thus, the submerged load V' required to

penetrate a depth h the skirt of a circular caisson is given by:

$$V' = \underbrace{2\pi R_o \int_0^h \tau_o dz}_{F_o} + \underbrace{2\pi R_i \int_0^h \tau_i dz}_{F_i} + \underbrace{\int_{A_{rim}} \sigma'_{end} dA}_{B_c+B_q+B_\gamma} \tag{4.1}$$

where the subscripts o and i refer to *outside* and *inside* the caisson skirt wall respectively. Therefore, R_i and R_o are the inside and outside caisson radii; F_o and F_i represent the friction forces *inside* and *outside* the caisson skirt wall. The mobilised shear stress τ in the soil-skirt interface, called skin or shaft friction in pile analysis (Poulos and Davis, 1981; Fleming *et. al.*, 1994; Tomlinson, 1999; Randolph, 2003; Jardine *et al.*, 2005), is given by the Coulomb failure criterion, which can be expressed as:

$$\tau = \sigma'_r \tan\delta = K\sigma'_v \tan\delta \tag{4.2}$$

where σ'_r is the radial (horizontal σ'_h or normal σ'_n stress), K is the coefficient of lateral earth pressure, which depends on the soil stress history next to the skirt wall, and $\tan\delta$ is the coefficient of friction of the soil-skirt interface with δ being the interface friction angle. Figure 4.1(a) shows that owing to friction on the skirt wall soil arching occurs and since by definition principal stresses act only on planes of zero shear stresses σ'_1 and σ'_3 rotate, hence $\theta \neq 90°$. Taking force equilibrium on a triangular element and deducing $\sigma'_h - \sigma'_3 = \sigma'_1 - \sigma'_v$ from the Mohr circle shown in Figure 4.1(b), gives (Zeevaert, 1983; Handy, 1985; 2004):

$$K = K_A = \frac{\sigma'_h}{\sigma'_v} = \frac{\cos^2\theta + k_a \sin^2\theta}{\sin^2\theta + k_a \cos^2\theta} = \frac{1 - \sin^2\phi}{1 + \sin^2\phi} = \frac{\cos^2\phi}{2 - \cos^2\phi} \tag{4.3}$$

For a smooth wall $\theta = 90°$, and (4.3) reduces to the Rankine active coefficient $k_a = \frac{1-\sin\phi}{1+sin\phi}$. The Krynine active pressure coefficient K_A appears for fully mobilised friction at the wall replacing θ by $45° - \frac{\phi}{2}$. For instance, K_A finds application in the case of caisson pullout, when the skirt wall is extracted from the ground. So, drained tension capacity can be

calculated as:

$$V_t' = \gamma' h^2 (K_A \tan\delta)_o \pi R_o + \gamma' h^2 (K_A \tan\delta)_i \pi R_i \approx \gamma' h^2 2\pi R K_A \tan\delta \tag{4.4}$$

It has been found in studies of wall friction in buried pipes that when K_A is high, tanδ is low, keeping the product $K_A \tan\delta$ nearly constant with a theoretical maximum value of 0.193 (Handy, 2004). In the interest of analysing wall penetration into the ground the passive coefficient can be similarly deduced:

$$K = K_P = \frac{\sigma_h'}{\sigma_v'} = \frac{\cos^2\theta + k_p \sin^2\theta}{\sin^2\theta + k_p \cos^2\theta} = \frac{1+\sin^2\phi}{1-\sin^2\phi} = \frac{2-\cos^2\phi}{\cos^2\phi} \tag{4.5}$$

Perfectly smooth walls ($\theta = 90°$) reduce (4.5) to the Rankine passive coefficient $k_p = \frac{1+\sin\phi}{1-sin\phi}$. The Krynine passive pressure coefficient K_P is deduced for walls with fully mobilised friction replacing θ by $45° + \frac{\phi}{2}$.

The end bearing pressure σ_{end}' around the caisson rim will be calculated using the bearing capacity formulation in plane strains presented in Chapter 3, where B_c, B_q and B_γ correspond to the bearing capacity force components of cohesion, overburden and self weight respectively.

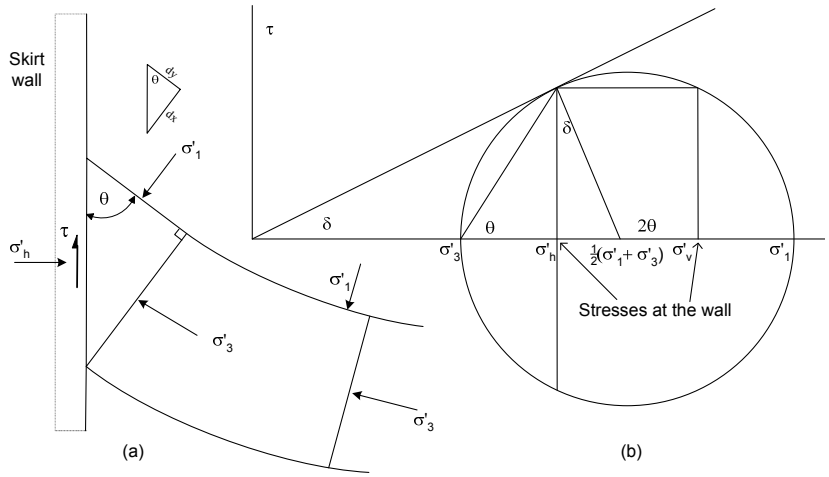

Figure 4.1: (a) Triangular soil element under force equilibrium showing arching trajectory defined by the minor principal stresses, and (b) Mohr circle showing stresses acting at the wall

4.2.2 Non-linear stress distribution

The vertical load V' required to penetrate a depth h the caisson skirt assuming a linear stress distribution $\sigma'_v = \gamma' z$, and assuming soil arching over the constant radii R_i and R_m (which results in an exponential stress distribution with depth) are covered in Houlsby and Byrne (2005b). An extension of this case considers the enhancement of stresses in a radius linearly varying with depth.

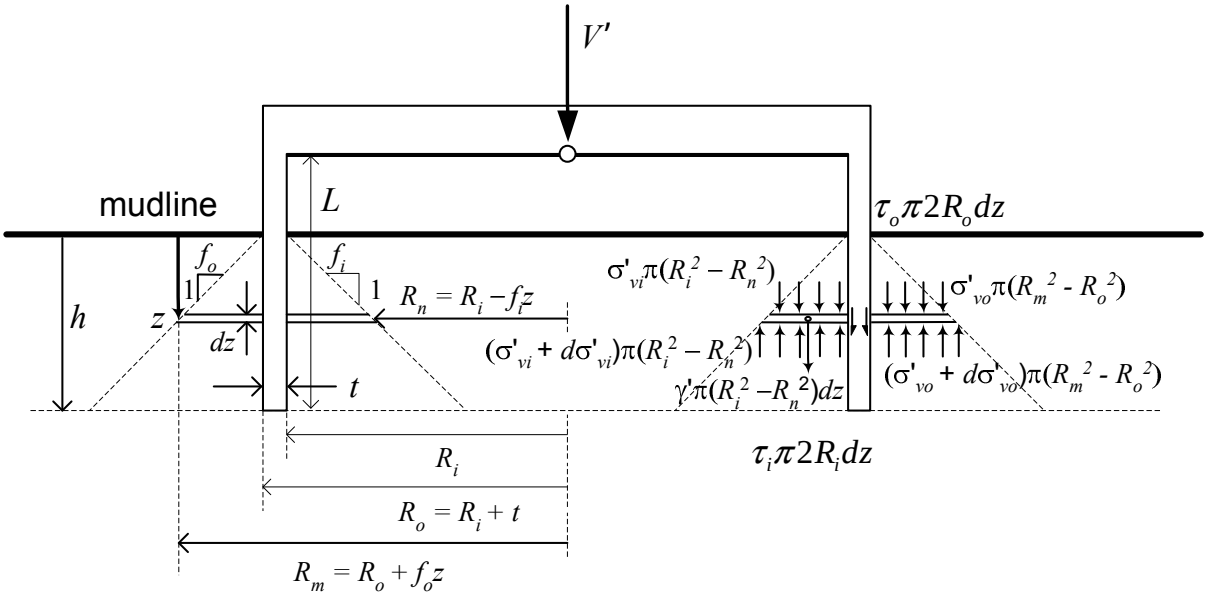

Figure 4.2: Outline of a suction caisson showing equilibrium of soil element dz

Figure 4.2 shows soil arching 'varying' linearly with depth inside the caisson as $R_i - R_n = f_i z$ and outside the caisson as $R_m - R_o = f_o z$, being f_i and f_o the respective constant rates of variation. Note the inverse contribution of arching, whilst inside the caisson R_n decreases with depth, outside the caisson R_m increases with depth. Equilibrium of the vertical forces acting on soil elements of thickness dz leads to the following ordinary differential equations ODE:

$$\frac{d\sigma'_{vi}}{dz} = f_i(z, \sigma'_{vi}) = \gamma' + \frac{\sigma'_{vi}}{Z_i(z)} \qquad \frac{d\sigma'_{vo}}{dz} = f_o(z, \sigma'_{vo}) = \gamma' + \frac{\sigma'_{vo}}{Z_o(z)} \tag{4.6}$$

where Z_i and Z_o can be written as:

$$Z_i = \frac{R_i \left[1 - \left(1 - \frac{f_i z}{R_i}\right)^2\right]}{2(K \tan\delta)_i} \qquad Z_o = \frac{R_o \left[\left(1 + \frac{f_o z}{R_o}\right)^2 - 1\right]}{2(K \tan\delta)_o} \tag{4.7}$$

Unfortunately there is not an analytical solution for (4.6). Nevertheless, these first order ODEs can be solved numerically using Euler or Runge-Kutta methods, in which each approximation for the unknown function is based on the previous value. A fourth order Runge-Kutta method was employed to solve (4.6) since it is more accurate and numerically stable than the Euler method. The iterative formula is given by:

$$\begin{aligned}
&\text{initial value of } \sigma'_v = 0 \text{ at } h = 0 \\
&\text{For } j = 0,\ 1,...,\ n\ \text{-}\ 1 \\
&k_1 = \Delta h f(h_j, \sigma_j) \\
&k_2 = \Delta h f(h_j + \frac{1}{2}\Delta h, \sigma_j + \frac{1}{2}k_1) \\
&k_3 = \Delta h f(h_j + \frac{1}{2}\Delta h, \sigma_j + \frac{1}{2}k_2) \\
&k_4 = \Delta h f(h_j + \Delta h, \sigma_j + k_3) \\
&\sigma_{j+1} = \sigma_j + \frac{1}{6}(k_1 + 2k_2 + 2k_3 + k_4)
\end{aligned} \tag{4.8}$$

where h is incremented by Δh, σ_j ($\equiv \sigma'_{v\,i_j} \equiv \sigma'_{v\,o_j}$) is incremented by a multiple of the parameters k_1, k_2, k_3 and k_4 preceding it, and $f(h, \sigma'_v)$ is the function on the right hand side of the ODE (4.6). The integration of (4.1) can be solved simultaneously changing the integrals for summations. The vertical load V' corresponding to a penetration depth h_j is obtained after each value of σ_{j+1} is solved, replaced in (4.2), sums are conducted to finally add the force terms as follows:

$$\begin{aligned}
V' = &\underbrace{2\pi R_o (K \tan\delta)_o \sum_{j=1}^{n} \sigma'_{v\,o_j} \Delta h}_{F_o} + \underbrace{2\pi R_i (K \tan\delta)_i \sum_{j=1}^{n} \sigma'_{v\,i_j} \Delta h}_{F_i} + \underbrace{\sigma'_{v\,i_n} 2N_q 2\pi R t}_{B_q} \\
&+ \underbrace{\gamma' t N_\gamma 2\pi R t}_{B_\gamma} \qquad \forall n \in \{1, ...N\} \quad \text{where} \quad n = \frac{h}{\Delta h} \quad \text{and} \quad N = \frac{L}{\Delta h}
\end{aligned} \tag{4.9}$$

4.2.3 Suction assisted penetration

A schematic flow net is depicted in Figure 4.3, representing a suction caisson of $\frac{L}{2R}$ = 0.5 and penetrating by suction half of its depth. The flow net has been constructed following procedures for plane strain conditions. For axial symmetric flow nets numerical

calculations are necessary (Aldwinkle, 1994). The suction or extraction of fluid from the caisson compartment creates a hydraulic gradient that makes interstitial fluid and fluid above the mudline to flow in the direction shown by the arrows in the figure. This flow occurs because of the presence of negative pressure differentials or negative relative heads between the fluid inside the caisson and the fluid in the soil voids. The flow direction is downwards outside the caisson and upwards inside the caisson. Horizontal flow occurs briefly as a transition from downwards to upwards flow. The flow channel next to the caisson's skirt wall drastically changes the flow direction, whereas for the other flow channels a smoother change occurs.

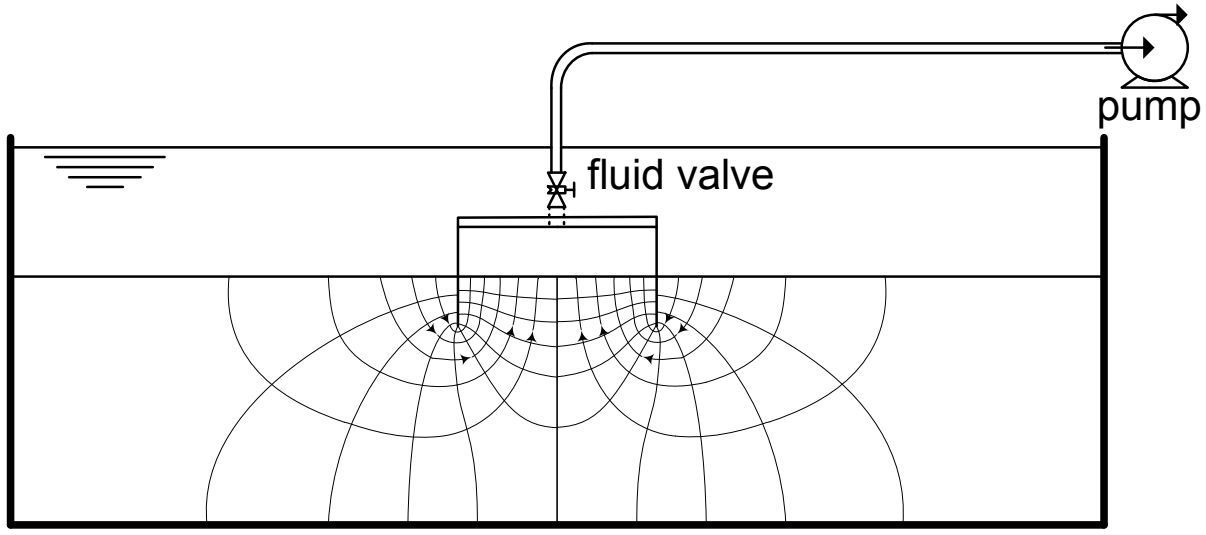

Figure 4.3: Seepage around a suction caisson during installation showing schematic flow net constructed using plane strain procedures

The flow direction caused by the suction influences the stresses and hence the soil strength and density. As a consequence, soil index and strength properties that are practically constant during a self-weight penetration can vary due to seepage created by the suction. The flow net sketched in Figure 4.3 considers a uniform permeability (vertical and radial). Alternatively, if seepage modifies the effective stresses then variation of the specific volume will occur; the coefficient of permeability (referred to as permeability onwards) can be substantially affected by the intensity of seepage because permeability is a function of the specific volume and hence of the soil unit weight.

If a flow net analysis is carried out to calculate flow rates or permeabilities if the pumping

rate is known, from Darcy's law the steady flow under the caisson can be written as:

$$q = 2\pi Rk\frac{s}{\gamma_f}\frac{N_F}{N_H} \tag{4.10}$$

where k is a uniform permeability, s is the suction or difference in total head between the first and last equipotential , γ_f is the fluid unit weight and N_F and N_H are the numbers of flow channels and equipotential drops, representing each the same total head loss. Houlsby and Byrne (2005b) extend the steady flow calculation when differences in permeability of the soil inside the caisson and outside the caisson occur.

$$q = 2Rk_o\frac{s}{\gamma_f}F \tag{4.11}$$

where k_o is the soil permeability outside the caisson and F is a dimensionless factor that accounts for the change in N_F and N_H as a function of $\frac{h}{2R}$ and the permeability ratio $k_f = \frac{k_i}{k_o}$, where k_i is the soil permeability inside the caisson. According to the flow net in Figure 4.3 $N_F = 6$, $N_H = 10$, $\frac{h}{2R} = 0.25$, and $k_f = 1$, resulting in $F = \frac{3\pi}{5} \approx 1.9$, which is slightly higher than the numerical calculations of $F = 1.6$ shown in Figure 4.4. This difference is due to the fact that the flow net was constructed following procedures for plane strain conditions and equations (4.10) and (4.11) and therefore F correspond to axial symmetric conditions. Note that F depends on the permeability ratio rather than on absolute values of permeability. This is an important point for the following analyses of the suction. In addition, no direct measurements of $\frac{k_i}{k_o}$ were possible. Figure 4.5 depicts a caisson being penetrated a depth h under the submerged weight V' and the application of suction s, which are counterbalanced by the shear stresses τ_i and τ_o as well as the end bearing stress at the tip σ'_{end}. The equilibrium of forces acting on the caisson established in (4.1) now includes the suction force sA_i resulting in:

$$\begin{aligned} V' + sA_i =& 2\pi R_o \int_0^h \underbrace{\sigma'_{v\,o}}_{seepage}\, dz(K\tan\delta)_o + 2\pi R_i \int_0^h \underbrace{\sigma'_{v\,i}}_{seepage}\, dz(K\tan\delta)_i + \\ & (\underbrace{\sigma'_{v\,i}}_{seepage} N_q + \gamma' t N_\gamma) 2\pi Rt \end{aligned} \tag{4.12}$$

The suction s is added in equation (4.1) in the left hand side, capturing the assistance effect in the installation process. The flow net shown in Figure 4.3 illustrates how the hydraulic head varies along each flow channel. As a result, outside the caisson the downward flow increases the stresses, whereas inside the caisson the upward flow reduces the stresses.

Houlsby and Byrne (2005b) propose that the change of stresses due to seepage is proportional to the average hydraulic gradients inside and outside the caisson:

$$i_i = \frac{(1-a)s}{\gamma_f h}; \qquad i_o = -\frac{as}{\gamma_f h} \tag{4.13}$$

where γ_f is the fluid unit weight and a is a pressure factor that represents the ratio between the excess pore fluid pressure at the tip of the caisson skirt and next to the base ($0 \leq a < 1$). Alternatively, the excess pore fluid pressures generated by the seepage regime become a function of the suction and the pressure factor as inside the caisson, and $-(1-a)s$ outside the caisson. Therefore, the effective vertical stresses in the soil inside and outside the caisson are modified by seepage according to:

$$\sigma'_{v\,i\,seepage} = \left[1 - \frac{(1-a)s}{\gamma' h}\right]\sigma'_{v\,i}; \quad \sigma'_{v\,o\,seepage} = \left[1 + \frac{as}{\gamma' h}\right]\sigma'_{v\,o} \tag{4.14}$$

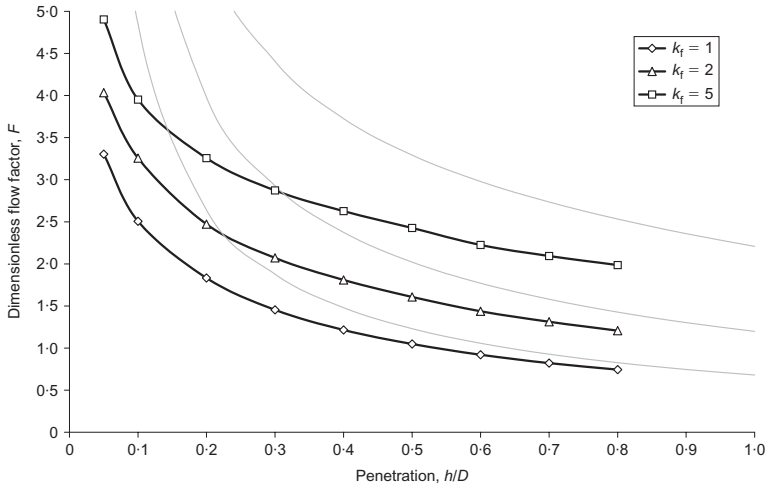

Figure 4.4: Variation of dimensionless flow parameter F. The faint lines correspond to the approximation $F = \frac{(1-a)\pi k_f}{4\left(\frac{h}{2R}\right)}$, with a a pressure factor to be introduced (taken from Houlsby and Byrne (2005b))

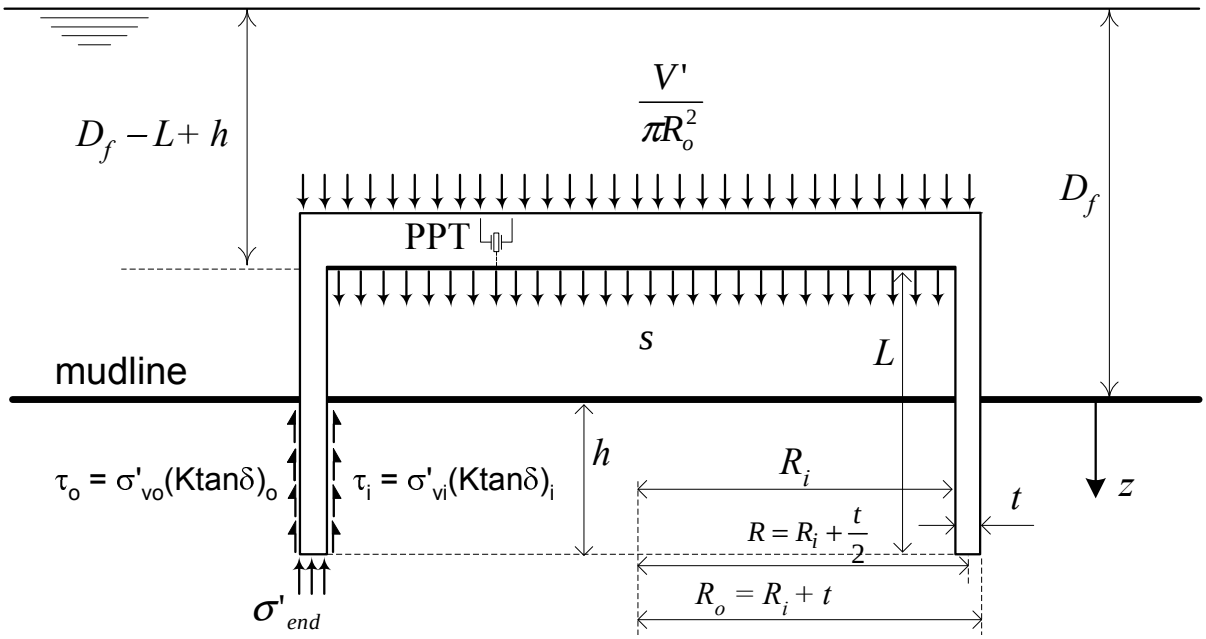

Figure 4.5: Vertical stresses on a suction caisson during installation

where σ'_{vo} and σ'_{vi} correspond to the case without seepage. The excess pore fluid pressure at the tip of the caisson can be obtained from inside or outside as follows:

$$u' = s - \sigma'_{vi} - \sigma'_{vi\,seepage} = s - \frac{(1-a)s}{\gamma' h}\sigma'_{vi}; \quad u' = \sigma'_{vo} - \sigma'_{vo\,seepage} = -\frac{as}{\gamma' h}\sigma'_{vo} \tag{4.15}$$

which reduces to the distribution $-as\frac{z}{h}$ with depth if $\sigma'_{vi} = \sigma'_{vo} = \gamma' z$ as assumed by Houlsby and Byrne (2005b). Replacing (4.14) in the respective σ'_{vi} and σ'_{vo} of expression (4.12) and assuming stresses linearly varying with depth leads to the following expression:

$$\begin{aligned} V' + sA_i &= 2\pi R_o \int_0^h (K\tan\delta)_o \left[1 + \frac{as}{\gamma' h}\right] \sigma'_{vo} dz \\ &+ 2\pi R_i \int_0^h (K\tan\delta)_i \left[1 - \frac{(1-a)s}{\gamma' h}\right] \sigma'_{vi} dz + \left\{\left[1 - \frac{(1-a)s}{\gamma' h}\right] \sigma'_{vi} N_q + \gamma' t N_\gamma\right\} 2\pi R t \end{aligned} \tag{4.16}$$

It is worth pointing out that equation (4.16) reveals that the suction not only contributes as a driving force as in equation (4.12), but also contributes enormously in reducing the stresses at the caisson tip and inside the caisson skirt. Because of the reduced soil resistance at the caisson tip the skirt penetration is possible under a much lower net

vertical load. Solving the integrals results in:

$$V' + sA_i = \left[\gamma' + \frac{as}{h}\right] h^2 (K \tan\delta)_o \pi R_o + \left[\gamma' - \frac{(1-a)s}{h}\right] h^2 (K \tan\delta)_i \pi R_i + \\ + \left[\gamma' - \frac{(1-a)s}{h}\right] (hN_q + tN_\gamma) 2\pi Rt \tag{4.17}$$

Alternatively, the suction can be solved from expression (4.17) resulting in:

$$s = \frac{V' - [\gamma' h^2 (K \tan\delta)_o \pi R_o + \gamma' h^2 (K \tan\delta)_i \pi R_i + \gamma' h N_q 2\pi Rt + \gamma' t N_\gamma \pi Rt]}{ah(K \tan\delta)_o \pi R_o - (1-a)[h(K \tan\delta)_i \pi R_i + (N_q + \frac{t}{h} N_\gamma) 2\pi Rt] - A_i} \tag{4.18}$$

The bracketed expression in the numerator corresponds to the net force required to penetrate a caisson without suction ($F_i + F_o + B_q + B_\gamma$). Multiplying the numerator and the denominator of expression (4.18) by $\gamma' h$ leads to the introduction of the already known forces F_i, F_o, B_q and B_γ in the denominator. In this form a more compact equation for the suction required is obtained:

$$s = \frac{[V' - (F_i + F_o + B_q + B_\gamma)]\gamma' h}{aF_o - (1-a)(F_i + B_q + B_\gamma) - \gamma' h A_i} \tag{4.19}$$

The pressure factor a accounts for the variation of excess pore pressure with skirt depth. Aldwinkle (1994) carried out a numerical analysis using the finite element program I-DEAS, whereby the seepage problem was solved by means of the heat transfer analogy. The analogies are: conductivity ≡ permeability, and temperature gradient ≡ pressure difference. It was assumed that the reduced 'pore pressure' at the tip was a times 'the suction' in the caisson compartment (T = 0°C); at the same level but outside of the caisson the suction was zero (T = 100°C). The a values obtained by Aldwinkle (1994) covered caisson aspect ratios $\frac{h}{2R} \leq 0.33$. Junaideen (2004) (cited by Houlsby and Byrne, 2005b) using almost the same mesh details verified and extended the values of a for $\frac{h}{2R} \leq 0.8$. If seepage provoked by the suction does not change the soil permeability ($k_f = 1$ in Figure 4.6), then the pressure factor a can be approximated by:

$$a = a_1 = c_0 - c_1 \left[1 - e^{-\frac{h}{c_2 2R}}\right] \tag{4.20}$$

with the values $c_0 = 0.45$, $c_1 = 0.36$, and $c_2 = 0.48$. Values of a at $h = 0$ are not important as this represents just the beginning of penetration before suction would be applied. The fact that seepage can change the soil buoyant unit weight implies also that the specific volume can change, and hence the permeability. The permeability k is found to be related to the specific volume υ by means of the Kozeny-Carman equation for fully saturated porous media, which can be expressed as:

$$k = C_s D_s^2 \left(\frac{\gamma_f}{\mu_d}\right) \frac{(\upsilon - 1)^3}{\upsilon} \tag{4.21}$$

where C_s is a shape factor equal to $\frac{1}{2}$ if full flow occurs through a tube, D_s can be interpreted as a representative grain size, normally taken as D_{10}; μ_d and γ_f are the viscosity and unit weight of the fluid as described in Chapter 2. For a soil permeability ratio $k_f = \frac{k_i}{k_o}$ the pressure factor a is expressed by:

$$a = \frac{a_1 k_f}{(1 - a_1) + a_1 k_f} \tag{4.22}$$

Furthermore, the variation of a with h in (4.20) induces a variation in the calculated stresses in (4.14), and hence a variation in k_f. An attempt to include a reduction of only k_i in a soil annulus next to the caisson skirt wall will change the values of a as a function of the annulus dimensions (Aldwinkle (1994) used for example, one seventh of the radius). However, such a refinement in the analysis requires knowledge of how to evaluate the annulus dimensions. Since the suction calculation is very sensitive to a further research is necessary to find out the spatial distribution of the stresses around the caisson caused by seepage.

A general equation to determine the suction can be obtained arranging equation (4.16) in terms of s, as in equation (4.18) and also multiplying the numerator and denominator by $\gamma' h$ as in equation (4.19), resulting in:

$$s = \frac{(2\pi R_o \int_0^h \tau_o z dz + 2\pi R_i \int_0^h \tau_i z dz + (\sigma'_{v\,i} N_q + \gamma' t N_\gamma) A_{rim} - V')\gamma' h}{A_i \gamma' h - 2\pi R_o a \int_0^h \tau_o dz + (1 - a)[2\pi R_i \int_0^h \tau_i dz + (\sigma'_{v\,i} N_q + \gamma' t N_\gamma) A_{rim}]} \tag{4.23}$$

It is worth pointing out that in (4.23) the integrals are the same as for the self-weight penetration. The expression of the suction for the case of exponential distribution of stresses can be obtained from equation (16) in Houlsby and Byrne (2005b). For the case of a non-linear stress distribution as described in section §4.2.2 the integrals in (4.23) become sums in a numerical calculation of stresses, then the suction can be obtained from:

$$s = \frac{\left(2\pi R_o \sum_{j=1}^{n} \tau_{o_j} h_j \Delta h + 2\pi R_i \sum_{j=1}^{n} \tau_{i_j} h_j \Delta h + h_j(\sigma'_{v\,i_j} N_q + \gamma' t N_\gamma) A_{rim} - V' h_j\right) \gamma'}{A_i \gamma' h_j - 2\pi R_o a \sum_{j=1}^{n} \tau_{o_j} \Delta h + (1-a)[2\pi R_i \sum_{j=1}^{n} \tau_{i_j} \Delta h + (\sigma'_{v\,i} N_q + \gamma' t N_\gamma) A_{rim}]}$$
$$\forall n \in \{1, ...N\} \quad \text{where} \quad n = \frac{h}{\Delta h} \quad \text{and} \quad N = \frac{L}{\Delta h} \tag{4.24}$$

4.2.4 Limits to suction assisted penetration

The assistance of suction to install a caisson is limited by the soil resistance. Exceeding a critical value of the suction induces a progressive and irreversible soil failure that consequently halts the caisson penetration. The critical hydraulic gradient i_c that causes a boiling or *piping* condition is given by (Terzaghi and Peck, 1967):

$$i_c = \frac{\gamma'}{\gamma_f} \tag{4.25}$$

A condition of zero effective vertical stress at the caisson tip may trigger and spread around the caisson creating also piping if the critical suction s_{crit} is reached. Clausen and Tjelta (1986) (cited by Feld, 2001) propose the following expression for the critical suction:

$$s_{crit} = \frac{\gamma' h}{1 - \frac{0.68}{1.46\frac{h}{2R}+1}} \tag{4.26}$$

Expression (4.26) was derived from numerical solutions of axial symmetric steady state flow for $\frac{h}{2R} < 0.5$. It can be observed in Figure 4.6 that the pressure factor implicitly suggested in (4.26) as $a = \frac{0.68}{1.46\frac{h}{2R}+1}$ follows a similar trend as in the formulation given in

(4.22), and indeed corresponds to $k_f \approx 2.5$. Additionally, the a expression of Clausen and Tjelta (1986) still is valid for $0.5 < \frac{h}{2R} < 1$. Replacing the critical hydraulic gradient

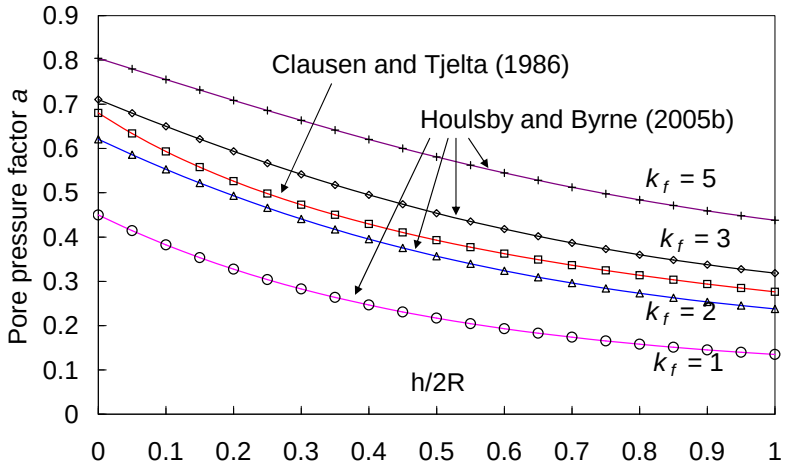

Figure 4.6: Variation of the pressure factor a with $\frac{h}{2R}$ comparing expressions by Clausen and Tjelta (1986) with Houlsby and Byrne (2005b)

(4.25) in (4.13) or alternatively making $\sigma'_{v\,i\,seepage} = 0$ in (4.14) a general expression can be obtained,

$$s_{crit} = \frac{\gamma' h}{1 - a} \tag{4.27}$$

In terms of the limit depth of penetration h_{crit}, expressions can be obtained replacing s_{crit} from equation (4.27) into s in equation (4.16). For example, for the particular case of a linear stress distribution, solving for h in equation (4.16) leads to:

$$h_{crit} = \frac{\gamma' A_i + \sqrt{(\gamma' A_i)^2 + 4\gamma'(1-a)(K\tan\delta)_o \pi R_o V'}}{2\gamma'(K\tan\delta)_o \pi R_o} \tag{4.28}$$

In the unfavourable case of $V' = 0$ N, and assuming $R_i \approx R_o \approx R$, h_{crit} becomes equal to:

$$h_{crit} = \frac{R}{(K\tan\delta)_o} \tag{4.29}$$

For an usual value of $(K\tan\delta)_o \cong 0.5$, h_{crit} becomes equal to the caisson diameter $2R$. From equation (4.28) h_{crit} increases with V' and also with h since a diminishes with depth. If the exponential distribution of stresses $\sigma'_{v\,o} = \gamma' Z_o \left(e^{\frac{z}{Z_o}} - 1\right)$ (where $Z_o = \frac{R_o(m^2-1)}{2(K\tan\delta)_o}$ with m >1 defining a constant extension of soil arching as a multiple of the radius mR_o) is

used in expression (4.16) the following equation results:

$$2\pi R_o(K\tan\delta)_o\gamma' Z_o^2\left[e^{\frac{h}{Z_o}}-1-\frac{h}{Z_o}\right]-\gamma' A_i h - V'(1-a)=0 \tag{4.30}$$

The solution for h_{crit} has to be found using a numerical method and iterating for h to obtain the variation of a with depth. If $\sigma'_{v\,o}$ is obtained numerically as in section §4.2.2, then the critical penetration depth is given by:

$$h=\frac{2\pi R_o(K\tan\delta)_o\sum_{j=1}^{n}\sigma'_{v\,o_j}h_j\Delta h - V'(1-a)}{\gamma' A_i} \qquad \forall n\in\{1,...N\} \quad \text{where} \quad n=\frac{h}{\Delta h} \quad \text{and} \quad N=\frac{L}{\Delta h} \tag{4.31}$$

where h_{crit} is found when h coincides with the penetration h_j.

Another form to evaluate a limit to suction is by calculation of a reversed bearing capacity failure. This has been established for suction caissons in clay under uplift loading by Fuglsang and Steensen-Bach (1991) and employed by Deng and Carter (2000), Randolph and House (2002), House (2002) and Houlsby and Byrne (2005a). Whilst for caissons in clay the response relies on undrained conditions, in sand a fully drained condition is expected. The failure mechanism moves towards the inside of the caisson when the stresses outside the caisson overcome the stresses inside the caisson during suction installation. To avoid this type of failure the following condition must be verified:

$$\sigma'_{v\,o} < N_q\sigma'_{v\,i} \qquad \forall \quad h\in(0,L] \tag{4.32}$$

substituting (4.14) into (4.32) for the linear and exponential stress distributions results in:

$$\frac{\left[1-\frac{(1-a)s}{\gamma' h}\right]N_q}{\left[1+\frac{as}{\gamma' h}\right]}>1, \quad \frac{\left[1-\frac{(1-a)s}{\gamma' h}\right]Z_i(e^{\frac{h}{Z_i}}-1)N_q}{\left[1+\frac{as}{\gamma' h}\right]Z_o(e^{\frac{h}{Z_o}}-1)}>1 \qquad \forall \quad h\in(0,L] \tag{4.33}$$

where $Z_i = \frac{R_i}{2(K \tan \delta)_i}$. It is assumed in the above expressions that N_q used in the downward form of bearing capacity problems is also valid for the reversed form.

4.3 EXPERIMENTAL RESULTS

4.3.1 Pushing installation into loose and dry sand

A series of pushing installation tests were performed prior to moment loading tests. It is worth pointing out that the interest of determining the maximum vertical load V_o experienced by the foundation has its roots in the critical state soil mechanics interpretation of triaxial tests, where the maximum load is analogous to the preconsolidation pressure.

In the laboratory, the vertical load V' was monitored throughout every test at an interval of half a second for a penetration rate of $\dot{h} = 0.5$ mm/s. When lid contact occurred the vertical stepper motor of the VMH loading rig was stopped. However, it is difficult to stop the installation exactly at the lid contact or contact load V_c, and in the best case a small increase over V_c was obtained. On the contrary, if the penetration is stopped before lid contact, there will be uncertainty of whether the skirt penetrated completely or not. As a consequence, there was always a difference between V_c and V_o. To analyse the data V_o should rigorously be adopted as the maximum value of the vertical load experienced by the foundation. Nevertheless, the analysis is more consistent if an intrinsic property of the foundation as the *contact* vertical load V_c is considered instead of random values of V_o. They were in average around 30% larger than V_c (Tables 4.1 and 4.2). As a result, the values of V_c and h_c will be adopted in the subsequent analyses.

Load-penetration curves are shown in Figures 4.7(a) and 4.7(b), where it is possible to observe the variation of V' with h as well as V_c and V_o. Figures 4.8(a) and 4.8(b) show two normalisations for the previous plots: $\frac{V'}{V_c}$ and $\frac{V'}{\gamma_d (2R)^3}$. These normalisations prove to be very effective in unifying results from different soil densities and was possible to include both in the same plot because V_c and γ_d (or V_c and R_d) can be correlated as

Table 4.1: Pushing installation tests of caisson A in dry, loose Leighton Buzzard sand

Test	γ' kN/m^3	R_d %	υ	V_c N	h_c mm	V_o N	h_o mm	V_t N	h_t mm
FV1_1_1	15.16	20	1.714	473	143.7	726	145.2	-55	142.7
FV15_2_1	15.05	16	1.727	482	144.4	606	145.7	-55	144.6
FV26_3_1	15.37	28	1.692	575	143.2	728	145.0	-56	143.4
FV27_3_1	15.37	28	1.692	558	144.3	822	145.9	-	-
FV29_3_1	15.37	28	1.691	554	143.7	868	145.5	-	-
FV30_4_1	15.52	34	1.675	665	134.7	904	136.4	-56	134.7
FV31_4_1	15.50	33	1.677	654	135.2	925	136.3	-	-
FV32_4_1	15.24	23	1.706	561	143.5	844	145.5	-	-
FV33_4_1	15.24	23	1.706	541	144.5	651	145.4	-	-
FV34_5_1	15.18	21	1.713	546	145.0	705	146.2	-51	143.6
FV35_5_1	15.34	27	1.695	595	145.2	817	146.6	-52	143.5
FV36_5_1	15.37	28	1.691	613	143.7	774	145.5	-52	143.5
FV37_5_1	15.37	28	1.691	613	143.3	870	145.2	-52	143.4
FV57_10_1	15.60	37	1.666	721	141.2	975	143.4	-	-
FV58_10_1†	15.60	37	1.666	729	141.7	2388	146.4	-61	145.0
FV60_10_1	15.60	37	1.666	677	142.3	802	143.7	-55	140.2
FV61_10_1	15.60	37	1.666	695	143.7	934	144.6	-64	143.2
FV81_14_1	15.85	46	1.640	726	139.5	786	141.3	-47	130.0
FV82_14_1	15.85	46	1.640	784	141.4	906	142.5	-53	134.2
FV84_14_1	15.85	46	1.640	795	141.4	983	143.0	-60	139.5
FV85_15_1	15.99	50	1.626	783	141.2	1013	142.6	-48	128.9
FV86_16_1	15.11	18	1.721	458	146.3	798	148.8	-	-
FV87_16_1	15.11	18	1.721	461	145.6	703	148.1	-59	146.6
FV88_16_1	15.11	18	1.721	503	144.3	884	147.4	-57	144.2
FV89_16_1	15.11	18	1.721	478	143.8	693	147.6	-58	146.0
FV90_17_1	15.03	15	1.730	463	145.9	751	147.9	-51	143.0
FV91_17_1	15.03	15	1.730	468	146.0	670	147.7	-	-
FV92_17_1	15.03	15	1.730	491	145.6	667	147.0	-	-
FV93_17_1	15.03	15	1.730	473	144.3	791	147.3	-	-
FV94_18_1	15.00	14	1.733	445	146.5	663	148.0	-	-
FV95_18_1	15.00	14	1.733	456	145.6	690	147.9	-	-
FV97_18_1	15.00	14	1.733	465	144.0	676	146.6	-	-
FV99_19_1	15.01	14	1.732	430	143.2	645	148.6	-	-
FV100_19_1	15.01	14	1.732	496	145.0	650	147.5	-	-
FV101_19_1	15.01	14	1.732	473	144.5	661	147.0	-53	145.1
FV107_21_1	14.96	12	1.738	460	145.2	586	146.9	-	-
FV108_21_1	14.96	12	1.738	483	143.7	602	145.9	-	-
FV109_21_1	14.96	12	1.738	487	143.4	526	145.1	-	-
FV111_22_1	15.23	23	1.707	557	145.3	745	149.2	-62	145.1
FV113_22_1	15.23	23	1.707	530	147.8	759	150.2	-	-
FV116_22_1	15.23	23	1.707	573	144.4	708	147.6	-	-
FV118_22_1	15.23	23	1.707	538	145.2	700	147.9	-	-
FV121_23_1	15.10	18	1.722	521	145.8	756	149.6	-55	144.7
FV123_23_1	15.10	18	1.722	534	145.4	638	148.5	-47	136.1
FV125_23_1	15.10	18	1.722	560	145.7	790	148.9	-51	137.9
FV127_23_1	15.10	18	1.722	530	144.1	747	148.5	-43	128.9
FV130_24_1	15.29	25	1.700	582	145.4	764	148.4	-61	144.5
FV132_24_1	15.17	21	1.714	513	147.2	735	150.8	-58	148.2
FV134_24_1	15.17	21	1.714	528	145.5	707	147.8	-62	145.9
mean	15.23	23	1.708	558	144.3	780	146.2	-55	141.8
st deviation	0.27	10	0.030	98	2.8	247	3.2	5	5.2

†vertical loading tests until rig capacity reached

Table 4.2: Pushing installation tests of caisson B in dry, loose Leighton Buzzard sand

Test	γ' kN/m^3	R_d %	υ	V_c N	h_c mm	V_o N	h_o mm	V_t N	h_t mm
FV38_6_1	15.27	24	1.702	540	199.7	696	202.0	-75	200.5
FV40_6_1	15.27	24	1.702	608	198.5	792	200.8	-70	198.7
FV41_6_1	15.33	27	1.696	653	198.4	728	200.7	-68	199.1
FV42_6_1	15.27	24	1.702	557	197.9	681	200.1	-60	197.0
FV45_7_1	15.35	27	1.694	676	197.4	777	198.8	-68	198.3
FV46_7_1	15.35	27	1.694	663	198.1	817	200.0	-78	198.4
FV47_7_1	15.35	27	1.694	624	197.8	770	199.7	-74	198.4
FV48_7_1	15.40	29	1.688	700	196.8	853	199.3	-74	197.2
FV49_8_1	15.37	28	1.692	623	197.7	688	198.8	-77	198.7
FV50_8_1	15.37	28	1.692	676	197.7	852	199.6	-76	197.0
FV51_8_1	15.37	28	1.692	655	199.0	778	200.5	-80	199.6
FV52_8_1	15.37	28	1.692	668	197.6	819	199.6	-80	197.9
FV53_9_1	15.46	32	1.681	695	196.3	938	198.6	-81	198.4
FV54_9_1	15.46	32	1.681	724	195.9	897	198.6	-80	196.6
FV55_9_1	15.46	32	1.681	640	197.2	790	199.3	-75	199.3
FV56_9_1	15.46	32	1.681	698	195.6	910	198.3	-78	196.8
FV101_19_2	15.10	18	1.722	483	197.7	653	200.5	-53	196.6
FV102_20_1	15.00	14	1.733	428	202.4	606	205.6	-67	204.7
FV103_20_1	15.00	14	1.733	417	202.9	535	204.7	-	-
FV110_22_1	15.10	18	1.722	443	203.2	518	205.2	-72	191.4
FV112_22_1	15.00	14	1.733	433	203.0	500	204.6	-67	202.0
FV117_22_1	15.10	18	1.722	469	203.1	578	204.6	-71	-
FV119_22_1	15.23	23	1.707	557	198.7	799	201.7	-	-
FV120_23_1	15.05	16	1.727	421	203.6	567	205.8	-	-
FV122_23_1	15.10	18	1.722	443	204.4	563	206.4	-74	206.8
FV124_23_1	15.10	18	1.722	467	202.2	575	204.4	-64	198.7
FV126_23_1	15.10	18	1.722	459	200.4	581	203.5	-71	204.2
FV129_24_1	15.11	18	1.721	465	201.6	559	203.1	-81	194.4
FV131_24_1	15.11	18	1.721	460	201.8	629	204.8	-65	203.2
FV133_24_1	15.11	18	1.721	467	200.5	629	203.8	-68	201.2
FV135_24_1	15.11	18	1.721	470	201.4	650	204.8	-69	203.0
mean	15.23	23	1.708	553	199.7	700	202.0	-72	199.4
st deviation	0.16	6	0.018	107	2.6	127	2.7	7	3.4

shown in Figures 4.9(a) and 4.9(b). The mean error in the estimation of $\frac{V_c}{\gamma_d(2R)^3}$ using a linear regression are 0.031 ± 0.008 (Figure 4.9(a)) and 0.15 ± 0.05 (Figure 4.9(b)), for a 95% confidence level for the mean and assuming an infinite number of measurements.

To evaluate the theoretical predictions with the experimental results, test FV81_14_1A was chosen as a representative example. In the calculations a peak angle of friction ϕ'_{peak} was estimated using the procedure suggested by Bolton (1986). Using a direct shear apparatus Lings and Dietz (2005) determine interface friction angles δ between 10.8° and 13.3° for a medium sub-rounded sand with relative densities between 23% and 78% and under a normal stress of 25 kPa. The surface to which they sheared the sand corresponded to a

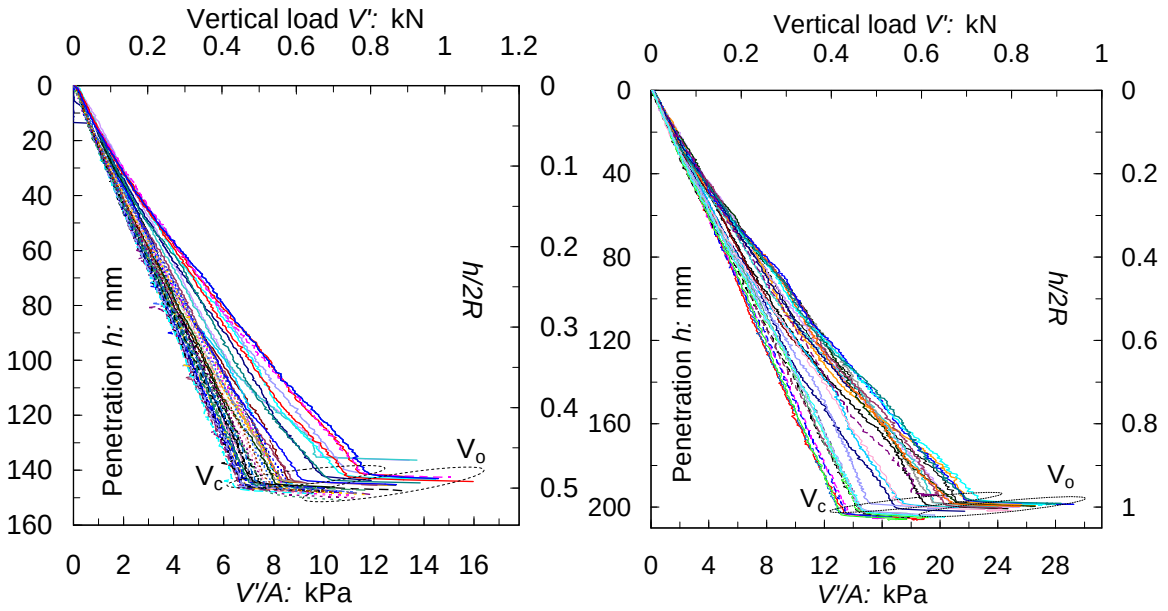

(a) Caisson A: $\frac{L}{2R} = 0.5$, $\frac{t}{2R} = 1.16\%$ (b) Caisson B: $\frac{L}{2R} = 1$, $\frac{t}{2R} = 1.67\%$

Figure 4.7: Pushing installation tests

material with a maximum roughness R_{max} of 3.85 μm. A value $R_{max} = 4$ μm was found for a dural plate (Chapter 2), and a value of R_{max} of the same order of magnitude was assumed to hold for the aluminium caissons A and B. Therefore, a compromise value of $\delta = 12.5°$ is adopted.

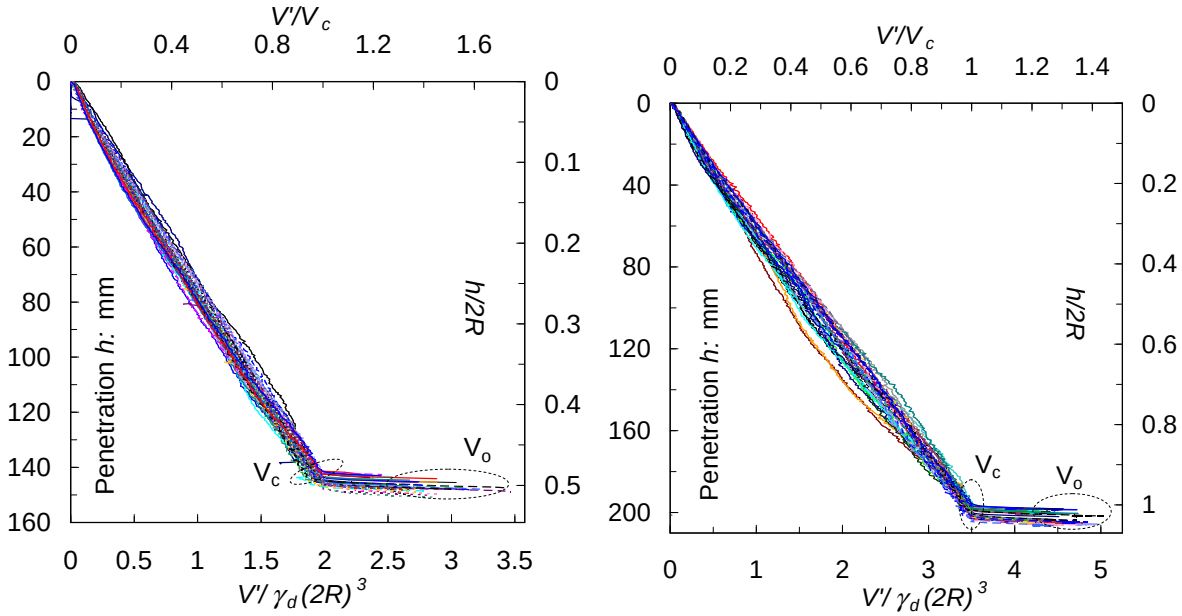

(a) Caisson A: $\frac{L}{2R} = 0.5$, $\frac{t}{2R} = 1.16\%$ (b) Caisson B: $\frac{L}{2R} = 1$, $\frac{t}{2R} = 1.67\%$

Figure 4.8: Normalised results of the pushing installation tests showing V_c and V_o

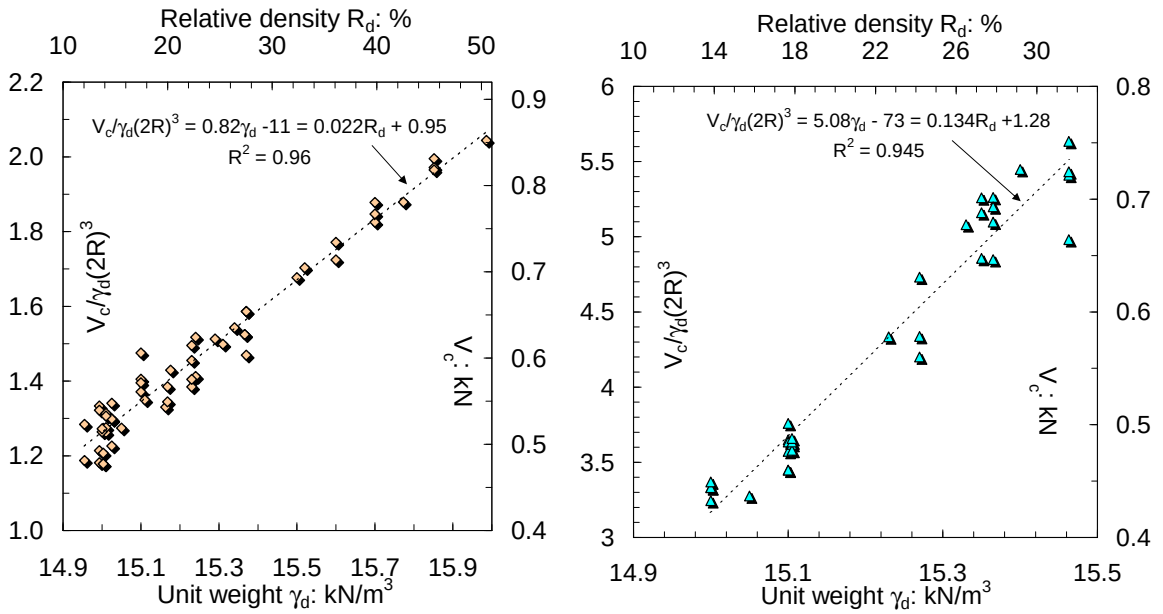

(a) Caisson A: $\frac{L}{2R} = 0.5$, $\frac{t}{2R} = 1.16\%$ (b) Caisson B: $\frac{L}{2R} = 1$, $\frac{t}{2R} = 1.67\%$

Figure 4.9: Relationships between the contact vertical load V_c and the soil unit weight γ_d and the relative density R_d

It can be observed in Figure 4.11(a) that the prediction obtained is poor when a linear stress distribution is considered ($\sigma'_{v\,geostatic}$ in Figure 4.10(a)). The frictional forces are equal $F_i = F_o$ since a similar friction parameter $K \tan\delta$ was used inside and outside. The exponential stresses shown in Figure 4.10(a) increase over the geostatic after 20 mm of penetration, which is the effect of considering soil arching. This results in a better prediction of V' as Figure 4.11(b) demonstrates. The value of m can be changed to increase

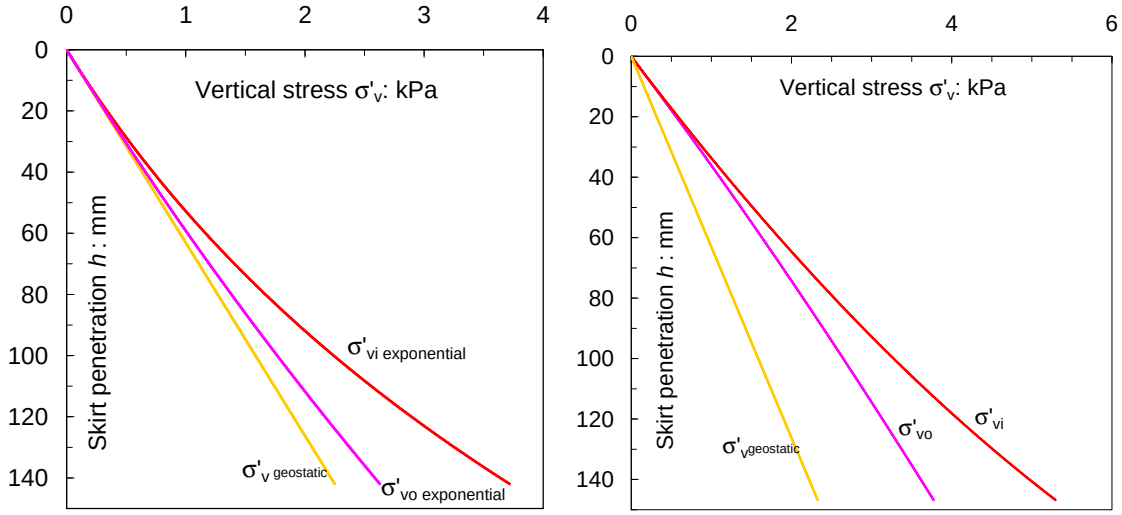

(a) Linear and exponential (b) Linear and non-linear

Figure 4.10: Vertical stress distributions

$\sigma_{v\,o}$, but the prediction of V' will not significantly improve.

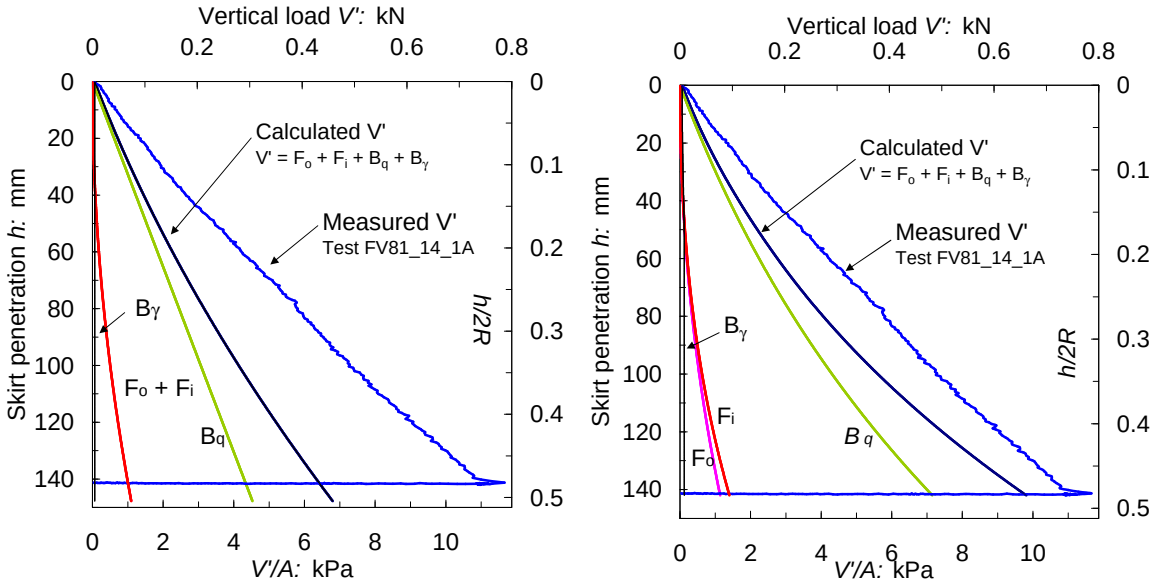

(a) Linear stress distribution

(b) Exponential stress distribution, $m = 2$

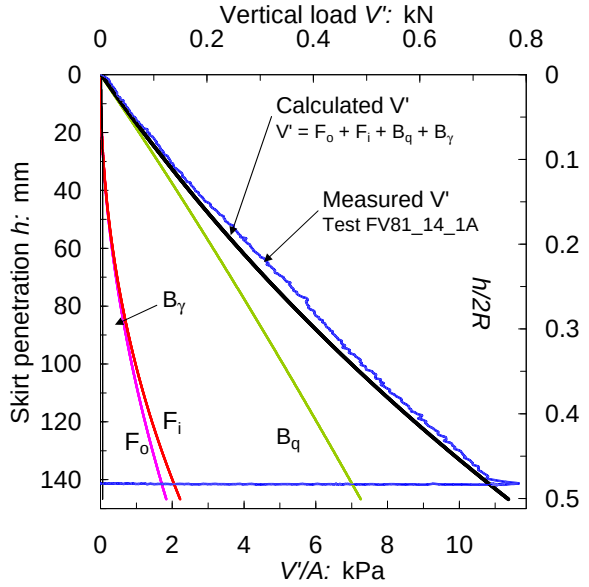

(c) Non-linear stress distribution, $f_o = f_i = 1$

Figure 4.11: Measured and calculated load-penetration response assuming the following parameters: $\gamma_d = 15.85$ kN/m^3, $\phi'_{peak} = 36.8°$ and $\delta = 12.5° \Rightarrow K \tan\delta = 0.47$

Higher non-linear stresses were obtained when the soil arching was taken for a radius linearly varying with depth at a rate of $f_i = f_o = 1$. Figure 4.10(b) shows that the vertical stresses inside and outside the caisson increase over the geostatic from the onset of the penetration and again $\sigma'_{v\,i} > \sigma'_{v\,o}$. Figure 4.11(c) shows that using the non-linear stresses led to a good agreement between the measured and calculated V'. The values of f_i or f_o could be slightly changed to improve the prediction, however, the intention here is to show the convenience of increasing non-linearly the stresses according to the formulation

presented in section §4.2.2. It is worth pointing out that in this example the chosen value of N_γ was irrelevant (in the three stress distributions) since the surcharge and friction components are substantially higher than the soil weight component.

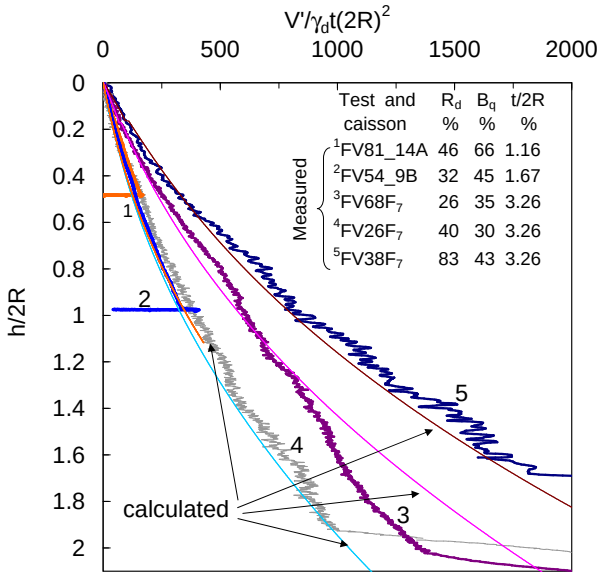

Figure 4.12: Measured and calculated normalised load-penetration curves for three different caissons assuming non-linear stresses with $f_i = f_o = 1$. In test FV54_9B the parameter values adopted were: $\gamma_d = 15.46$ kN/m^3, $\phi'_{peak} = 34.7°$ and $\delta = 14° \Rightarrow K \tan\delta = 0.49$

Figure 4.12 compares installation curves of tests carried out with caisson F_7 (Chapter 3) in loose and dense Leighton Buzzard sand and loose Dogs Bay sand, with installation curves of tests carried out with caissons A and B. Note that owing to the large influence of the surcharge component B_q (especially in tests with caissons A and B), the normalised vertical load should include the thickness ratio to achieve similarity. Using the dimensionless relationship: $\frac{V'}{\gamma_d\left(\frac{t}{2R}\right)(2R)^3} = \frac{V'}{\gamma_d t(2R)^2}$, the installation curves of three different caissons compare relatively well for loose Leighton Buzzard sand (tests FV81_14A, FV54_9B and FV26F$_7$). The tests in very loose calcareous sand (FV68F$_7$) and in dense Leighton Buzzard sand have higher normalised vertical loads due to the higher angles of friction. For the former the higher value of $\phi'_{peak} = \phi'_{cs}$ is due to the angularity of the grains, whilst for the silica sand is due to soil dilation. Calculated curves using non-linear stresses show that a reasonable good prediction can be achieved. The values of unit weight and peak angle of friction for the tests with caisson F$_7$ are presented in Chapter 3; a value of $\delta = 12.5°$ was adopted.

4.3.2 Drained pullout tests

Models developed for the study of shallow foundations do not include tensile capacity, for instance, Model B and Model C described in Chapter 1. However, from Figures 4.13(a) and 4.13(b) it can be observed that fully drained pullout tests of caissons A and B exhibited tensile capacity due to friction developed on the skirt. Values of maximum tensile loads V_t and displacements h_t are listed in Tables 4.1 and 4.2. Pullout tests were carried out under a rate of $\dot{h} = 2$ mm/s, but with different load histories (monotonic and/or cyclic rotational or translational tests). Only test FV58_10_1A was carried out exclusively to explore the vertical load capacity, but because the caisson was more deeply embedded due to the larger V_o applied the maximum tensile load V_t was slightly higher. It

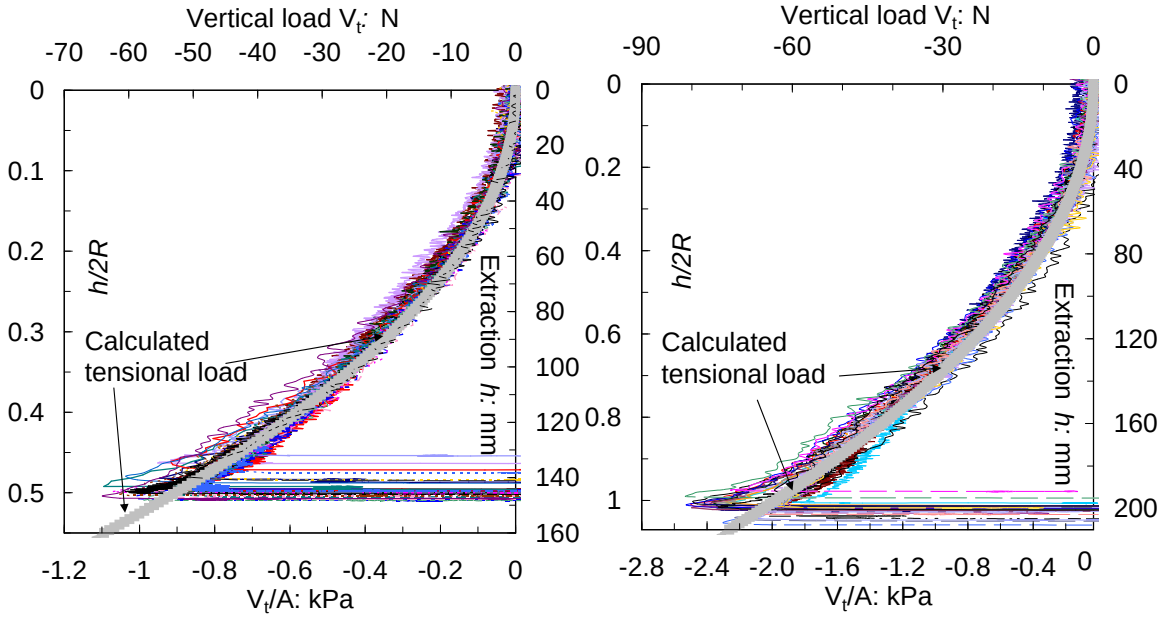

(a) Caisson A (b) Caisson B

Figure 4.13: Measured and calculated drained pullout curves assuming: $\gamma_d = 15.2$ kN/m^3, $\phi'_{cs} = 33°$ and $\delta = 18° \Rightarrow K_A \tan\delta = 0.18$

can be concluded that, independent of the load history, a very small mobilised extraction ($h = h_o - h_t$) is required to trigger the maximum tensile capacity. After the maximum tensile capacity is reached the tensile load decreases with further extraction of the caisson. The calculated pullout-extraction curves using equation (4.4) are shown in Figures 4.13(a) and 4.13(b). The calculation of V_t depends strongly on the value of $K_A \tan\delta$ adopted. The parameter values assumed attempt to represent an average of all tests. The prediction

agrees with the measured curves in spite of the soil disturbance caused by shearing during installation and subsequent moment loading. The disturbance was diminished since the soil was always in a loose state.

4.3.3 Pushing installation into dense saturated sand

Before studying suction assisted installation, it is felt important to investigate pushing installation under saturated conditions. This will allow a comparison between both installation methods and also with those test results in dry and loose sand.

It is necessary to clarify that the use of V' does not refer to an effective load as if it were an extension of the principle of effective stresses by Terzaghi. The use of the dash, as before, must be interpreted as the submerged weight of the whole structure plus appurtenances. The effective stresses are transmitted only through the soil skeleton, whereas loads on the caisson foundation can be related by equilibrium.

Table 4.3 summarises soil and conditions of the tests performed with caissons C and A, where D_f corresponds to the height of fluid above the mudline, t_p is the total time required to install the caisson and $\dot{h}$ is the constant penetration rate at which both caissons were pushed into the ground. Measured and calculated load-penetration curves are shown in Figures 4.14(a) and 4.14(b) for two groups of similar tests, which allowed for only one calculation for each caisson. The calculation procedure developed in section §4.2.2 for non linear stresses was used to estimate V' as the sum of $F_i + F_o + B_q + B_\gamma$. Figures 4.14(a) and 4.14(b) show clearly that the major contribution is done by the surcharge component B_q, which increased even more for the larger caisson A. On the other hand the weight component B_γ is practically negligible (it is next to left ordinate axis) despite the greater than twofold increase in the thickness ratio $\frac{t}{2R}$ for caisson A. Finally, it can be observed that a very good agreement exists between the theory and the experimental results for both caissons. A relevant implication of this is that values of V_o can be predicted properly by this theory, which is crucial for a successful application of hyperplasticity theories.

Table 4.3: Data and parameters for load-penetration calculations of pushing installation tests

Test and caisson	γ' kN/m^3	R_d %	ϕ' °	δ °	$K\tan\delta$	D_f mm	$\dot{h}$ mm/s	t_p min	h_o mm	V_o N
FV2_4_1C†	9.76	74	40.5	17	0.75	60	0.5	3	87	258
FV3_4_1C†	9.48	64	37.2	0	0	121	0.016	105	98	28
FV6_3_1C	9.70	75	44.1	15	0.76	130	0.5	3.2	97	403
FV7_1_1C	9.66	74	44.1	15	0.76	130	0.5	3.3	101	414
FV7_5_1C	9.66	74	44.1	15	0.76	122	0.5	3.3	102	422
FV7_2_1A	9.66	74	44.1	14	0.70	130	0.4	5.5	131	1715
FV7_4_1A	9.66	74	44.1	14	0.70	136	0.2	11.4	136	1537
FV8_2_1A	9.88	81	44.1	14	0.70	128	0.2	10.6	126	1641

†tests in oil-saturated Baskarp Cyclone sand, remainder tests in water-saturated Redhill sand

For example, V' was calculated as approximately 0.4 kN for caisson C and as 1.6 kN for caisson A (Table 4.3 shows V_o values obtained directly from the tests).

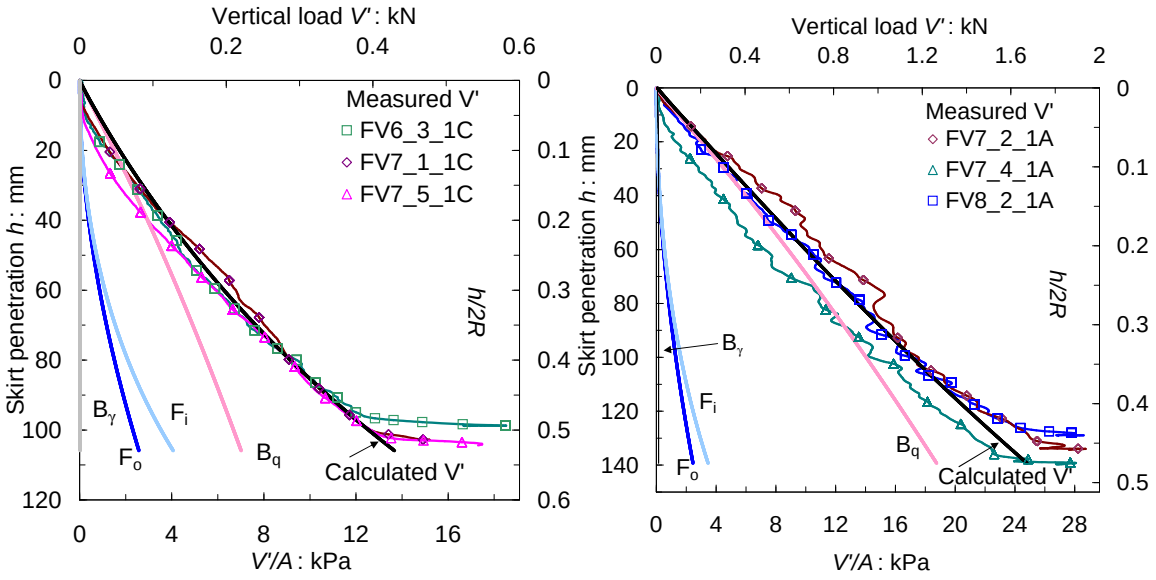

(a) Caisson C (b) Caisson A

Figure 4.14: Measured and calculated load-penetration curves of pushing installation tests assuming $f_i = f_o = 1$, $\gamma' = 9.66$ kN/m^3, $\phi'_{peak} = 44.1°$, $\delta = 15°$ and $14° \Rightarrow K\tan\delta = 0.7$ and 0.76

Although the bleed valve was kept open during all the pushing installation tests an increase in pore pressure with penetration was observed. Figure 4.15(a) shows excess pore pressure (over the hydrostatic) recorded underneath the caisson lid. This was caused by insufficient section area of the bleed valve to compensate the rate of water flowing out the caisson with the penetration rate. However, this transient excess pore pressure increment dissipated once the installation ended. Note in Table 4.3 the very low value of V_o obtained in test FV3_4_1C. According to estimations of V_o using the theory already

presented it can be hypothesized that the only way to achieve such a low value is with frictional forces tending to zero due to $\delta \rightarrow 0$ as a result of the very low penetration rate and high viscosity fluid. As stress is expected to decrease with strain rate, it would be similarly expected that very low penetration rates would reduce friction. Moreover, it seems that a high viscosity fluid might act as a lubricant under the vertical penetration and interface conditions, which may also be a cause for the reduction of friction.

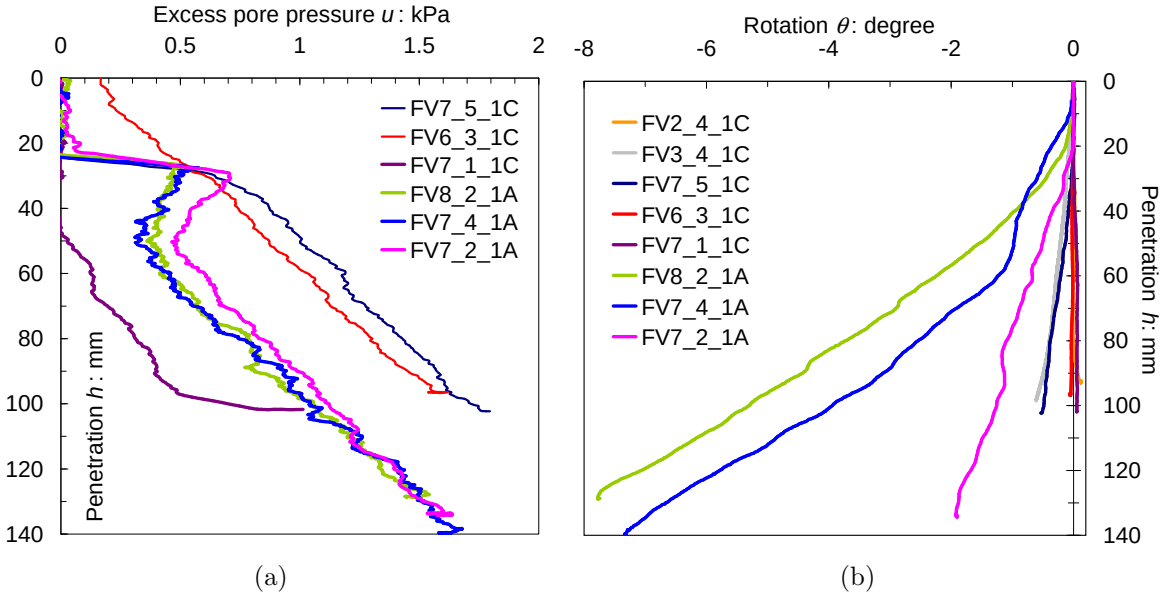

Figure 4.15: (a) Measured excess pore pressures during pushing penetration, and (b) rotation of caisson during pushing penetration. See details of the tests in Table 4.3

Figure 4.15(b) shows that caisson A rotated during penetration more than caisson C, rotating up to 8°. The negative sign in the plot is because of the counterclockwise rotation. The sign of the rotation is not important, as under this loading no rotation would be expected, and the measured rotation is just a measure of experimental variability. Rotation started once fluid flowing out of the caisson through the open vent created an upward force that due to the eccentricity caused a moment, which became larger with depth and especially for caisson A. Positive moment caused negative rotation because the program subroutine instructs the caisson to rotate opposite to counterbalance the positive increase of horizontal load H and moment M during vertical loading. This resulted in the reduction of H and M by translating and rotating the caisson in the opposite direction. Low penetration rates favoured the caisson tilting too since the counterbalance process occurs for a longer period of time. Initial penetration is caused by the structure's self-weight,

therefore, tilting can become an issue if eccentric loads act on the caisson. In the next section it will be seen that caissons penetrate straight naturally using suction, but if the caisson is initially rotated suction will not correct that inclination.

4.3.4 Suction installation results in dense sand

The theory presented in section §4.2.3 to predict the required suction to assist the installation of caissons requires experimental results for calibration and validation. Preliminary comparisons between this theory and four case records and one series of laboratory tests were presented by Houlsby and Byrne (2005b). The database used for the calculations is reproduced in Table 4.4, where values of δ have been deduced using equation (4.5) and $K \tan \delta$. The first two cases correspond to trial tests at Tenby and Sandy Haven, South Wales. The suction installation results at Tenby demonstrated the importance of determining the limits of suction-assisted penetration. The caisson could not be penetrated into the ground past 1.4 m because of piping failure. The other two cases involved caisson foundations for the jacket structures: Draupner E and Sleipner T (Tjelta, 1994; 1995). These cases correspond to much larger caissons and also to much higher vertical loads than in the trial tests. Latterly, Houlsby *et al.* (2006) add new data from suction caisson installation during field trials at Luce Bay, Scotland. The theory performs reasonably well for those cases analysed. It was concluded that for successful predictions k_f should be between 2 and 3, and $K \tan \delta = 0.54 \pm 0.09$ for unitary stress distribution factors ($f_i = f_o = 1$). An exception was the high value of $K \tan \delta$ for the trials in Luce Bay, which may correspond to a high roughness of the skirt wall δ or a compensation for not using a higher value of k_f.

Whilst Table 4.4 shows a range of data there is still a pressing need for additional studies of suction-penetration of caissons under diverse conditions, in particular different caisson geometries, soil properties and submerged weights. Furthermore, investigation of the effect of the installation method on the subsequent loading performance must also be considered. The foundation response to subsequent monotonic or cyclic lateral loading

Table 4.4: Data and parameters for suction calculations installation tests (taken from Houlsby and Byrne (2005b) and Houlsby *et al.* (2006))

Location	$2R$ m	L m	t mm	V' kN	γ' kN/m^3	ϕ' °	δ °	$K \tan\delta$	k_f
Tenby	2	2	8	10	8.5	40	11	0.48	3
Sandy Haven	4	2.5	20	100	8.5	40	11	0.48	2
Draupner E	12	6	45	6622	8.5	44	12	0.63	3
Sleipner T	15	5	45	12000	8.5	45	15	0.8	3
Laboratory	0.15	0.2	1.65	†	8.5	45	9	0.45	2.5
Luce Bay	1.5, 3	1, 1.5	8	7, 60	10.3	45	19	1	3

†45, 85, 165 ($\cdot 10^{-3}$)

will be related to whether the soil strength was modified or not during installation. Consequently, a series of installation tests using suction were planned covering a range of different caisson geometries, soils and submerged weight V'. Chapters 5, 6 and 7 are devoted to loading of caissons after installation. A summary of the parameters assumed

Table 4.5: A summary of parameters used in the calculations

Test and caisson	V' N	D_f mm	γ' kN/m^3	R_d %	ϕ °	δ °	$K \tan\delta$	k_f
FV1_2_1E†	5	46	10.25	90	43	15	0.73	2.7
FV10_4_1D	45	200	10.10	89	46.3	15	0.85	1.3
FV3_1_1C†	-4	46	9.93	80	41.5	15	0.69	2.7
FV9_4_1C	7	160	10.21	92	46.8	15	0.88	2.6
FV6_5_1C	7	115	9.70	75	44.3	15	0.78	2.8
FV9_2_1C‡	40	180	10.21	92	46.8	15	0.88	2.8
FV9_1_1C	62	185	10.21	92	46.8	15	0.88	2.8
FV9_5_1A	14	202	10.21	92	46.8	14	0.81	3.5
FV10_3_1A	16	180	10.10	89	46.3	14	0.80	3.4
FV7_3_1A	65	140	9.66	74	44.1	14	0.72	8
FV10_2_1A	62	204	10.10	89	46.3	14	0.80	3.4
FV7_1_3A	125	130	9.66	74	44.1	14	0.72	10
FV10_1_1A	117	193	10.10	89	46.3	14	0.80	3.4

†carried out in oil-saturated Baskarp Cyclone sand
‡caisson initially tilted 4°

for the suction calculations is listed in Table 4.5. The values of angle of friction have been estimated using the procedure proposed by Bolton (1986) to calculate peak friction angles. The interface angles δ have been assumed according to value ranges presented by Lings and Dietz (2005) (section §4.3.1). Additionally, Table 4.6 includes information of the suction variation with penetration $\frac{ds}{dh}$ (which is not constant, but a relatively fair constant variation can be assumed at the end of the installation), suction rate $\dot{s}$, penetration rate $\dot{h}$, time during suction application t_s, penetration by self weight h_p, final penetration h_o, estimated penetration by self weight h_{pe} and calculated V_o. The recorded

suction underneath the lid with a pore pressure transducer PPT was corrected to obtain the differential pressure (see Chapter 2 for details of the suction system used), which is the difference between the pressure in the caisson compartment and the pressure in the fluid outside the caisson at the same level, according to Figure 4.5 the corrected suction results in:

$$s = s_{ppt} - \gamma_f(D_f - L + h) \tag{4.34}$$

where γ_f is the unit weight of the fluid equal to 9.8 kN/m^3 for water and 9.4 kN/m^3 for the silicon oil. The range of suction applicable diminishes with D_f, but even if more suction were applied there is a maximum available suction given by:

$$s_{available} = p_a + \gamma_f D_f - p_{cav} \tag{4.35}$$

where p_a is the atmospheric pressure ($\approx$ 101.3 kPa) and p_{cav} is the cavitation pressure ($\approx$ 100 kPa). Therefore, the available suction relies mostly on the fluid height D_f, without which suction is very limited or maybe insufficient to install successfully a suction caisson.

Test FV10_2_1A was selected to compare the different calculations of suction presented in section §4.2.3. The measured suction-penetration curve shown in Figure 4.16(a) indicates that the suction was applied after an initial pushing penetration h_p = 20 mm, obtained when V' = 62 N (the calculated penetration for this load is h_{pe} = 4 mm). Subsequently, the suction commences under the constant vertical load V' = 62 N that caused the self weight penetration. To compare these results with other suction records the non dimensional parameters $\frac{s}{\gamma' 2R}$ and $\frac{h}{2R}$ were included in the plots. The suction calculations shown in Figures 4.16(a) and 4.16(b) correspond to: i) linear stress distribution with depth, ii) exponential stress distribution with depth based on soil arching, and iii) other non-linear increase of stresses with depth due to soil arching.

According to these calculation results the three procedures lead to an underestimation of the measured suction. The use of non-linear σ'_v gave a better prediction followed by exponential σ'_v, and linear σ'_v. A large discrepancy of V_o was obtained using the same

Table 4.6: A summary of suction installation tests

Test and caisson	$\frac{ds}{dh}$ kPa/m	$\dot{s}$ kPa/hr	$\dot{h}$ mm/min	t_s min	h_p mm	h_{pe} mm	h_o mm	V_o N
FV1_2_1E†	22	1.3	0.82††	106	25	4	98	217
FV10_4_1D	17	2.8	2.64	42	27	20	138	641
FV3_1_1C†	18	0.8	0.93	73	29	0	97	250
FV9_4_1C	19	$0.17e^{2.825t}$	$0.45e^{0.042t}$	50	13	2	90	414
FV6_5_1C	22	2.6	2.22	25	35	4	92	296
FV9_2_1C	22	2.8	2.29	37	16.5	13	94	443
FV9_1_1C	20	6	5.30	13	29.5	20	96	458
FV9_5_1A	26-10	1.7	$0.26e^{0.027t}$	98	12	0	128	2616
FV10_3_1A	21	1.6	$0.29e^{0.027t}$	97	13	3	119	2146
FV7_3_1A	22	4.6	3.67	30	29	7	131	1724
FV10_2_1A	20	0.6	0.18 - 0.44‡	300	20	4	135	2582
FV7_1_3A	30	8	4.33	22	46	13	123	1571
FV10_1_1A	20	0.8	0.34 - 0.62‡	215	22	8	131	2472

†oil-saturated Baskarp Cyclone sand, ††$\dot{h}$ = -0.63·$10^{-4}t^2$ + 0.15t - 0.38, ‡bi-linear

soil parameters for h_o = 135 mm, resulting in: i) 820 N, ii) 1474 N, and iii) 2582 N. Villalobos *et al.* (2005) report a similar underestimation of the suction when using the stress enhancement calculation procedure iii) for the test FV7_3_1A adopting a very high $K \tan\delta = 0.9$, $f_i = f_o = 1$ and $k_f = 1$ (V_o = 1700 N for h_o = 131 mm).

The initial pushing penetration of the skirt into dense sand rises a soil plug owing to

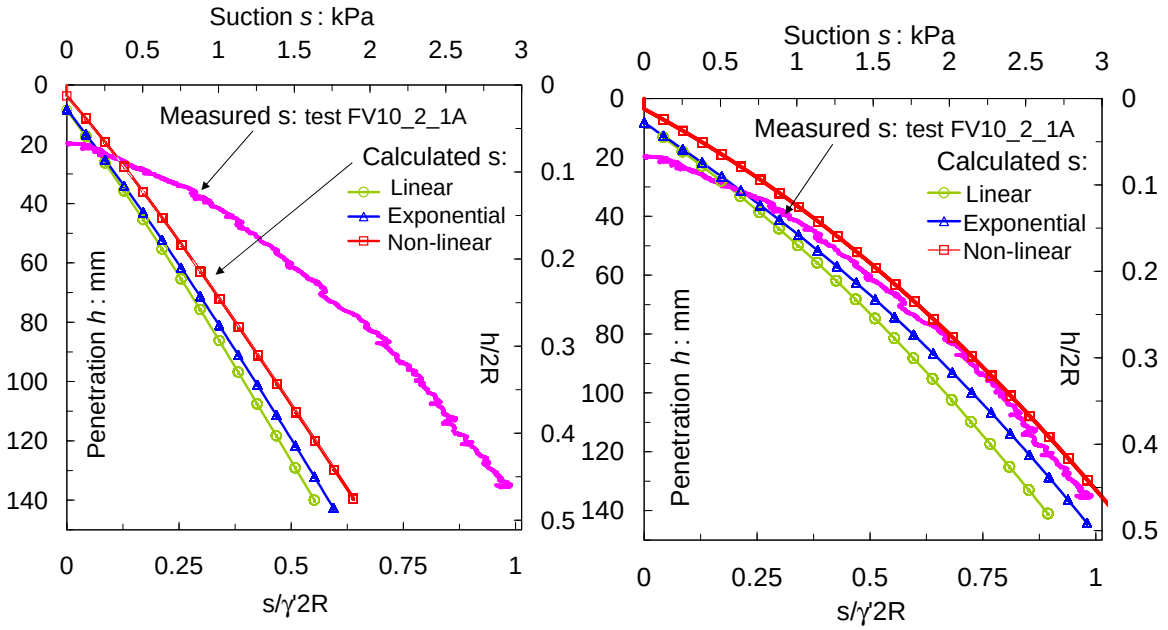

(a) $k_f = 1$ (b) $k_f = 3.4$

Figure 4.16: Measured and calculated suction-penetration curves assuming V' = 62 N, $m = 2$ for exponential, and $f_i = f_o = 1$ for non-linear stress distribution

dilative behaviour as discussed in Chapter 3. As a consequence of sand dilation an increase of specific volume occurs, hence permeability increases too if the sand is saturated according to the Kozeny-Carman equation (4.21). In the light of the experimental results this is confirmed, since the soil permeability changes due to dilation and seepage, which modifies the effective stresses during caisson penetration, and as a consequence the specific volume and in turn the permeability ratio $k_f > 1$. This qualitative experimental evidence is supported quantitatively by the suction calculation and equation (4.21), which relates the increase of permeability with specific volume. Indeed, Figure 4.16(b) shows the significant improvement of the suction estimation when a permeability ratio k_f of 3.4 is chosen. Although the use of linear or exponential distribution of stresses still underestimate the suction compared with the non-linear approach, they can be useful as preliminary estimations or as a verification of numerical results. Furthermore, for piles soil arching effects diminishes as pile diameter increases (Hight *et al.*, 1996; Lehane *et al.*, 2005). Therefore, these simpler calculation procedures may be useful. However, this needs to be investigated for suction caissons.

It was not a surprise that in calculations of the suction the surcharge force B_q was predominant whereas the influence of the weight force B_γ was negligible as in sections §4.3.1 and §4.3.3, since those calculations are based on formulations for pushing penetration. Finally, the variation of soil permeability cannot be overlooked if an accurate estimation of the suction is pursued. In Chapter 3 it was pointed out that the skirt penetration causes a soil plug heave as a result of dilative behaviour in dense sand. In consequence, soil permeability k_i increases next to the skirt wall since dilation induces the increase of void ratio, but k_o decreases due to the opposite direction of seepage.

Calculated distributions of effective vertical stress are shown in Figure 4.17 for test FV10_2_1A. Non-linear distributions of $\sigma'_{v\,o}$ and $\sigma'_{v\,i}$ were calculated as in the case of pushing penetration (see Figure 4.10(b)). The effect of seepage on the stresses is also reflected in Figure 4.17, where the calculated effective vertical stress $\sigma'_{v\,o\,seepage}$ increased whereas $\sigma'_{v\,i\,seepage}$ reduced with depth. Furthermore, the calculated distribution of excess

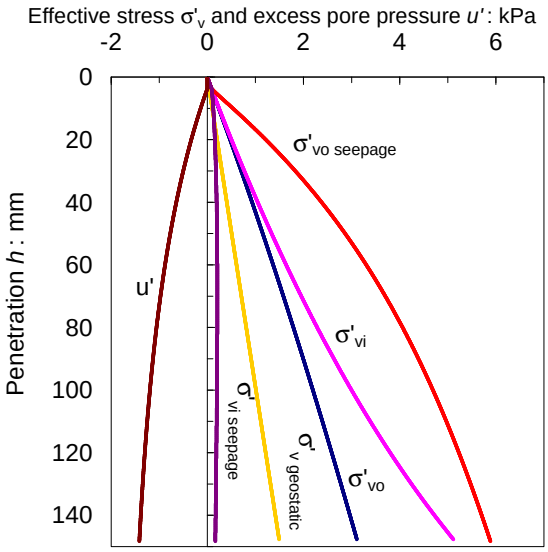

Figure 4.17: Calculated distribution of effective vertical stresses with and without seepage, showing also calculated distribution of excess pore water pressure u' at the tip of the caisson (test FV10_2_1A)

pore water pressure u' at the tip of the caisson as penetration occurs is plotted in Figure 4.17. Because the calculation of u' includes the pressure factor a, the distribution of u' is not linear since a varies non linearly with depth. Note the drastic reduction of $\sigma'_{v\,i}$ to $\sigma'_{v\,i\,seepage}$ explains why installation under low net vertical load is possible.

Measured and calculated suction were compared for three different values of submerged weight V' as shown in Figure 4.18(a) for caisson A and in Figure 4.18(b) for caisson C. The calculated suction reduces when V' is increased, reproducing the same trend observed in the measured suction. Test FV9_2_1C was carried with the caisson tilted 4°. However, the suction did not straight the caisson up during penetration. The use of suction does not rotate or translate the caisson as may occur during pushing penetration. Calculated hydraulic gradients, using equation (4.13), are opposite in direction yet clear differences in magnitude are found as shown in Figures 4.19(a) and 4.19(b). Whilst i_o causes a flow downwards and can be larger than one, i_i causes a flow upwards and has a high initial increase that continues asymptotically. This asymptote corresponds to the critical hydraulic gradient $i_c = \frac{\gamma'}{\gamma_f} = 1.03$, hence $i_i < 1$. A high i_o is beneficial because it strengthens the sand, buffering for instance the spread of an initial piping condition. On the other hand, i_i is also beneficial in the sense that allows the skirt to penetrate under

a much lower vertical load. However, i_i is limited by the critical hydraulic gradient i_c, otherwise piping failure may occur and further penetration may not be possible. It is worth noting that the increase of V' reduces the hydraulic gradient inside the caisson i_i, so reducing the risk of piping failure as well. Figures 4.19(a) and 4.19(b) show that at small penetrations the downward hydraulic gradient i_o is much greater than the upward hydraulic gradient i_i until a maximum value is reached. During subsequent penetration i_o diminishes to values close to i_i at the end of penetration. In the theory this is directly related to the pressure factor a. Experimentally, it was found that initially the suction increases causing small penetration, but once a certain level of suction was reached much larger penetration occurs at a lower (and approximately constant) increase of the suction with penetration. Those approximately constant values of $\frac{ds}{dh}$ are shown in Table 4.6.

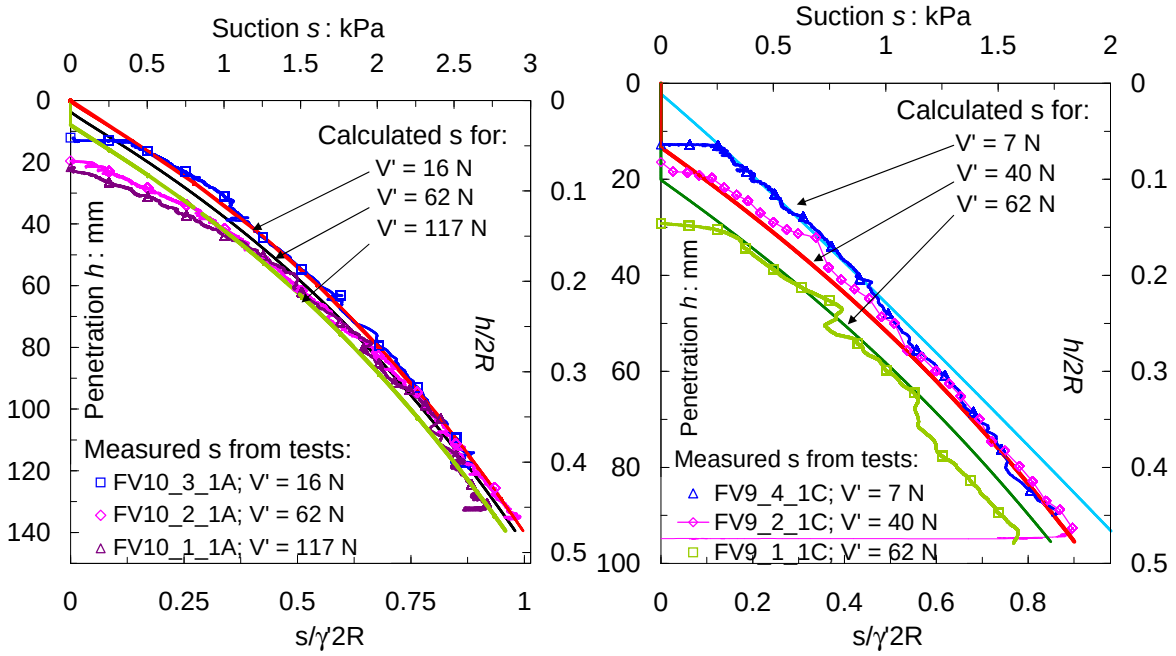

(a) Caisson A (b) Caisson C

Figure 4.18: Measured and calculated suction-penetration curves using non-linear stress distribution and $k_f > 1$

Figure 4.20(a) shows the suction applied to caissons E and D, which differed only in the skirt length L as presented in Chapter 2. Nevertheless, caisson E was installed in a very fine oil-saturated sand under a low vertical load $V' = 5$ N, and caisson D was installed in a fine water-saturated sand under a higher vertical load $V' = 45$ N. Owing to these differences two patterns of suction variation with depth appeared. For the former an

initial high increment of suction occurred, whilst for the latter a lower and relatively constant increment of suction with depth occurred. However, once the initial high increment of suction diminished both curves were almost parallel. For caisson E a higher suction increment was needed in order to start the caisson penetration as a consequence of the

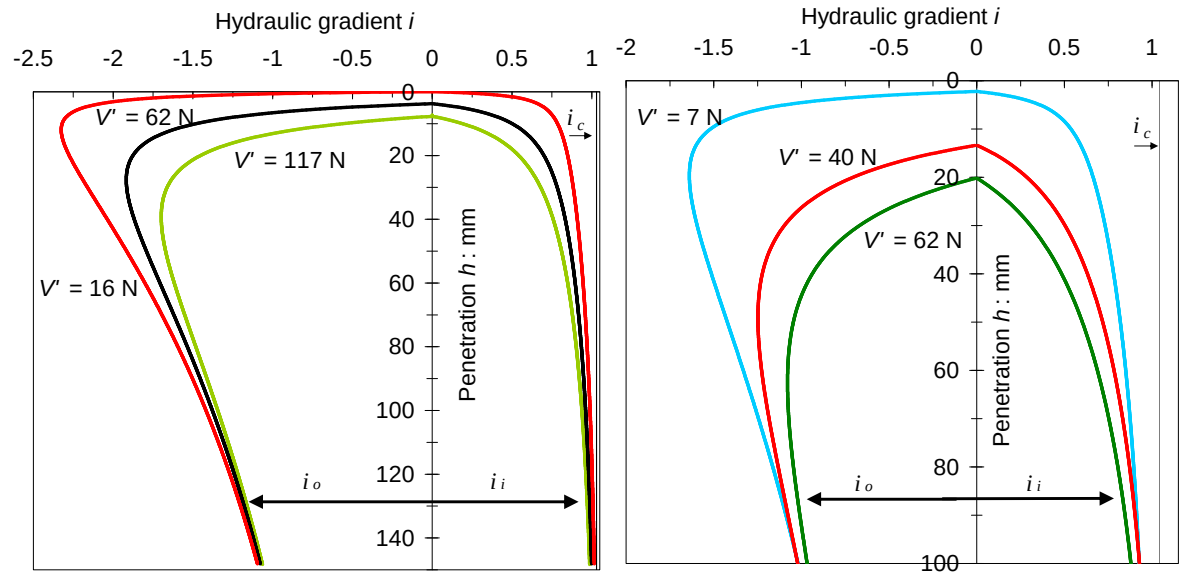

(a) FV10_3_1A, FV10_2_1A, and FV10_1_1A, (b) FV9_4_1C, FV9_2_1C, and FV9_1_1C

Figure 4.19: Calculated average hydraulic gradients, showing critical hydraulic gradient i_c using equation (4.13)

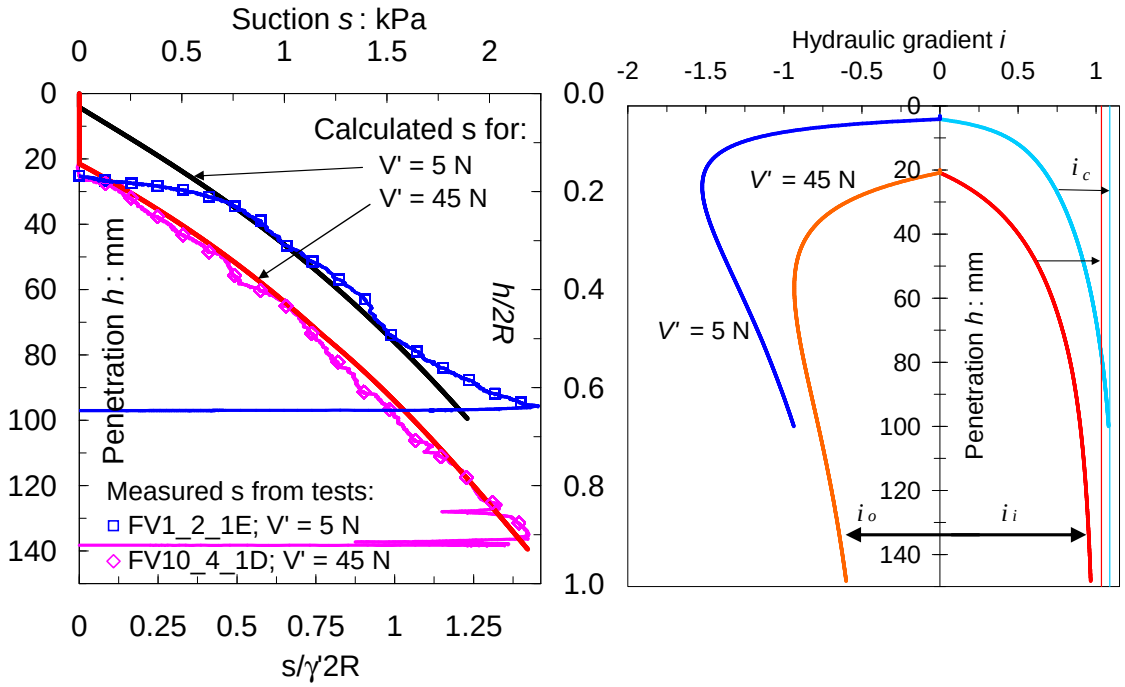

(a) (b)

Figure 4.20: (a) Measured and calculated suction-penetration curves, and (b) calculated hydraulic gradients outside and inside the caisson, showing critical hydraulic gradient i_c

low soil permeability caused by the oil permeant. In other words, to create enough upwards seepage forces to reduce the soil strength. To achieve this an increase of pore fluid pressure was required to cause the reduction of effective stresses at the tip. An equivalent finding by Tran *et al.* (2004) indicates that the suction increases with penetration rate. However, the increase of the suction with the reduction of permeability or with the increase of penetration rate, although consistent, have not been yet explained by theory. Once the flow regime was developed the increment of suction *stabilised*, for that reason both curves end up with similar slopes. This *stabilisation* or steady state flow regime requires more suction for caisson E because it is not only being penetrated under a lower vertical load, but also into a soil with a permeability three orders of magnitude lower than that for caisson D. (In Figures 4.18(a) and 4.18(b) the difference in the measured suction curves was only due to different V', because the sand and the permeant were the same). It can also be observed that the measured suction for caisson E increased at a higher rate after a penetration of 75 mm. This indicates the presence of a much denser sand layer that forces a higher suction to be applied in order to progress. This sample was around three years old and probably for that reason there was this increase of density with depth.

The purpose of the following series of tests was to investigate the caisson installation under very low vertical loads as well as higher penetration rates. Figure 4.21(a) shows that installation by suction was possible even under a tensile load V' of -4 N in oil-saturated Baskarp Cyclone sand (test FV3_1_1C). Installation under negative V' is not relevant to field but it was included for completeness. A second test shown in Figure 4.21(a) corresponds to the installation in water-saturated Redhill sand under a low load V' of 7 N (test FV6_5_1C). Contrary to Figure 4.20(a), where both measured curves were distant, in Figure 4.21(a) both measured curves are almost similar once suction stabilisation was reached. Because the values of V' were similarly low, there was a compensation between the differences in soil permeabilities and the suction rate $\dot{s}$. Not surprisingly, for the less permeable soil $\dot{s}$ and $\dot{h}$ were lower than for the more permeable soil (Table 4.6). This was also reflected in the time needed to install the caisson, three times more for the less permeable soil.

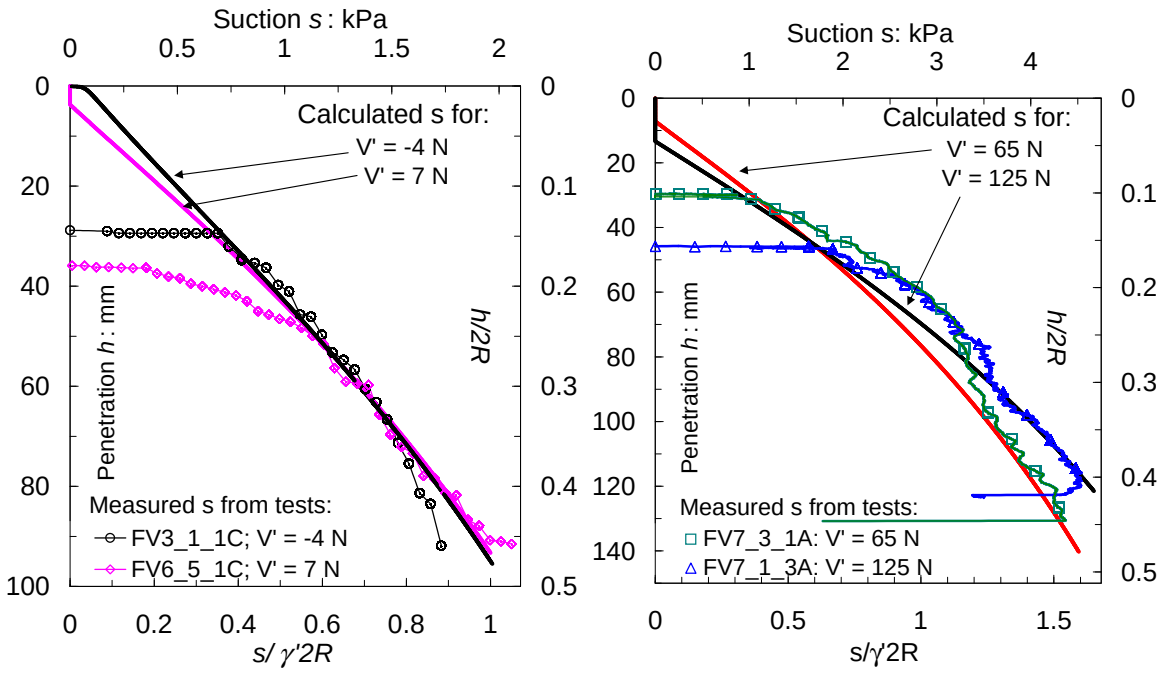

(a) FV3_1_1C, FV6_5_1C (b) Caisson A

Figure 4.21: Measured and calculated suction-penetration curves for higher penetration rates

An almost twofold increase of the applied suction can be observed in Figure 4.21(b) when comparing with similar tests shown in Figure 4.18(a). The comparison is also valid with other tests in terms of $\frac{s}{\gamma' 2R}$, usually less than one, now reaches a maximum value of 1.6. For example, tests FV7_3_1A and FV10_2_1A have relatively similar V' and R_d (65 N, 74%, and 62 N, 89%), but for the doubled suction applied an increase of ten times the rate of penetration $\dot{h}$ was obtained. The same occurred comparing tests FV7_1_3A and FV10_1_1A. Furthermore, when the suction was doubled an increase of twenty times the penetration rate was found in tests carried out by Tran *et al.* (2004) in water-saturated silica sand ($2R = L = 100$ mm, $t = 0.5$ mm, $V' = 2.6$ N and $R_d = 92\%$). Therefore, the suction increment causes penetration rate effects. The underestimation of suction in the test FV7_3_1A by Villalobos *et al.* (2005) reveals that in part it was due to rate effects because the calculated suction in Figure 4.21(b) used a k_f value of 8 (Table 4.6). It is assumed that expressions (4.20) and (4.22) hold despite the fact that the pore pressure factor a parameters was estimated for a range of k_f between 1 and 5. The model does not consider rate effects and a high value of k_f results as an attempt to fit the data. Further work is needed to include rate effects in the calculations. Figure 4.22(a) shows that higher suction rate increases substantially the outside hydraulic gradient i_o and Figure 4.22(b)

shows that this results in high stresses outside the caisson.

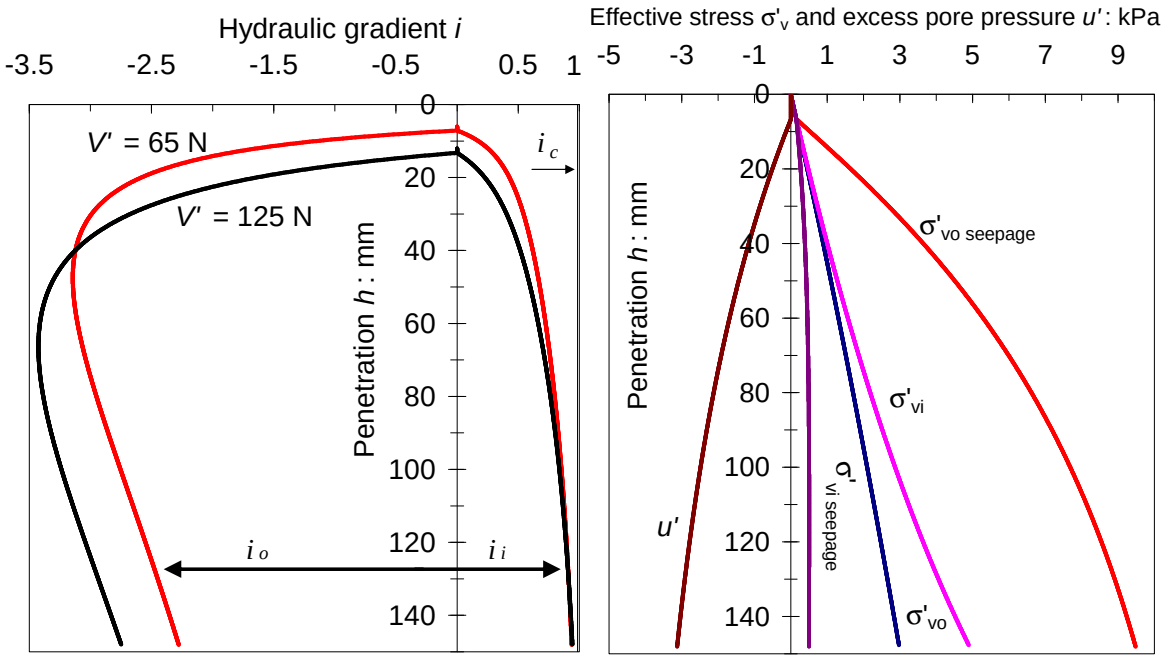

(a) Tests FV7_3_1A and FV7_1_3A (b) FV7_3_1A

Figure 4.22: (a) Calculated hydraulic gradients, and (b) calculated effective vertical stresses and excess pore water pressures at the caisson tip

Limits to suction installation were determined using the expressions from section §4.2.4. Hydraulic gradients have already been shown in Figures 4.19(a), 4.19(b), 4.20(b) and 4.22(a) and compared against the critical hydraulic gradient i_c. Table 4.7 coalesces three criteria to evaluate the limit to the applied suction: i) hydraulic gradient $i_i < i_c$, ii) the safety factor to inverse bearing capacity failure $\frac{\sigma'_{v\,i} N_q}{\sigma'_{v\,o}} < 1$, and iii) penetration $h_{crit} > L$. Only in test FV7_3_1A a local piping occurred at a penetration of 43 mm, however, after reapplying the suction the test continued without further interruption. In general, around the outside of the caisson a settlement of the sand in the form of a wedge occurred as a result of densification or rearrangement of fine particles. This was particularly visible in test FV10_4_1D. Therefore, criteria i) and ii) were in agreement with the experimental results. In criterion iii) equation (4.28) overestimates the critical penetration, whereas equation (4.31) underestimates the critical penetration.

A comparison between two tests with the same caisson and sand conditions, but installed by pushing and by suction is shown in Figure 4.23. For the suction installation test the

Table 4.7: Limits to suction installation

Test and caisson	i_c	$i_{i\,max}$	$\frac{\sigma'_{v\,i} N_q}{\sigma'_{v\,o}}$	h_{crit} (4.28) mm	h_{crit} (4.31) mm
FV1_2_1E†	1.09	1.07	1	135	64
FV10_4_1D	1.03	0.96	19	211	130
FV3_1_1C†	1.09	1.03	4	157	70
FV9_4_1C	1.04	0.99	7	173	83
FV6_5_1C	0.99	0.93	5	173	84
FV9_2_1C	1.04	0.91	17	209	118
FV9_1_1C	1.04	0.87	24	229	138
FV9_5_1A	1.04	1.02	2	242	113
FV10_3_1A	1.03	1.00	4	250	115
FV7_3_1A	0.99	0.94	2	259	129
FV10_2_1A	1.03	0.99	5	292	141
FV7_1_3A	0.99	0.90	4	272	144
FV10_1_1A	1.03	0.99	5	331	167

vertical load V' was kept constant at 60 N, and the curve labelled $V'+S$ represents the net vertical load due to the constant 60 N plus the pressure differential on the caisson lid in terms of force. It is clear that there is a significant reduction of the net vertical load using suction, reflected in the difference between the suction curve and the pushing curve. That difference between these curves represents the beneficial effects of the hydraulic gradients set up within the soil due to the suction.

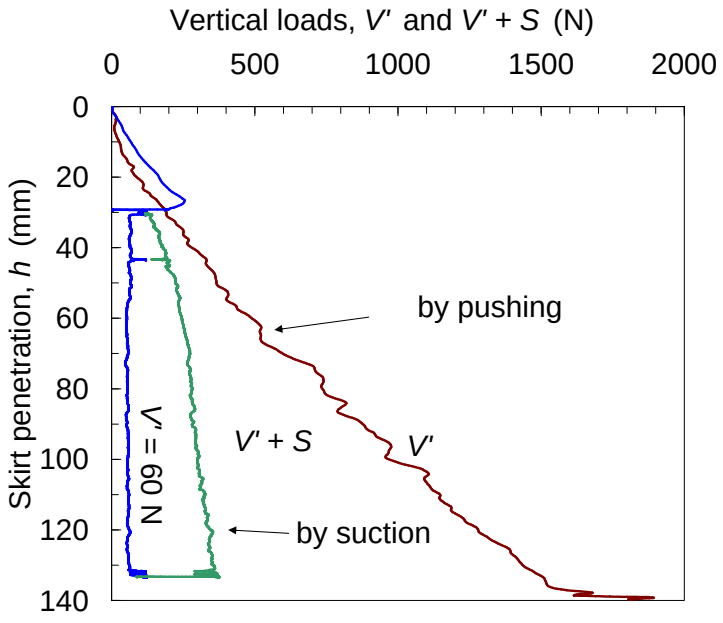

Figure 4.23: Comparison between pushed installation and suction installation for the 293 mm diameter caisson

4.4 CONCLUSIONS

From the experimental and analytical work carried out to study the installation of caissons by pushing and by suction the following conclusions can be drawn.

An expression to evaluate the lateral earth pressure against a frictional wall (not smooth) is suggested. Interface friction angles were correlated by means of the wall maximum roughness. In this way the parameter $K \tan \delta$ could be evaluated and not back calculated.

The pushing installation method was used to simulate a condition of self-weight penetration. In the field extremely large self-weights would be normally necessary to install fully a prototype caisson. The use of suction can supply the vertical load over the self weight available to completely install a caisson. With the assistance of suction there is a considerable reduction in the net force required to penetrate a caisson into dense sands due to the hydraulic gradients created by the application of suction. Pushing installation was extensively used in the laboratory owing to simplicity, especially when subsequent monotonic or cyclic loading tests were planned. These results were extremely useful for the parameter calibration and general assessment of the installation theory. It was found that for the thickness ratios and aspect ratios used the surcharge force was the most relevant followed by the friction forces in terms of the calculation of the vertical load and the suction. The end bearing component is practically negligible.

Caisson verticality must be carefully controlled during pushing penetration. Tests results demonstrated that a caisson can increasingly tilt with depth if the resultant vertical force is not centred. When suction was applied, the caisson penetration was straight and no tilting or translation was observed in the vertical plane measured. However, if the caisson is tilted the suction application can not straighten it up.

Under similar conditions, less suction was required when the submerged self weight increased. In addition, not only the caisson self weight, but also the permeability influences

the suction which generates seepage. It was found that the permeability ratio was a very decisive parameter in the determination of the suction. A range of values between 2 and 3 were previously suggested by Houlsby and Byrne (2005b), but in this study a wider range was necessary to predict appropriately the experimental results. In tests with high penetration rates as a result of high suction rates values of the permeability ratio between 8 and 10 were used to estimate the measured suction. Therefore, there is a rate effect that needs to be accounted for to calculate the required suction in the case of applied suction rates which are of one order of magnitude higher in conjunction with low values of V'. More research is needed to study the interaction between suction rate and penetration rate.

A study of the critical suction or critical penetration must be done to assess the adequacy of the caisson design. It was found that the maximum hydraulic gradient i_i compared with the critical hydraulic gradient i_c and the safety factor to the inverted bearing capacity are useful options to evaluate the limits to the suction. Critical penetration was overestimated when calculated with linear stress distribution, whereas the critical penetration was underestimated when non-linear stress distribution was adopted.

Chapter 5

MOMENT LOADING CAPACITY OF CAISSONS IN DRY SAND

Abstract

This chapter presents and analyses experimental results obtained from combined loading tests on model scale caissons. Combined moment and horizontal loading tests conducted with low constant vertical load are covered broadly to explore the shape and size of the caisson yield surface and the corresponding vectors of incremental plastic displacements. A major purpose of this investigation was to provide the information necessary to construct hyperplasticity formulations within the framework of force resultant models. It has been found that caissons can resist moment and horizontal loads under tension. The experimental results indicate that a yield surface and a flow rule formulation derived from hyperplasticity theory can be applied to modelling the results described here.

5.1 A SIMPLE MODEL

A simple model based on force equilibrium is a useful way of giving insight and understanding in soil-footing interaction problems. Figure 5.1 depicts the external forces applied to a caisson at the load reference point LRP as well as the reacting internal stresses and lateral earth pressures. It is assumed that the enclosed soil plug moves with

the caisson and as a result does not interact with the caisson. Then, the shear stresses represent the external friction between the caisson and the soil next to the wall and across the base. End bearing stresses around the caisson rim are included in the total vertical stresses σ'_v at the base. Assuming that σ'_v is uniformly distributed as a consequence of the soil plug weight and V' is a simplification. Because it may be arguable that a triangular distribution would appear when large moments are transmitted to the tip level overlapping the stresses due to soil plug weight and V'. In that case σ'_v should be considered as an average value. It is also assumed that the caisson rotates without lateral displacement around a point exactly under the LRP at a distance z_m. This point of rotation is referred to as the *metacentre*.

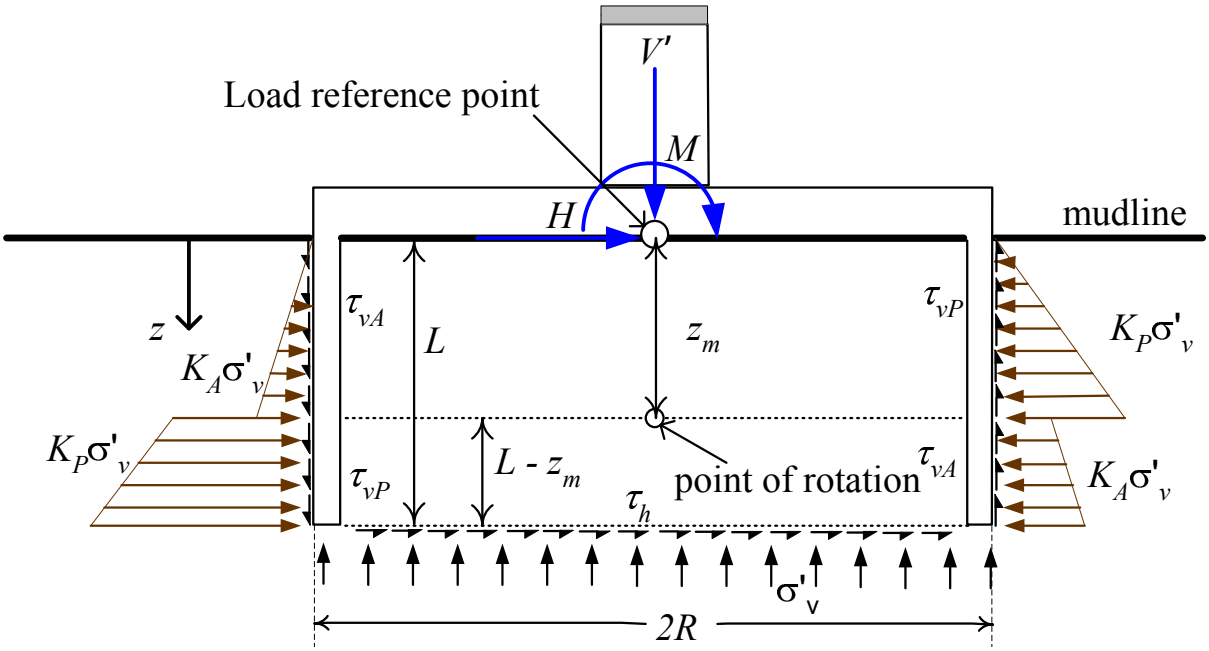

Figure 5.1: Simplified model of soil-footing interaction mechanism for a caisson with an aspect ratio of $\frac{L}{2R} = 0.5$ under a planar system of combined loading

The inclusion of the vertical load V' extends the analysis carried out by Byrne (2000) using M and H. The equations of force equilibrium that include the applied loading system (V', M, H) and the reaction forces due to friction and earth lateral pressure can be expressed as follows:

$$V' = \sigma'_v \pi R^2 + F_v \quad \text{with} \quad F_v = 2R\gamma' L \tan\delta K(2z_m - L) \tag{5.1}$$

$$H = 2R\gamma' K\left(z_m^2 - \frac{L^2}{2}\right) - F_h \quad \text{with} \quad F_h = \tau_h \pi R^2 = \sigma'_v \tan\phi' \pi R^2 \tag{5.2}$$

$$M = \frac{2R\gamma' K}{3}(L^3 - 2z_m^3) + F_h L + f(F_v)R \quad \text{with} \quad f(F_v) = \frac{(K_A + K_P)[(L - z_m)^2 + z_m^2]}{LK(2z_m - L)}F_v \tag{5.3}$$

At the base σ'_v includes the geostatic pressure of the soil plug and stresses transmitted by the vertical load V', F_v is the resultant of vertical frictional forces along the skirt, K is the difference between the passive and active lateral earth pressure coefficients $K = K_P - K_A$, F_h is the resultant of horizontal frictional forces caused by the shear stresses at the base, where ϕ' is the soil-soil interface angle of friction. It is assumed that the resultant lateral earth pressures (and shear stresses) act along the skirt over a perimeter equal to the diameter of the caisson $2R$. From equation (5.2) the horizontal load is proportional to the square of the caisson skirt length, whereas from equation (5.3) the moment is proportional to the cube of the caisson skirt length. If frictional forces on the skirt are neglected and

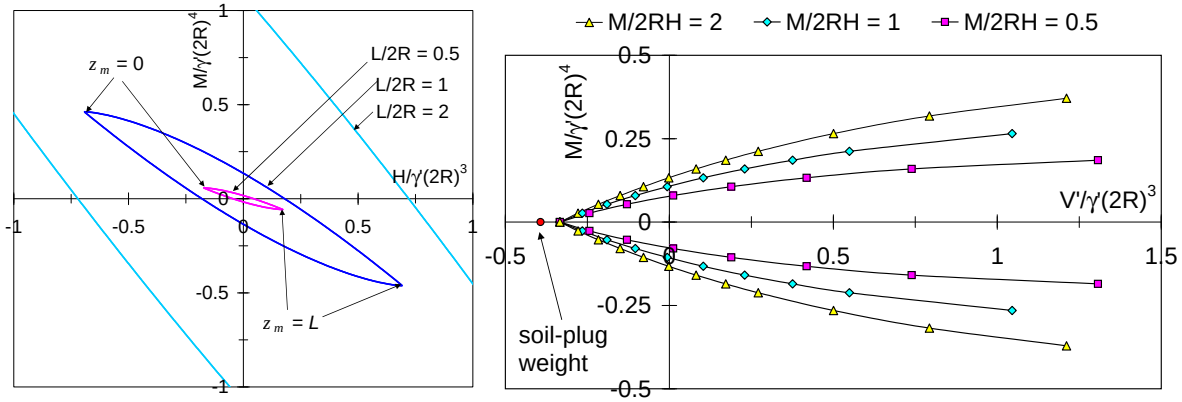

(a) $F_v = F_h = 0$ N (b) $\frac{L}{2R} = 0.5$

Figure 5.2: (a) Load envelopes in the normalised moment and horizontal load plane for three caisson aspect ratios $\frac{L}{2R}$, and (b) load envelopes in the normalised moment and vertical load plane for three load ratios $\frac{M}{2RH}$

equations (5.2) and (5.3) are merged z_m can be eliminated to obtain a load envelope, also referred to as interaction diagram, in which a state of loading on the envelope corresponds to a condition of limit equilibrium; outside the envelope static equilibrium is not possible. This load envelope can be expressed by:

$$\left[\frac{1}{2} - \frac{3(M - F_h L - f(F_v)2R)}{4R\gamma' K L^3}\right]^2 - \left[\frac{H + F_h}{2R\gamma' K L^2} + \frac{1}{2}\right]^3 = 0 \tag{5.4}$$

Three load envelopes were calculated using equation (5.4) and plotted in a normalised moment and horizontal load plane as shown in Figure 5.2(a). All the frictional forces have been neglected, so that the caisson response is independent of the vertical load V' and equation (5.4) holds for any value of V'. As a result of that an enormous increase in lateral load and moment load resistance with the caisson aspect ratio $\frac{L}{2R}$ is observed. Figure 5.2(a) illustrates that as the metacentre moves along the centre of the caisson from $z_m = 0$ to the bottom where $z_m = L$, similarly z_m moves from top to bottom of the load envelope. To include the effect of V' on the caisson resistance frictional forces were included in the calculations. The weight of the soil plug and V' are implicit in the calculation of σ'_v in F_h. Figure 5.2(b) shows the increase of the normalised moment load with the normalised vertical load. Therefore, the increase of V' triggers frictional forces that have a beneficial effect on the caisson moment resistance.

5.2 THEORETICAL FRAMEWORK

From the simple model presented above more sophisticated models can be constructed, assuming failure mechanisms plasticity models can be developed. A different approach recently taken is to derive constitutive models from thermodynamics. This approach is referred as hyperplasticity. In hyperplasticity the elements of the constitutive model arise from the thermodynamic laws instead of adding *ad hoc* elements to construct a model.

The present study is intended to provide experimental information to construct hyperplasticity models by means of determining for instance the yield surface and a flow rule. In order to obtain practical results hyperplastic models necessitate accurate values of the model parameters. Thus the determination of these parameters from laboratory tests was an important objective of this investigation. The advance in theoretical modelling necessitates of advances in physical modelling as well to make possible that a mathematical theory has useful applications in geotechnical engineering.

5.2.1 Elasticity

In hyperplasticity theory the elastic behaviour occurs inside and on the yield surface as assumed traditionally in plasticity. An elastic load-displacement relationship can be presented in a displacement controlled form as follows:

$$\begin{Bmatrix} V' \\ M \\ H \end{Bmatrix} = \begin{Bmatrix} K_V & 0 & 0 \\ 0 & K_M & K_{MH} \\ 0 & K_{MH} & K_H \end{Bmatrix} \begin{Bmatrix} w \\ \theta \\ u \end{Bmatrix} \tag{5.5}$$

where K_V, K_M, K_H and K_{MH} are the stiffness coefficients given by:

$$\begin{aligned} K_V &= 2GRk_v; \quad K_M = GR^3k_m - 8GR^2dk_{mh} + 2GRd^2k_h; \\ K_H &= 2GRk_h; \quad K_{MH} = 4GR^2k_{mh} - 2GRdk_h \end{aligned} \tag{5.6}$$

R is the footing radius, d is the distance between the assumed LRP and the point where the combined loads are applied as pointed out in Chapter 2 (d is zero if the loads are applied on the LRP); w, θ and u are the elastic vertical, rotational and horizontal displacements. If the LRP is located at the elastic metacentre, the matrix in (5.5) becomes diagonal ($K_{MH} = 0$) and coupling of moment and horizontal load does not occur (Bell, 1991; Houlsby, 2003). This is because the moment applied in the elastic metacentre causes pure elastic rotation of the caisson and *vice versa* the elastic horizontal load applied at the elastic metacentre causes only translation of the caisson. Numerical analyses carried out recently by Doherty and Deeks (2003) provide the dimensionless stiffness coefficients k_v, k_m, k_h and k_{mh} for assessing the elastic behaviour of skirted footings at different embedments. A Poisson' ratio of 0.2 was assumed, which is appropriate for a wide range of sands. Moreover, four caisson aspect ratios were considered, $\frac{L}{2R} = 0.25$, 0.5, 1 and 2. Additionally, an α parameter that accounts for the type of shear modulus G distribution with depth as well as a rigid caisson were considered. Latterly, Doherty *et al.* (2005) extend the analysis to the case of flexible caissons, which can introduce significant reduction of the stiffness coefficients for low caisson thickness ratios $\frac{t}{2R}$ and even more if the soil is very stiff. Assuming a constant shear modulus G, the elastic displacement components

for the planar case can be derived as follows:

$$\begin{Bmatrix} w \\ \theta \\ u \end{Bmatrix} = \begin{Bmatrix} \frac{1}{K_V} & 0 & 0 \\ 0 & \frac{K_H}{D} & -\frac{K_{MH}}{D} \\ 0 & -\frac{K_{MH}}{D} & \frac{K_M}{D} \end{Bmatrix} \begin{Bmatrix} V' \\ M \\ H \end{Bmatrix} \tag{5.7}$$

where

$$D = K_M K_H - K_{MH}^2 \tag{5.8}$$

From the elastic stress wave propagation problem it is well known that the elastic shear modulus is related to the shear wave velocity v_s and the density ρ of the medium of propagation by $G = \rho v_s^2$. Measurements of shear wave velocities in sand (Hardin and Richart, 1963; Ishihara, 1993) have demonstrated that even under small strain amplitudes G has a non-linear dependency on the current level of stresses. Moreover, G was found to be a function of the specific volume υ and grain angularity. These findings have led to the use of the following general expression of G assuming isotropic stress conditions (Schnaid, 1990; Houlsby *et al.*, 2005; Mitchell and Soga, 2005; Kelly *et al.* 2006):

$$\frac{G}{p_a} = A f(\upsilon) \left(\frac{\sigma'_v}{p_a} \right)^n \tag{5.9}$$

where σ'_v is a representative effective stress that represents the current stress level, p_a is the atmospheric pressure adopted as a reference stress, n and A are constants that can be related to grain angularity and $f(\upsilon)$ is a function of the specific volume υ. Kelly *et al.* (2006) assume a mean effective stress as the effective vertical stress at a depth aR below the caisson as:

$$\sigma'_v = \frac{V'}{\pi R^2} + \gamma'(L + aR) \tag{5.10}$$

Equation (5.9) was used by Houlsby *et al.* (2005) in the derivation of a hyperelastic formulation. It was found that a pressure exponent $n = 0.5$ gives a good representation of shear strain contours when compared with experimental results. Values of the constant A and expressions of the function $f(\upsilon)$ for different soils can be found in Mitchell and Soga (2005).

5.2.2 Yield surface

Changes in the loading of a footing can cause the surrounding soil to yield. The combination of these loadings can be used to define a yield surface if plastic irreversible displacements of the footing occur. Mathematically, yield is expressed by means of yield surfaces. Yield surface formulations for flat footings date from the works by Butterfield and Ticof (1979) and Butterfield and Gottardi (1994). Subsequently, yield functions were proposed by Martin (1994) to construct Model B as well as Gottardi *et al.* (1999) and Cassidy (1999) to construct Model C.

Recently, an expression of the yield surface for caisson footings has been proposed by Nguyen-Sy and Houlsby (2005). This new formulation differs from the yield function used by Cassidy (1999) since it includes the possibility for tensile vertical loads. The yield function can be expressed in a reduced form as follows:

$$y = t^2 - \beta_{12}^2 \left(\nu_1 + t_o\right)^{2\beta_1} \left(1 - \nu_2\right)^{2\beta_2} = 0 \tag{5.11}$$

The horizontal and moment loads are expressed through t in the form of an eccentric ellipse, where for the planar case t is given by:

$$t = \sqrt{h^2 + m^2 - 2emh} \tag{5.12}$$

where e is the eccentricity of the ellipse. Considering the isotropic hardening case the dimensionless horizontal and moment loads are given by the following expressions:

$$h = \frac{a_H \chi_H + (1 - a_H) H}{h_o V_o} \qquad m = \frac{a_M \chi_M + (1 - a_M) M}{2 R m_o V_o} \tag{5.13}$$

The dimensionless vertical loads ν_1 and ν_2 are given by:

$$\nu_1 = \frac{a_{V_1} \chi_V + (1 - a_{V_1}) V'}{V_o} \qquad \nu_2 = \frac{a_{V_2} \chi_V + (1 - a_{V_2}) V'}{V_o} \tag{5.14}$$

χ_V, χ_M and χ_H are the dissipative generalised vertical, moment and horizontal loads, which are related to the dissipation function d by means of the partial derivative $\chi_i = \frac{\partial d}{\partial \dot{\alpha}_i}$, where α_i are internal variables that represent irreversible behaviour and play the role of plastic displacements under certain conditions (Collins and Houlsby, 1997). It is worth mentioning that in kinematic hardening models for instance, $\sigma_{ij} - \chi_{ij}$ plays the role of a 'back stress', where the kinematics comes from the definition established with the internal variable α_{ij} for the generalised stress $\overline{\chi}_{ij}$ (Puzrin and Houlsby, 2001). On the other hand, σ_{ij} represents the true loads V', M and H, and a_{V_1}, a_{V_2}, a_M and a_H are "association factors". However, depending on their values they are able to describe non-associativity as well. a_{V_1} and β_1 deal with low vertical loads, whereas a_{V_2} and β_2 deal with the higher V values. The yield surface maximum dimension is defined by α (in a dimensionless $m-\nu$ or $h-\nu$ plane or at $V' = \alpha V_o$ in a $M - V'$ plane):

$$\alpha = \frac{\beta_1 - \beta_2 t_o}{\beta_1 + \beta_2} \tag{5.15}$$

Furthermore, according to equations (5.11) and (5.12) at the point α the intersection of the yield surface with the m and h axes are simultaneously maximums. These maximum intersection points are referred to as m_o and h_o. The tension parameter t_o is defined by:

$$t_o = \frac{|V_{t\,max}|}{V_o} \tag{5.16}$$

where $V_{t\,max}$ is the load of maximum tension or also referred to as the pullout capacity. V_o represents a pre-consolidation load, commonly the largest load experienced by the caisson during installation. Both loads $(V_{t\,max}, V_o)$ correspond to the cases of pure vertical load and they define the size of the yield surface. The parameter β_{12} is given by:

$$\beta_{12} = \beta_1^{-\beta_1} \beta_2^{-\beta_2} \left(\frac{\beta_1 + \beta_2}{t_o + 1} \right)^{\beta_1 + \beta_2} \tag{5.17}$$

5.2.3 Flow rule

In hyperplasticity theory the dissipation function gives origin to the yield function and the flow rule (Collins and Houlsby, 1997). Therefore, there is no need to define a plastic potential function. This is a significant difference with the work hardening plasticity theory implemented for instance in Model B and Model C. The flow rule defines the direction of the irreversible displacement increments. The traditional division between elastic and plastic as reversible and irreversible is not necessarily true because of the dependency of stiffness on the internal variable in coupled materials. However, an associated flow rule in generalised load space holds always and plastic displacement increments are obtained according to:

$$\dot{\alpha}_i = \lambda \frac{\partial y}{\partial \chi_i} \tag{5.18}$$

where λ is a positive scalar multiplier that accounts for the magnitude of the velocity vectors. The α_i components are known generically as internal state variables and are related with irreversible processes, for this reason they are related with χ_i by means of the dissipation function.

The non-associated flow rule can be expressed in hyperplasticity as:

$$\begin{Bmatrix} \dot{\alpha}_V \\ \dot{\alpha}_M \\ \dot{\alpha}_H \end{Bmatrix} = \lambda \begin{Bmatrix} \frac{\partial y}{\partial \chi_V} \\ \frac{\partial y}{\partial \chi_M} \\ \frac{\partial y}{\partial \chi_H} \end{Bmatrix} \tag{5.19}$$

Once the derivatives are obtained in true load space the internal variable increments have the following expressions:

$$\dot{\alpha}_V = \lambda \frac{\partial y}{\partial \chi_V} = \lambda \frac{2\beta_{12}^2}{V_o} \left(\nu_1 + t_o\right)^{2\beta_1} \left(1 - \nu_2\right)^{2\beta_2} \left\{ \frac{\beta_2 a_{V_2}}{1 - \nu_2} - \frac{\beta_1 a_{V_1}}{\nu_1 + t_o} \right\} \tag{5.20}$$

$$\dot{\alpha}_M = \lambda \frac{\partial y}{\partial \chi_M} = \lambda \frac{2a_M}{2Rm_o V_o}(m - eh) \tag{5.21}$$

$$\dot{\alpha}_H = \lambda \frac{\partial y}{\partial \chi_H} = \lambda \frac{2a_H}{h_o V_o}(h - em) \tag{5.22}$$

Cassidy (1999) proposes the use of a deviatoric load $Q = V_o t$ to derive a radial displacement increment $\dot{q}$, that is for the consideration of the combined effect of the moment and horizontal load as well as the rotational and translational displacements, which in the incremental form results:

$$\dot{\alpha}_Q = \lambda \frac{\partial y}{\partial \chi_Q} = \frac{\lambda 2Q}{V_o^2} = \frac{\lambda}{\sqrt{1-e^2}} \sqrt{(h_o \dot{\alpha}_H)^2 + (m_o \dot{\alpha}_M)^2 + 2e(h_o \dot{\alpha}_H)(m_o \dot{\alpha}_M)} \qquad (5.23)$$

The use of radial displacements can allow a more direct study of the flow rule, for instance comparing plastic vertical displacement increments with plastic radial displacement increments instead of separately with plastic rotational or plastic horizontal displacement increments.

5.3 EXPERIMENTAL RESULTS

5.3.1 Experimental procedures

The data was recorded as voltages and transformation to engineering units was carried out using relationships obtained from calibration of the instruments. The transformation was automatically implemented in the Visual Basic control program. Subsequently, the displacement raw data in engineering units - directly obtained from the tests, was corrected for the flexibility of the apparatus according to the rig flexibility matrix presented in Chapter 2. Next, loads and displacements were referred to the caisson LRP, which for both caissons tested was 10 mm below the base plate of the rig arm. Displacements w, $2R\theta$ and u were zeroed at the beginning of rotation or translation tests.

Tests were displacement controlled, the installation was done by pushing the caisson into the ground at a constant rate of $\dot{w} = 0.5$ mm/s until the underside of the lid made complete contact with the soil. Once installed, a constant rotational rate of $2R\dot{\theta} = 0.005$ mm/s or 0.01 mm/s was applied to the caisson (see Tables 5.1 and 5.3). For translational tests a constant horizontal velocity of $\dot{u} = 0.01$ mm/s was applied. In both cases a feedback control subroutine allowed for V' and $\frac{M}{2RH}$ to be kept constant during rotational or

translational tests. The reader should refer to Chapter 2 for details of the apparatus and its control, caisson dimensions and soil used as well as Chapter 4 for information of the installation tests carried out before the caissons were subjected to the combined loading tests.

5.3.2 Constant vertical load tests

To map out a yield surface in force space $(V', \frac{M}{2R}, H)$ and to determine the corresponding displacements $(w, 2R\theta, u)$ a series of combined loading tests under low vertical loads were performed. Information on each test is given in Tables 5.1 and 5.2 for caisson A and in Table 5.3 for caisson B. Plotted load-displacement and displacement-displacement curves from test FV1_1_1A to test FV65_11_1A are contained in Villalobos *et al.* (2003b).

Examples of test results using caisson A under a vertical load $V' = 0$ N, but different loading ratios are plotted in Figures 5.3(a), (b), (c) and (d). From plots (a) and (b) yield points were determined and from plots (c) and (d) velocity vectors were determined. The meaning as well as the methods to determine yield points and flow vectors will be explained in section §5.4.

It is possible to see a clear pattern in the curves shown in Figures 5.3(a) and 5.3(b). Initially, the curves are steep (steeper in the $H - u$ curve) which could be seen as linear within a very reduced range of displacement $2R\theta$ (0, 0.2) mm and u (0, 0.05) mm. The load-displacement response progresses after this narrow range of displacement reducing drastically the initial slope until a second 'almost' linear response is reached at a much wider range of displacements $2R\theta$ (0.8, 1.7) mm and u (0.3, 0.8) mm. Broadly speaking, the entire response can be interpreted as an initial stiff response predominantly elastic and a final much softer response where plastic displacements occur. There is evidently a transition response in between. It is clear from Figure 5.3(c) that the loading ratio $\frac{M}{2RH}$ does not affect the displacement curves $u - 2R\theta$. The same observation is not totally true for the displacement curves $w - 2R\theta$ shown in Figure 5.3(d), since the test FV26_3_1

Table 5.1: Summary of the tests undertaken using caisson A

Test	V' N	$\frac{M}{2RH}$	$K_{m\,i}$ $\frac{N}{mm}$	$K_{h\,i}$ $\frac{N}{mm}$	$\frac{M_y}{2R}$ N	H_y N	$2R\theta_y$ mm	u_y mm	$K_{m\,f}$ $\frac{N}{mm}$	$K_{h\,f}$ $\frac{N}{mm}$	$\frac{\delta u^p}{2R\delta\theta^p}$	$\frac{\delta w^p}{2R\delta\theta^p}$
FV130_24_2	-48	0.30	42	181	5.6	18.2	0.51	0.29	2	15	0.44	-1.21
FV84_14_2	-29	0.28	198	460	11.9	40.3	0.35	0.26	3	20	0.51	-0.55
FV85_15_2	4	0.28	283	597	19.1	64.8	0.50	0.35	2	16	0.52	-0.54
FV86_16_1	2	0.29	102	581	14.3	48.6	0.57	0.35	2	10	0.53	-0.50
FV87_16_1	23	0.28	142	631	18.2	60.4	0.60	0.32	2	13	0.51	-0.45
FV88_16_2	51	0.28	306	745	23.6	78.7	0.63	0.52	2	12	0.53	-0.40
FV89_16_1	100	0.28	756	1326	29.0	94.4	0.56	0.48	2	13	0.57	-0.27
FV82_14_2	-29	0.54	235	1088	16.4	29.6	0.45	0.20	4	16	0.46	-0.53
FV26_3_2†	0	0.53	40	534	18.4	33.6	0.60	0.25	4	15	0.46	-0.57
FV35_5_2†	20	0.53	40	350	25.6	45.1	0.78	0.31	3	13	0.49	-0.44
FV34_5_2†	52	0.54	82	680	33.1	58.4	0.81	0.30	3	13	0.49	-0.39
FV33_4_1	101	0.54	204	774	38.8	73.4	0.60	0.34	3	11	0.49	-0.24
FV30_4_2†	99	0.53	151	1269	43.3	75.6	0.69	0.26	4	18	0.50	-0.32
FV99_19_3	-54	1.03	34	50	6.1	6.1	0.54	0.21	3	6	0.41	-0.60
FV60_10_2	-39	1.03	63	109	11.9	10.9	0.29	0.10	10	22	0.44	-0.51
FV61_10_2	-28	1.04	215	246	18.3	17.6	0.47	0.19	5	12	0.40	-0.49
FV27_3_2†	1	1.05	56	298	25.2	23.1	0.74	0.25	4	9	0.44	-0.44
FV57_10_2	21	1.05	218	266	32.5	30.1	0.37	0.18	10	25	0.45	-0.41
FV1_1_2†	51	1.04	628	287	39.1	37.4	0.56	0.30	4	10	0.44	-0.28
FV31_4_2†	103	1.04	166	461	51.9	48.8	0.64	0.32	5	12	0.47	-0.25
FV81_14_2	-29	2.02	122	73	22.0	10.8	0.54	0.25	6	8	0.42	-0.48
FV15_2_2†	-1	2.06	67	130	26.5	12.0	0.65	0.20	5	8	0.44	-0.42
FV36_5_2†	20	2.05	79	170	35.6	17.0	0.70	0.22	6	7	0.41	-0.38
FV37_5_2†	49	2.05	118	170	45.3	22.3	0.64	0.27	7	7	0.43	-0.30
FV29_3_2†	101	2.06	320	151	54.7	27.6	0.60	0.32	7	8	0.40	-0.17
FV32_4_2†	99	2.05	200	170	54.9	26.4	0.64	0.26	7	9	0.41	-0.09
FV100_19_3	-44	-1.93	195	-158	11.5	-6.0	0.29	0.15	5	-7	0.43	-0.50
FV92_17_3	-29	-1.93	221	-150	33.2	-16.3	0.48	0.20	5	-9	0.41	-0.44
FV107_21_2	0	-1.91	145	-228	36.0	-16.7	0.64	0.14	9	-20	0.30	-0.30
FV90_17_2	22	-1.93	193	-180	45.3	-23.9	0.56	0.21	11	-18	0.32	-0.25
FV92_17_2	50	-1.92	165	-181	56.4	-29.5	0.65	0.23	12	-20	0.32	-0.15
FV94_18_2	101	-1.93	229	-175	61.3	-33.0	0.44	0.22	16	-24	0.31	0.04
FV132_24_2	-48	-0.94	114	-232	16.8	-19.3	0.37	0.16	12	-38	0.31	-0.38
FV91_17_3	-29	-0.96	434	-224	42.2	-48.1	0.44	0.29	11	-31	0.34	-0.36
FV108_21_2	2	-0.95	188	-329	40.2	-45.9	0.44	0.17	21	-95	0.23	-0.20
FV91_17_2	20	-0.95	131	-391	51.2	-56.3	0.55	0.17	22	-103	0.22	-0.14
FV99_19_2	21	-0.96	343	-250	46.0	-55.0	0.42	0.24	18	-90	0.23	-0.21
FV93_17_2	50	-0.95	154	-427	68.2	-71.0	0.76	0.20	17	-97	0.22	-0.02
FV95_18_2	99	-0.96	185	-650	68.8	-85.3	0.62	0.18	23	-125	0.15	0.06
FV94_18_3	-48	-0.47	58	-409	20.7	-34.3	0.45	0.02	21	190	-0.26	-0.31
FV109_21_2	0	-0.47	280	-499	61.0	-124.3	0.48	0.11	28	158	-0.46	-0.18
FV97_18_2	0	-0.47	129	-1111	59.3	-130.0	0.70	0.00	26	133	-0.45	-0.45
FV118_22_2	21	-0.47	206	-740	60.9	-148.8	0.47	0.09	42	184	-0.42	-0.07
FV123_23_2	50	-0.46	278	-571	79.4	-164.0	0.67	0.01	26	168	-0.43	-0.04
FV100_19_2	50	-0.47	127	-909	73.3	-152.0	0.78	0.04	26	133	-0.40	0.10
FV101_19_2	101	-0.46	135	-606	80.5	-172.0	0.76	0.08	29	125	-0.36	0.18
FV134_24_2	-47	-0.23	-304	-6061	12.2	-52.3	-0.26	-0.14	-7	53	0.64	0.76
FV113_22_2	0	-0.22	284	-872	28.0	-119.8	0.06	-0.02	-72	100	3.18	1.69
FV121_23_2	51	-0.22	105	-827	31.0	-145.7	0.24	0.24	286	149	-3.25	-0.48
FV111_22_2	1	-0.07	250	-2222	5.8	-83.5	-0.17	-0.11	-2	50	0.66	0.56
FV116_22_2	22	-0.07	-285	-2500	7.8	-108.0	-0.19	-0.11	-3	57	0.84	0.52
FV125_23_2	53	-0.07	48	-1538	8.8	-126.5	-0.03	-0.09	-5	71	0.96	0.47

†$2R\dot{\theta} = 0.005$ mm/s

Table 5.2: Summary of the tests undertaken using caisson A

Test	$\frac{M_i}{2R}$ N	H_i N	$2R\theta_i$ mm	u_i mm	$\frac{M_m}{2R}$ N	H_m N	$2R\theta_m$ mm	u_m mm	$\frac{M_f}{2R}$ N	H_f N	$2R\theta_f$ mm	u_f mm
FV130_24_2	3	8	0.12	0.05	7	22	0.98	0.38	9	29	1.79	0.81
FV84_14_2	7	23	0.05	0.05	14	47	0.70	0.45	16	55	1.63	0.87
FV85_15_2	10	27	0.04	0.05	21	71	0.84	0.52	23	78	1.68	0.93
FV86_16_2	7	22	0.07	0.04	16	52	0.87	0.49	17	57	1.81	0.96
FV87_16_2	11	37	0.09	0.06	20	65	0.98	0.50	21	70	1.73	0.96
FV88_16_2	14	46	0.05	0.06	25	83	0.83	0.55	26	89	1.72	1.02
FV89_16_2	18	50	0.03	0.04	31	103	0.91	0.59	32	110	1.72	1.14
FV82_14_2	8	10	0.04	0.01	20	36	0.80	0.43	23	42	1.70	0.78
FV26_3_2†	12	15	0.27	0.03	21	38	0.74	0.40	24	44	1.81	0.77
FV35_5_2†	20	33	0.40	0.08	26	51	0.84	0.53	29	54	1.81	0.82
FV34_5_2†	24	36	0.30	0.06	35	62	1.09	0.40	38	68	1.80	0.86
FV33_4_2†	25	46	0.13	0.06	40	77	0.80	0.50	44	82	1.87	0.91
FV30_4_2†	28	35	0.20	0.03	45	81	0.93	0.40	48	90	1.73	0.86
FV99_19_3	2	2	0.08	0.05	8	8	0.89	0.41	10	10	1.75	0.73
FV60_10_2	9	8	0.15	0.08	14	12	0.34	0.16	18	17	0.81	0.36
FV61_10_2	8	8	0.03	0.03	22	21	0.83	0.38	28	25	1.84	0.71
FV27_3_2†	18	11	0.32	0.04	27	26	1.07	0.44	30	29	1.71	0.73
FV57_10_2	20	20	0.12	0.09	35	33	0.44	0.21	39	37	0.82	0.42
FV1_1_2†	14	23	0.03	0.08	42	40	0.86	0.39	45	43	1.64	0.78
FV31_4_2†	26	26	0.16	0.06	55	52	1.00	0.40	59	56	1.65	0.76
FV81_14_2	9	5	0.08	0.06	27	13	1.07	0.43	32	16	1.78	0.75
FV15_2_2†	19	6	0.27	0.05	30	14	0.99	0.31	33	16	1.63	0.70
FV36_5_2†	25	9	0.33	0.06	39	19	0.10	0.37	43	21	1.74	0.67
FV37_5_2†	33	13	0.30	0.08	50	24	1.00	0.40	54	26	1.65	0.70
FV29_3_2†	28	16	0.10	0.11	60	30	1.00	0.45	65	32	1.70	0.73
FV32_4_2†	27	16	0.14	0.10	60	28	1.12	0.36	64	31	1.73	0.74
FV100_19_3	5	-3	0.02	0.02	15	-6	0.60	0.20	20	-10	1.72	0.75
FV92_17_3	19	-6	0.10	0.04	36	-18	0.70	0.30	41	-21	1.67	0.68
FV107_21_2	17	-10	0.13	0.04	44	-19	1.19	0.19	50	-25	1.73	0.53
FV90_17_2	20	-14	0.11	0.07	55	-27	1.05	0.31	61	-32	1.72	0.56
FV92_17_2	35	-21	0.23	0.12	64	-33	0.97	0.35	73	-37	1.73	0.58
FV94_18_2	45	-27	0.20	0.16	67	-36	0.66	0.30	81	-42	1.59	0.55
FV132_24_2	5	-7	0.05	0.03	25	-28	0.85	0.32	36	-37	1.74	0.56
FV91_17_3	12	-34	0.03	0.15	48	-53	0.70	0.40	58	-60	1.60	0.61
FV108_21_2	16	-31	0.10	0.10	52	-55	0.80	0.24	69	-71	1.65	0.42
FV91_17_2	33	-44	0.24	0.11	63	-66	0.93	0.24	78	-82	1.61	0.38
FV99_19_2	15	-51	0.05	0.20	58	-59	0.85	0.27	73	-75	1.60	0.48
FV93_17_2	30	-57	0.20	0.13	80	-80	1.15	0.26	89	-94	1.69	0.40
FV95_18_2	32	-82	0.16	0.16	82	-88	0.96	0.19	96	-100	1.62	0.29
FV94_18_3	10	-14	0.18	0.03	31	-64	0.84	-0.08	49	-101	1.67	-0.30
FV109_21_2	26	-55	0.09	0.11	76	-156	0.73	0.05	88	-189	1.18	-0.15
FV97_18_2	24	-54	0.20	0.05	75	-160	1.04	-0.10	91	-191	1.66	-0.36
FV118_22_2	25	-55	0.13	0.07	80	-180	0.76	0.03	99	-208	1.18	-0.15
FV123_23_2	17	-57	0.08	0.10	100	-206	1.08	0.04	109	-239	1.48	-0.19
FV100_19_2	40	-80	0.30	0.08	85	-185	1.00	-0.07	101	-214	1.66	-0.32
FV101_19_2	49	-44	0.37	0.07	90	-209	0.94	-0.21	111	-236	1.66	0.24
FV134_24_2	6	-21	-0.02	0.00	16	-73	-0.57	-0.38	19	-86	-1.05	-0.65
FV113_22_2	22	-32	0.08	0.35	32	-154	0.05	-0.27	37	-170	-0.04	-0.40
FV121_23_2	31	-39	0.24	0.05	31	-185	0.24	-0.09	41	-209	0.27	-0.27
FV111_22_2	3	-40	0.00	-0.02	7	-97	-0.35	-0.09	8	-114	-0.86	-0.60
FV116_22_2	6	-43	-0.03	0.01	9	-124	-0.35	-0.24	10	-140	-0.70	-0.56
FV125_23_2	4	-43	0.03	0.03	10	-148	0.11	-0.22	11	-166	-0.36	-0.48

†$2R\dot{\theta} = 0.005$ mm/s

Table 5.3: Summary of the tests undertaken using caisson B

Test	V' N	$\frac{M}{2RH}$	$K_{m\,i}$ $\frac{N}{mm}$	$K_{h\,i}$ $\frac{N}{mm}$	$\frac{M_y}{2R}$ N	H_y N	$2R\theta_y$ mm	u_y mm	$K_{m\,f}$ $\frac{N}{mm}$	$K_{h\,f}$ $\frac{N}{mm}$	$\frac{\delta u^p}{2R\delta\theta^p}$	$\frac{\delta w^p}{2R\delta\theta^p}$
FV131_24_2	-49	0.30	65	326	8.3	21.6	0.45	0.35	3	13	0.86	-0.55
FV42_6_2†	0	0.54	289	250	17.2	32.5	0.18	0.26	14	24	0.93	-0.40
FV45_7_2	0	0.57	320	250	21.9	38.8	0.22	0.29	13	24	0.92	-0.34
FV38_6_2†	21	0.54	315	350	22.4	40.3	0.23	0.27	11	21	0.92	-0.28
FV46_7_2	21	0.57	763	410	25.2	44.1	0.17	0.25	16	29	0.95	-0.32
FV47_7_2	50	0.57	756	501	29.1	51.3	0.18	0.25	16	28	1.01	-0.21
FV48_7_2	101	0.56	1256	426	34.4	59.6	0.17	0.27	17	30	1.04	-0.06
FV102_20_3	-57	1.05	256	176	24.3	20.9	0.44	0.35	8	10	0.86	-0.61
FV40_6_2†	1	1.06	170	250	24.8	24.5	0.24	0.20	21	23	0.84	-0.27
FV49_8_2	1	1.07	850	651	31.9	28.0	0.18	0.21	23	20	1.18	-0.36
FV41_6_2†	21	1.06	543	352	27.6	25.8	0.16	0.20	22	24	0.76	-0.22
FV50_8_2	21	1.02	431	151	35.4	33.8	0.20	0.30	22	22	0.93	-0.28
FV51_8_2	52	1.07	1352	190	40.7	39.0	0.18	0.30	25	25	0.98	-0.17
FV52_8_2	101	1.07	2002	241	45.1	42.7	0.15	0.30	24	22	0.99	-0.04
FV129_24_2	-49	2.08	168	169	24.5	10.4	0.45	0.32	10	6	0.81	-0.46
FV53_9_2	1	2.08	756	136	35.9	16.3	0.16	0.20	30	18	0.90	-0.30
FV54_9_2	19	2.08	896	236	43.9	19.1	0.20	0.20	30	18	0.97	-0.25
FV55_9_2	51	2.08	1000	351	42.5	18.6	0.15	0.16	30	18	0.92	-0.11
FV56_9_2	103	2.07	1100	166	52.9	24.2	0.17	0.26	31	18	0.94	0.01
FV124_23_2	21	-0.70	756	-333	102.0	-140.0	0.21	-0.26	115	222	-0.62	-0.25
FV135_24_2	-46	-0.46	1215	-1111	30.0	-65.0	-0.08	-0.08	-26	45	1.21	0.83
FV117_22_2	2	-0.46	-4000	-644	48.6	-98.0	-0.05	0.01	-81	92	1.91	0.80
FV122_23_2	20	-0.44	3333	-649	55.0	-112.0	-0.04	0.03	-66	81	1.88	0.80
FV133_24_2	-46	-0.20	-100	1326	7.3	-34.1	-0.16	-0.16	-8	33	0.98	0.73
FV112_22_2	1	-0.21	-356	-1538	14.6	-68.0	-0.14	-0.13	-10	38	1.24	0.53
FV126_23_2	22	-0.21	-1200	-1326	16.6	-80.0	-0.12	-0.10	-12	45	1.24	0.50
FV110_22_2	2	-0.06	-90	2600	3.4	-63.7	-0.19	-0.20	-1	28	1.03	0.43
FV120_23_2	22	-0.05	-35	14500	4.1	-71.1	-0.27	-0.21	-1	26	1.15	0.45

†$2R\dot{\theta}$ = 0.005 mm/s

separates from the other test curves after $2R\theta > 0.6$ mm of rotation has occurred.

Figures 5.4(a), (b), (c) and (d) show examples of test results using caisson B and a loading ratio of $\frac{M}{2RH} = 1$ over a range of vertical loads. Although caisson B was rotated half of the total rotation applied to caisson A (except test FV102_20_3), a similar type of load-displacement response is observed in Figures 5.4(a) and (b). It is worth noting in these figures the increase of moment load capacity as well as lateral load capacity with the increase of vertical load. It is remarkable that the caisson rotated under very high tension load (V' = -57 N) still has a significant moment and lateral load resistance. In the displacement curves shown in Figure 5.4(c) the magnitudes of u and $2R\theta$ are similar, contrarily to the displacement curves shown in Figure 5.3(c), where the magnitude of u was around half of $2R\theta$. Furthermore, Figure 5.4(d) shows that there is a reduction in

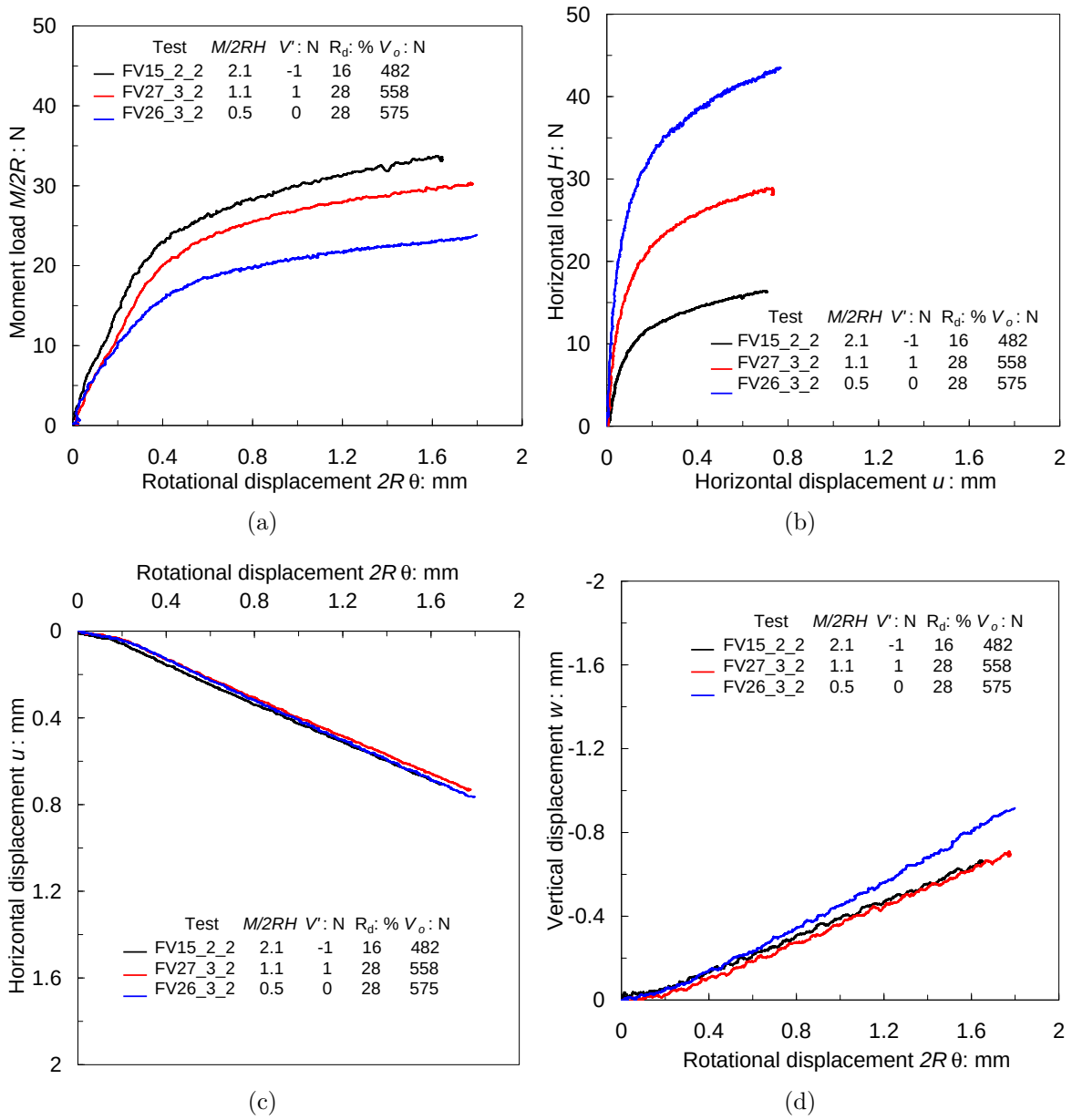

Figure 5.3: Rotational tests using caisson A under constant vertical load $V' = 0$ N at different ratios of $\frac{M}{2RH}$

the caisson uplift when the vertical load increases. During the rotation under tension the caisson uplift was the highest, as would be expected.

Another group of tests using caisson A under zero vertical load is shown in Figures 5.5(a) and 5.5(b), but for negative loading ratios $\frac{M}{2RH}$. Tests with $\frac{M}{2RH}$ = -1.9 and -1 were conducted as before, *i.e.* under rotational displacement control. As a result of the large increase in the magnitude of horizontal displacements and hence horizontal loads, rotational displacement controlled tests were not well suited for the range of loading ratios of

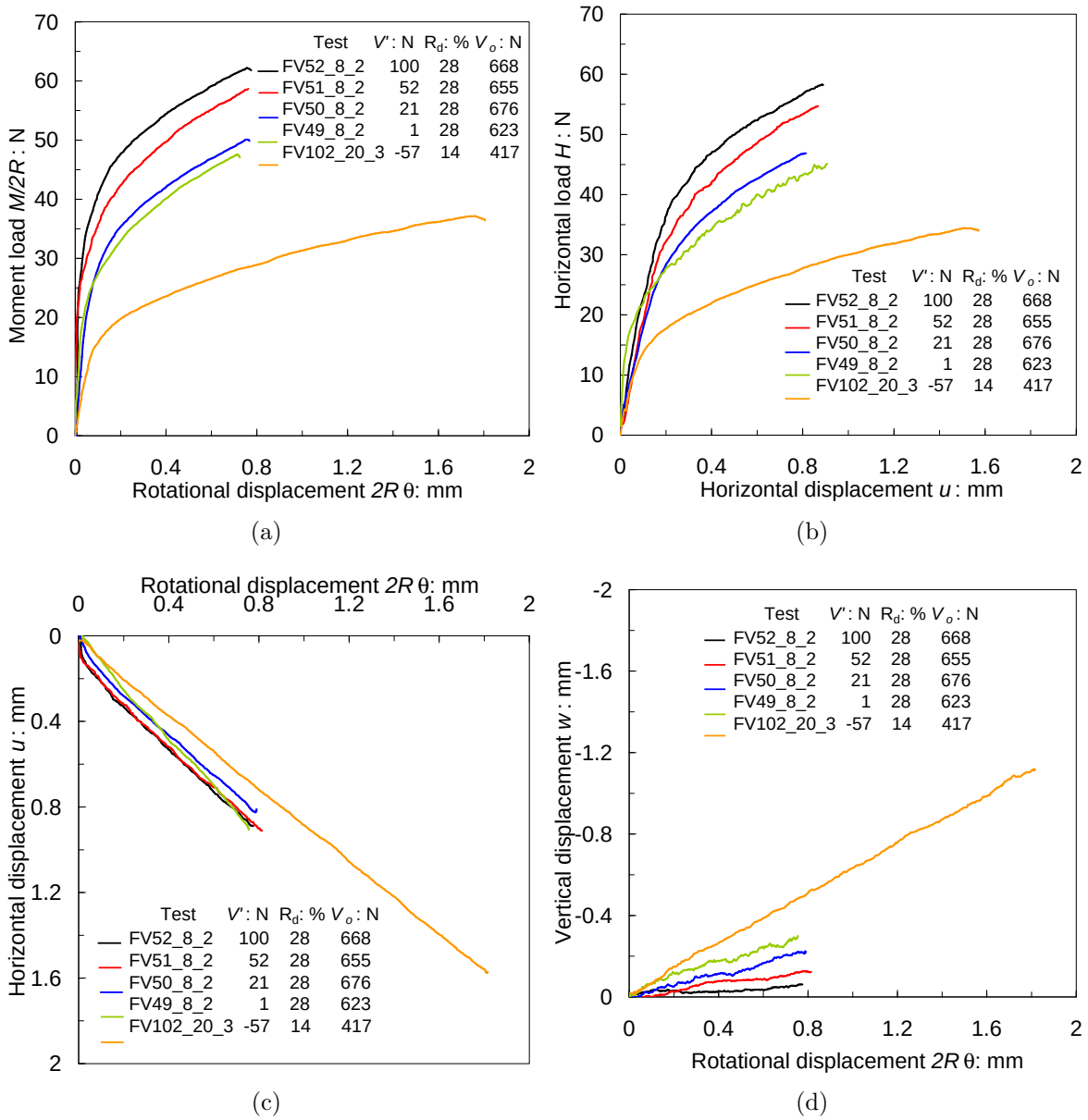

Figure 5.4: Rotational tests using caisson B under a constant load ratio of $\frac{M}{2RH} = 1$ at different vertical loads V'

$0 > \frac{M}{2RH} >$ -1. This was because this type of test put the caisson in a loading condition close to pure sliding. For these tests the horizontal displacement was controlled instead of the rotational displacement. The response pattern followed by the caisson in the tests with negative $\frac{M}{2RH}$ can be interpreted as before, but for the test under $\frac{M}{2RH}$ = -0.5 the pronounced initial stiff response and final softer response are harder to delimit. Changes in the displacement directions from positive to negative are observed in three tests. Figure 5.5(c) shows how the displacement curves $u - 2R\theta$ vary anticlockwise as the loading ratio $\frac{M}{2RH}$ changes from -1.9 to -0.1, giving evidence of a great displacement ratio gradient. The displacement ratio gradient is the variation of a displacement with respect to the variation

of another displacement, for example $\frac{\delta u}{2R\delta\theta}$. This gradient will be considered in subsequent sections to study the flow rule using the values of plastic displacement summarized in Tables 5.1 and 5.3. Under $\frac{M}{2RH}$ = -0.2 the caisson rotates less than 0.1 mm, returning at the end at the initial position. Notwithstanding that the tests with $\frac{M}{2RH}$ = -0.2 and -0.1 switched the rotation direction, Figure 5.5(d) shows that they have similar magnitudes of w as the other tests that did not switch rotation direction.

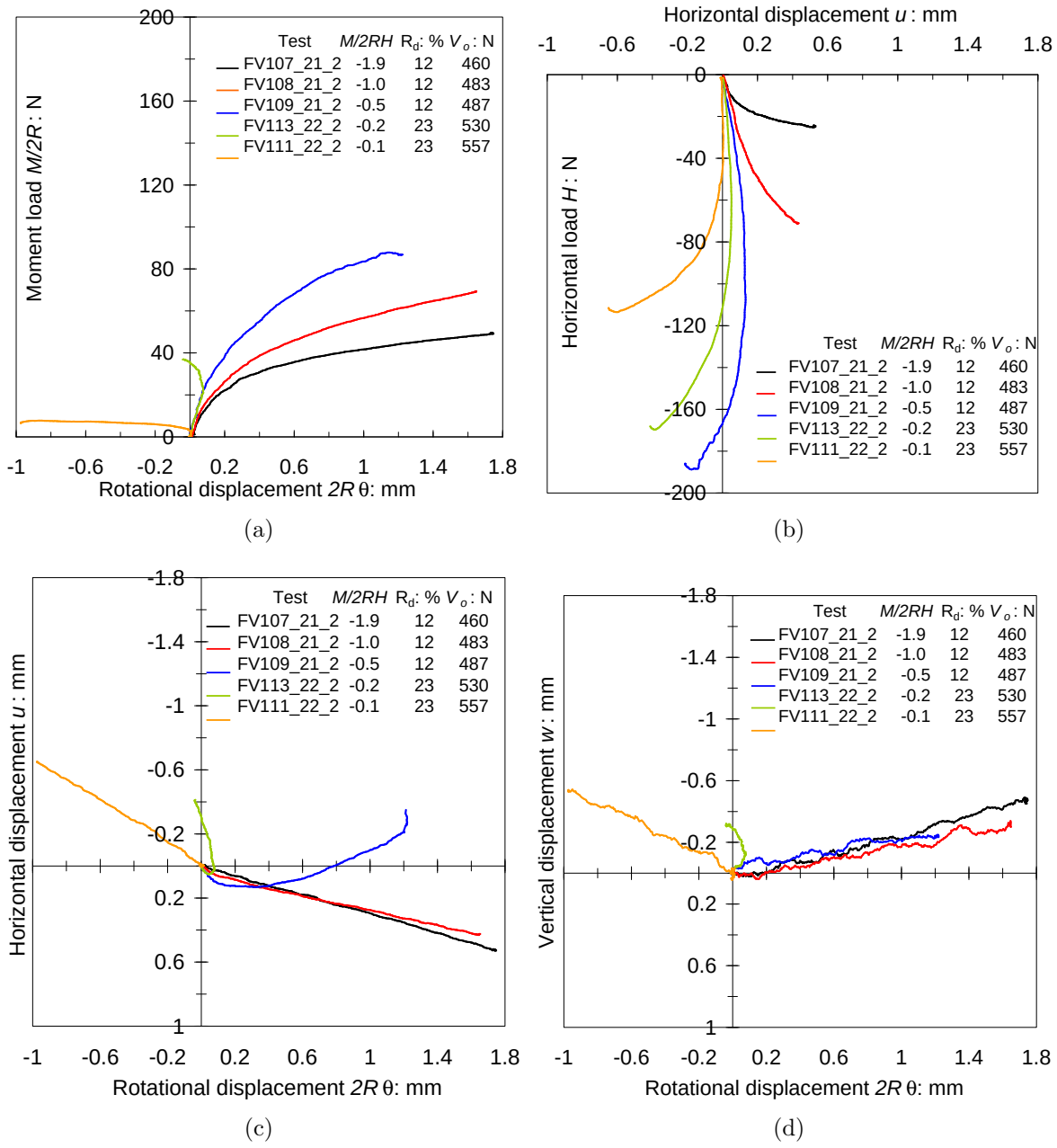

Figure 5.5: Rotational and translational tests using caisson A under a constant vertical load V' = 0 N at different ratios $\frac{M}{2RH}$

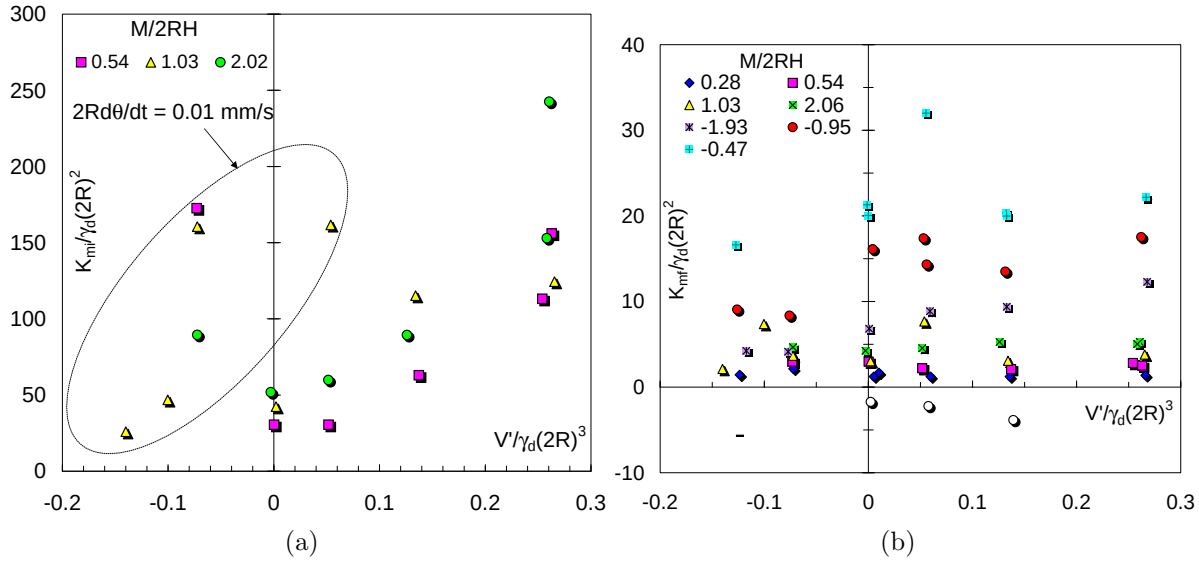

Figure 5.6: (a) Initial moment stiffness K_{mi} for caisson A. The encircled left side of the plot corresponds to tests under $2R\dot{\theta} = 0.01$ mm/s, the other points correspond to $2R\dot{\theta} = 0.005$ mm/s, and (b) final moment stiffness K_{mf} for caisson A

The difference in the rotational velocity $2R\dot{\theta}$ applied to the caisson has an effect on the initial load-displacement response. The initial slopes of the $\frac{M}{2R} - 2R\theta$ and $H - u$ curves changed according to $2R\dot{\theta}$ (see Tables 5.1 and 5.3). Figure 5.6(a) shows that the normalised foundation initial moment stiffness K_{mi} increased when the rotational velocity changed from $2R\dot{\theta} = 0.005$ mm/s to 0.01 mm/s. However, it will become apparent later that this rate difference does not influence noticeably the determination of yield points and the yield surface. On the other hand, Figure 5.6(b) shows that there is little influence on the final moment stiffness of the foundation K_{mf} either from the rotational velocity or from the vertical load. However, an influence of the loading ratio can be seen.

5.4 ANALYSES OF THE RESULTS

5.4.1 Yield surface

Yield is a gradual process where irreversible deformation occurs. Because soil is not a continuum but a particulate material this is a broad definition. It has been found that irreversible deformations start to develop at early stages where for instance in sandy soils shear strains are as small as 0.002% (Chaudhary and Kuwano, 2003; Mitchell and Soga, 2005). In practical terms, yield can be understood as the transition from a load-

displacement state with small magnitudes of irreversible deformation to another state with large magnitudes of irreversible deformation. Although the latter definition narrows the range for a definition of yield, it is not sufficient to link yield with a unique loading state.

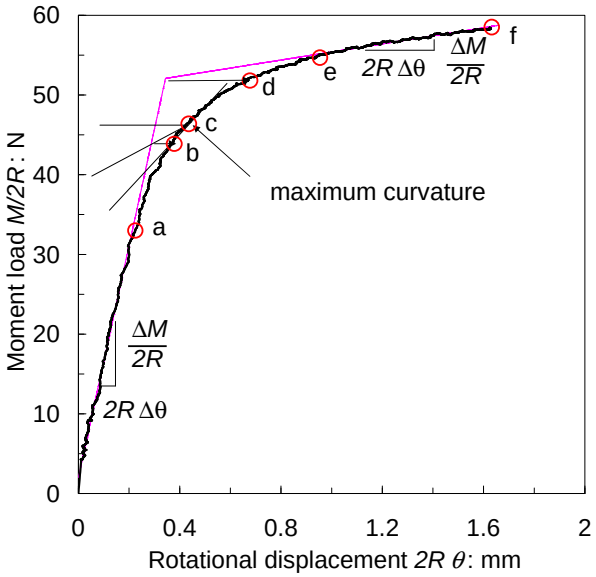

Figure 5.7: Five criteria for the determination of the yield point (test FV31_4_2A)

In order to visualise a yield point determination Figure 5.7 shows an example of a $\frac{M}{2R} - 2R\theta$ response with circles indicating the gradual progress of yield according to five criteria. The first criterion (a) establishes that yield occurs at the end of a linear response, *i.e.* when the ratio between the moment load variation $\frac{\Delta M}{2R}$ and the rotational displacement variation $2R\Delta\theta$ is not longer constant and commences to reduce. The second criterion (b) corresponds to the procedure used in consolidation analysis to determine the preload of a soil sample in oedometer tests (Terzaghi, 1943; Poorooshasb *et al.*, 1967). The third criterion (c) defines yield as the point of maximum curvature on the $\frac{M}{2R} - 2R\theta$ curve (McDowell, 2002). The fourth criterion (d) determines yield as the intersection of the two straight lines that fit the experimental curve at the beginning and at the end of the curve (Graham *et al.*, 1982). To obtain the displacement associated to the yield load the intersection point must be translated to the curve as illustrated in Figure 5.7. The fifth criterion (e) is the inverse of the first criterion in the sense that yield occurs when a linear response commences, resulting in a constant ratio between $\frac{\Delta M}{2R}$ and $2R\Delta\theta$, and lowest during the loading process. Finally the sixth circle (f) is not a criterion, but the final

loading state once the test has finished.

Values of yield points obtained according to criteria (a), (d), (e) and the final circle (f) are summarised in Tables 5.1 and 5.2. Figures 5.8(a), (b), (c), (d), (e) and (f) show these yield points plotted in a normalised plane of moment load *versus* normalised horizontal load. Criteria (b) and (c) are less reliable since they involve determination by eye or by a 'best' curve fit, leading to a scale dependency. Observing these yield point plots for each vertical load V a pattern of progression is visible from state (a) to state (f), showing a yield surface expansion. In addition, this expansion in each group of yield points shows that the initial state (a) separates clearly from states (d), (e) and (f) which are relatively close to each other in the first and third quadrants; they are further apart in the second and fourth quadrants (when $\frac{M}{2R}$ and H have opposite sign). A comparison between Figure 5.8(c) and the plot for $\frac{L}{2R} = 0.5$ in Figure 5.2(a) shows similarities in shape and inclination, considering the absence of friction assumed in the calculations ($F_h = 0$), which reduces the size and squats the yield surface.

Figures 5.9(a), (b), (c) and (d) show the evolution of yield points with V' and $\frac{M}{2RH}$. These plots confirm that criterion (d) is more suitable to interpret yield due to irreversible plastic displacements. This criterion proved to be consistent and repeatable in determining yield points as pointed out in an earlier study by Byrne *et al.* (2003). Less favourable cases exist for the range -2 $\leq \frac{M}{2RH} \leq$ -0.2 in the second and fourth quadrants where criterion (d) gives a lower boundary of the yield surface, but (d) still is close to the medium and final states than to the initial state.

A rational and repeatable procedure that minimises personal influences was implemented following Graham *et al.* (1982) to determine yield points using criterion (d). This method was used due to its simplicity and the consistency of the results. The least square error method was used to fit the data employing a bilinear function with a slope discontinuity at $x = c$ where x is the displacement. For a planar analysis x can represent w (as used in Chapter 3 for the determination of yield points in vertical loading tests of caissons in

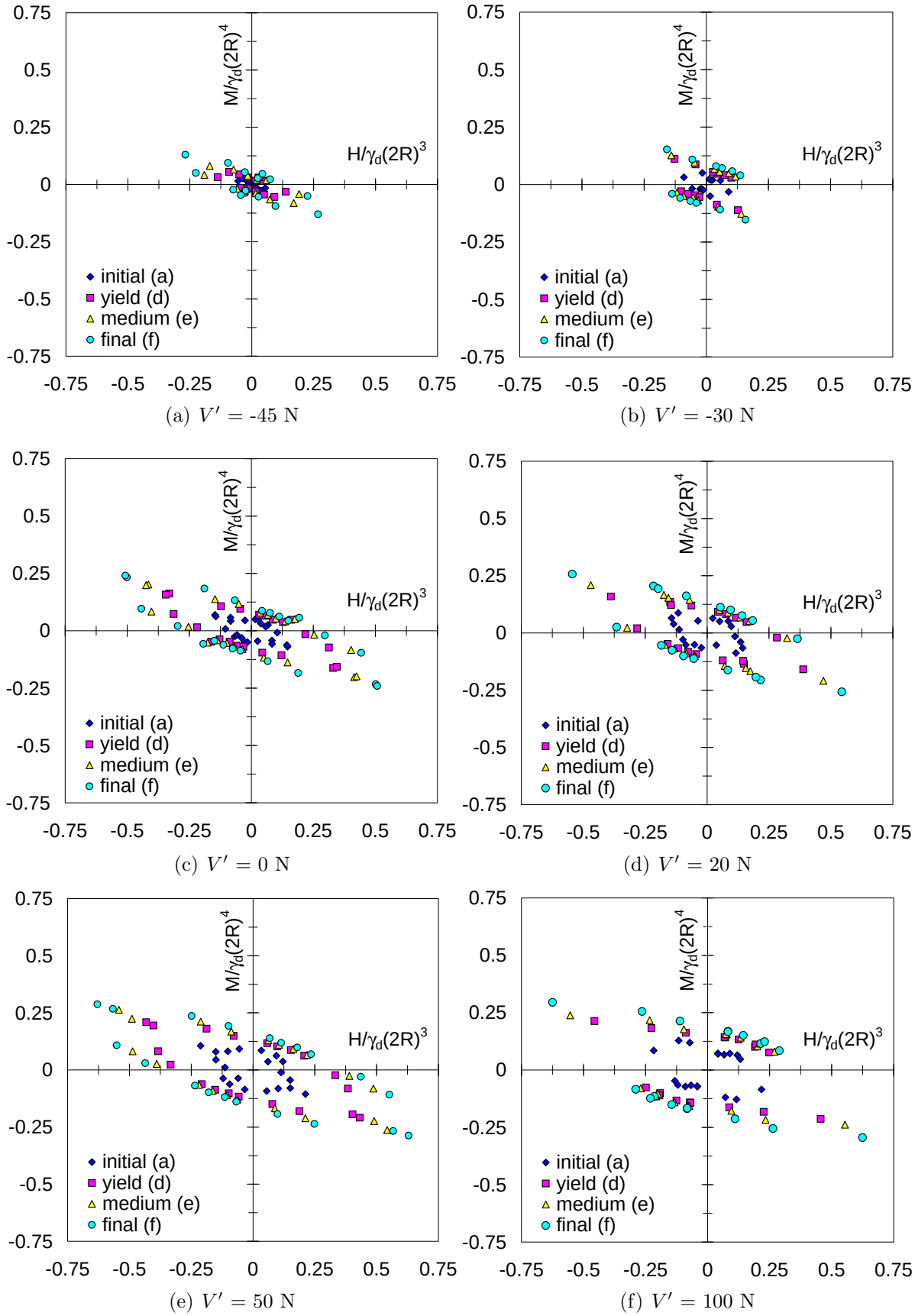

(a) $V' = -45$ N (b) $V' = -30$ N

(c) $V' = 0$ N (d) $V' = 20$ N

(e) $V' = 50$ N (f) $V' = 100$ N

Figure 5.8: Variation of yield points along loading for caisson A in the plane of moment load and horizontal load (V' is an average nominal value, for exact values of V' see Table 5.1)

loose sand), $2R\theta$, and u. The displacement x at c does not have a physical meaning; it is used only to find the load y at yield.

$$y = y_o + ax \quad \text{for} \quad x < c; \qquad y = y_o + ax + (b-a)[x-c] \quad \text{for} \quad x \geq c \tag{5.24}$$

Where y_o is the initial load at $x = 0$, a and b are the slope of the initial and final linear sections equal to $\frac{\Delta M}{(2R)^2 \Delta\theta}$ in a moment load-rotational displacement curve and $\frac{\Delta H}{\Delta u}$ in a lateral load-translational displacement curve. The values of these slopes are summarised in Table 5.1 as K_{mi} and K_{hi} for the initial linear section and K_{mf} and K_{hf} for the final

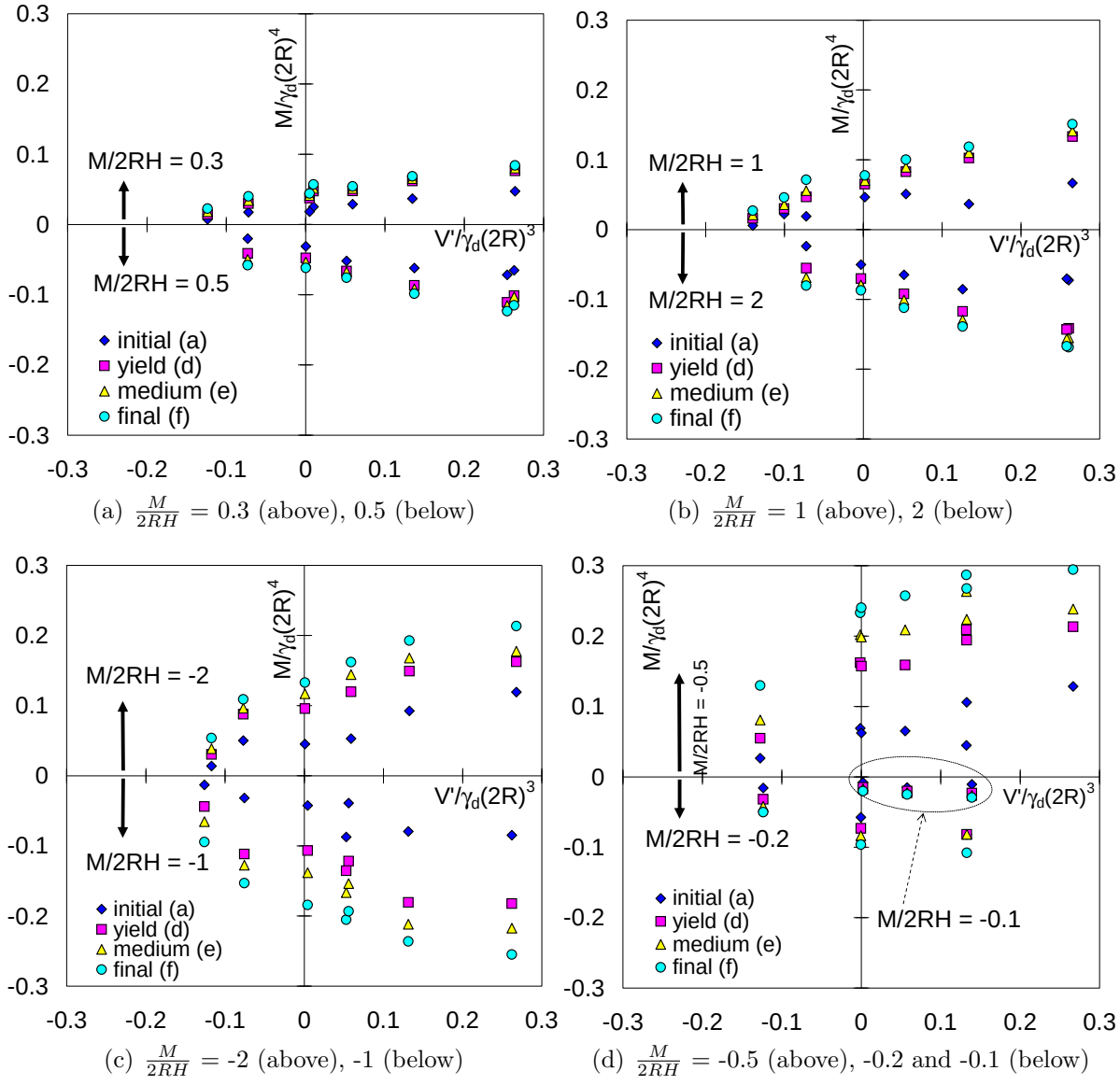

(a) $\frac{M}{2RH}$ = 0.3 (above), 0.5 (below)

(b) $\frac{M}{2RH}$ = 1 (above), 2 (below)

(c) $\frac{M}{2RH}$ = -2 (above), -1 (below)

(d) $\frac{M}{2RH}$ = -0.5 (above), -0.2 and -0.1 (below)

Figure 5.9: Variation of yield points along loading for caisson A in the plane of moment load and vertical load ($\frac{M}{2RH}$ is an average nominal value, for exact values of $\frac{M}{2RH}$ see Table 5.1)

linear section. In general the initial foundation stiffness is much larger than the final stiffness and it increases with the soil density and the vertical load. This is not the case for the final stiffness, where there is no influence of the vertical load, but the loading ratio $\frac{M}{2RH}$ influences the final response instead as shown in Figure 5.6(b).

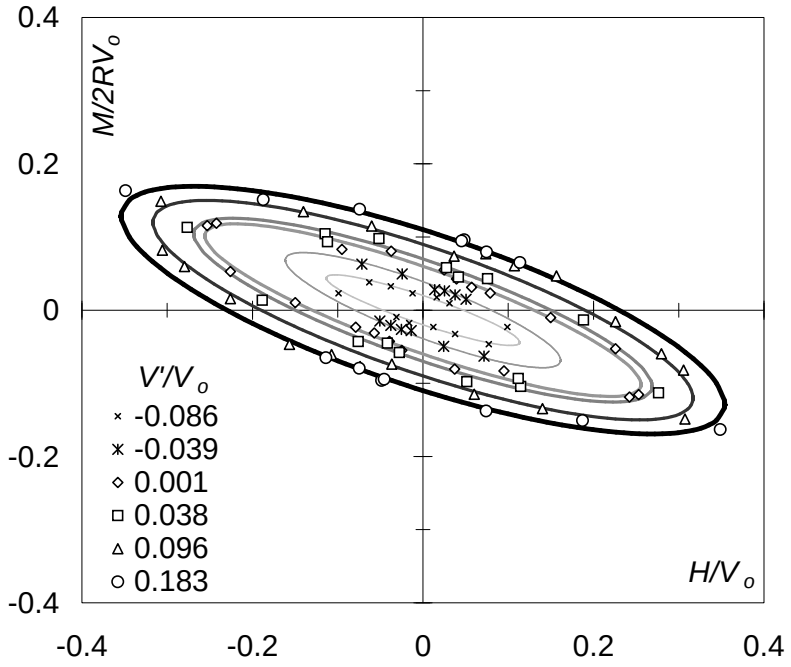

Figure 5.10: Yield points (d) determined from experiments using caisson A in the normalised $\frac{M}{2RV_o} - \frac{H}{V_o}$ plane and expression (5.25) fitted

The yield points obtained using the two straight lines method were normalised by V_c to interpret the results according to the hyperplasticity theory. Subsequently, yield points were plotted in a plane of nondimensional moment load and horizontal load $\frac{M}{2RV_c} - \frac{H}{V_c}$, assuming that V_c gives a better representation of V_o as discussed in Chapter 4. The nought subscript o is used henceforth to keep the same nomenclature used in the theoretical formulation. Figure 5.10 shows that the normalised yield points form non-symmetric ellipses in the $m - h$ plane ($\frac{M}{2RV_o} - \frac{H}{V_o}$) for different values of $\nu = \frac{V'}{V_o}$; the ellipses are rotated according to the eccentricity e, which from the figure it seems to be the same for all the ellipses. It is worth noting that the maximum combined loading capacity is found when m and h have different sign at the ellipse apices. On the other hand, the minimum loading capacity occurs when m and h are positive, which not only corresponds to the main loading on a foundation, but also controls the design. There are also in Figure 5.10 fitted curves constructed using equation (5.11), but reduced to the planar case, resulting

in:

$$y = \left(\frac{H}{h_i V_o}\right)^2 + \left(\frac{M}{2Rm_i V_o}\right)^2 - 2e\frac{H}{h_i V_o}\frac{M}{2Rm_i V_o} - 1 = 0 \tag{5.25}$$

where h_i and m_i represent the intersection of each ellipse with the axis $\frac{H}{V_o}$ and $\frac{M}{2RV_o}$ respectively, and e is the eccentricity of each ellipse. Values of the parameters m_i, h_i and e were determined using the least square error method; they are presented in Tables 5.4 and 5.5. Yield points were normalised as mentioned before by the respective V_o obtained from each test, but for the fit analysis an average value was used for each of the vertical loads V' shown in Tables 5.4 and 5.5. An increase of h_i and m_i with the normalised vertical load $\frac{V'}{V_o}$ was found previously by Martin (1994) for spudcan tests in clay. Indeed, Figures 5.11(a) and 5.11(b) show clearly this trend for both caissons. In addition, two fitted curves to the data were obtained by means of the following two equations:

$$h_i = \frac{H_i}{V_o} = h_o \left[\frac{(\beta_1+\beta_2)^{\beta_1+\beta_2}}{\beta_1^{\beta_1}\beta_2^{\beta_2}(t_o+1)^{\beta_1+\beta_2}}\right]\left(\frac{V'}{V_o}+t_o\right)^{\beta_1}\left(1-\frac{V'}{V_o}\right)^{\beta_2} \tag{5.26}$$

$$m_i = \frac{M_i}{2RV_o} = m_o \left[\frac{(\beta_1+\beta_2)^{\beta_1+\beta_2}}{\beta_1^{\beta_1}\beta_2^{\beta_2}(t_o+1)^{\beta_1+\beta_2}}\right]\left(\frac{V'}{V_o}+t_o\right)^{\beta_1}\left(1-\frac{V'}{V_o}\right)^{\beta_2} \tag{5.27}$$

Equations (5.26) and (5.27) proposed by Martin (1994), but without the tension parameter t_o, introduce the parameters β_1 and β_2 which play two roles. Firstly they shift the maximum normalised moment load m_o or the maximum horizontal load h_o from the middle along the normalised vertical load axis whilst keeping the same peak values by means of β_{12} (expression (5.17) shown in square brackets in (5.26) and (5.27)). Secondly, the tangent at the edges of the yield surface, *i.e.* at $t_o = \frac{V_t}{V_o}$ and $\frac{V'}{V_o} = 1$ can be changed from the parabolic case when $\beta_1 = \beta_2 = 1$. For the particular case of $\beta_1 < 1$ and $\beta_2 < 1$ the tangent increases, which can provide a better fit to the data. Figure 5.11(a) also highlights in a circle the parameter α which corresponds to the point in the normalised vertical load axis where the peaks m_o and h_o are located, also shown in circles. Although a visual observation of the ellipses does not clearly indicate a difference in inclination of the ellipse axes, a variation of the eccentricity with $\frac{V'}{V_o}$ was found as shown in Figures 5.12(a), and 5.12(b) where linear and parabolic best fit curves are included.

A better fit is obtained with a parabolic equation instead of a linear fit, as can be ob-

Table 5.4: Intersection and eccentricity parameters: h_i, m_i and e (caisson A)

V': N	V'/V_o	V_o: N	V_o st dev: N	h_i	m_i	e
-47	-0.086	548	71	0.047	0.020	-0.91
-29	-0.039	734	58	0.080	0.039	-0.87
1	0.001	553	103	0.130	0.060	-0.86
21	0.038	561	81	0.150	0.070	-0.83
51	0.096	531	35	0.190	0.090	-0.80
100	0.182	552	86	0.230	0.110	-0.76

Table 5.5: Intersection and eccentricity parameters: h_i, m_i and e (caisson B)

V': N	V'/V_o	V_o: N	V_o st dev: N	h_i	m_i	e
-49	-0.102	484	54	0.055	0.030	-0.92
1	0.002	563	101	0.115	0.064	-0.83
21	0.036	572	117	0.140	0.080	-0.83
51	0.080	640	14	0.160	0.090	-0.79
102	0.148	689	16	0.190	0.100	-0.75

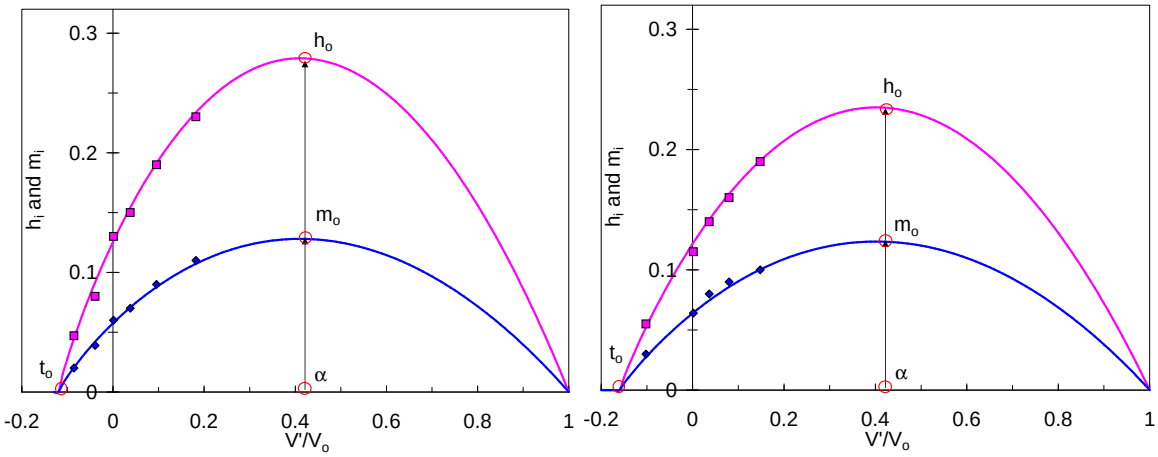

(a) Caisson A (b) Caisson B

Figure 5.11: Intersection points h_i and m_i as a function of the normalised vertical load $\frac{V'}{V_o}$

served in Figures 5.12(a) and 5.12(b), for that reason the parabolic expressions were used in subsequent calculations. Another reason for choosing parabolic equations is because they allow the variation of e, as found by Martin (1994), for higher values of ν, so extrapolation of e using the above parabolic equations is possible, which is not the case when using linear equations. Values of the parameter obtained from the best curve fits using the experimental results are summarised in Table 5.6. Figure 5.13 shows the normalised yield points projected in the $\frac{M}{2RV_o} - \frac{V'}{V_o}$ plane with the best fit curves using equation (5.11)

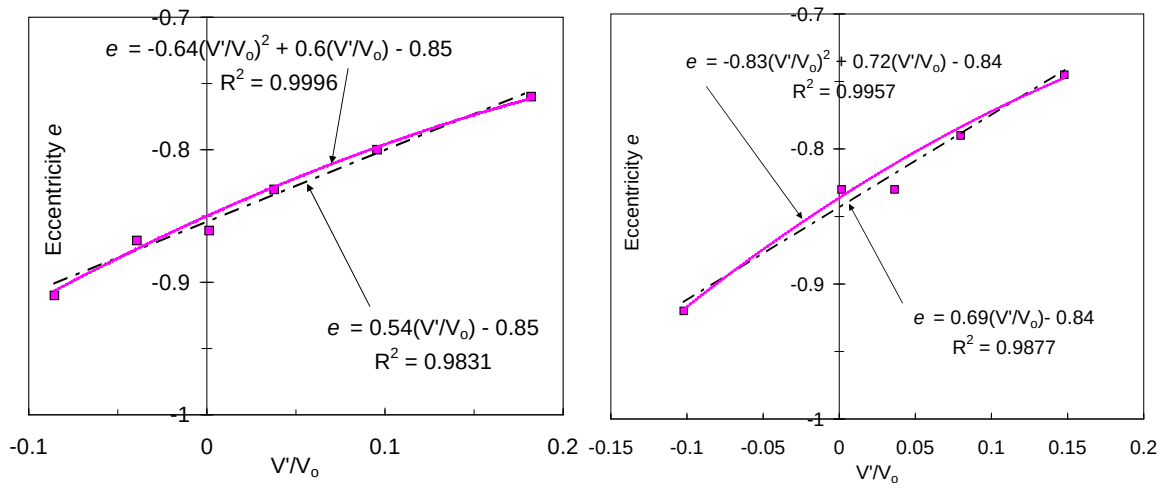

(a) Caisson A (b) Caisson B

Figure 5.12: Eccentricity as a function of the normalised vertical load $\frac{V'}{V_o}$

in the following form and the parameter values listed in Table 5.6:

$$y = \left(\frac{H}{h_o V_o}\right)^2 + \left(\frac{M}{2Rm_o V_o}\right)^2 - 2e\frac{H}{h_o V_o}\frac{M}{2Rm_o V_o} - \beta_{12}^2 \left(\frac{V'}{V_o} + t_o\right)^{2\beta_1} \left(1 - \frac{V'}{V_o}\right)^{2\beta_2} = 0 \quad (5.28)$$

Expression (5.28) captures too the trend followed by the experimental yield points in the $m - \nu$ plane with the fitted parameters. However, the yield surface slightly under predicts the yield points. The values of $t_o = 0.12$ and 0.16 obtained from the best fit of the data are larger than the value obtained from the pullout tests ($t_o \approx 0.10$ and 0.12, see Chapter 4). It seems that the caisson installation reduces the tension capacity due to the rearranging of grains sheared during the skirt penetration. The soil plug weight has been included as a circle in the $\frac{V'}{V_o}$ axis because of the potential application to caisson dimensioning. A view of the yield surface in three dimensions is shown in Figure 5.14 for low vertical loads and for intervals of 50 N along the vertical load axis.

Moment capacity tests carried out with caisson B were intended to investigate the effect that a different caisson geometry causes on the determination of a yield surface. Although the series of tests were not as numerous as for caisson A (see Table 5.3), it was sufficient to define the type of variation of the model parameters. Following the same criterion and procedures to determine yield points and yield surface parameters the set of values obtained for caisson B is also shown in Table 5.6 ($\frac{L}{2R} = 1$, $\frac{t}{2R} = 1.67\%$). How-

Table 5.6: Parameters suggested for the yield surface and flow rule expressions

Parameter	$\frac{L}{2R} = 0.5$	$\frac{L}{2R} = 1$	$\frac{L}{2R} = 1$
Thickness ratio, $t/2R$: %	1.16	1.67	1.16
Eccentricity of yield surface (average), e	-0.84	-0.87	-0.87
Contact vertical load (average), $V_c \Rightarrow V_o$: N	580	590	512
Maximum pure pullout load (average), V_t: N	-70	-94	-82
Tension factor, t_o	0.12	0.16	0.16
Dimension of yield surface (horizontal), h_o	0.279	0.235	0.300
Dimension of yield surface (moment), m_o	0.128	0.124	0.145
Curvature factor for yield surface (low V'), β_1	0.89	0.93	0.96
Curvature factor for yield surface (high V'), β_2	0.99	0.99	0.99

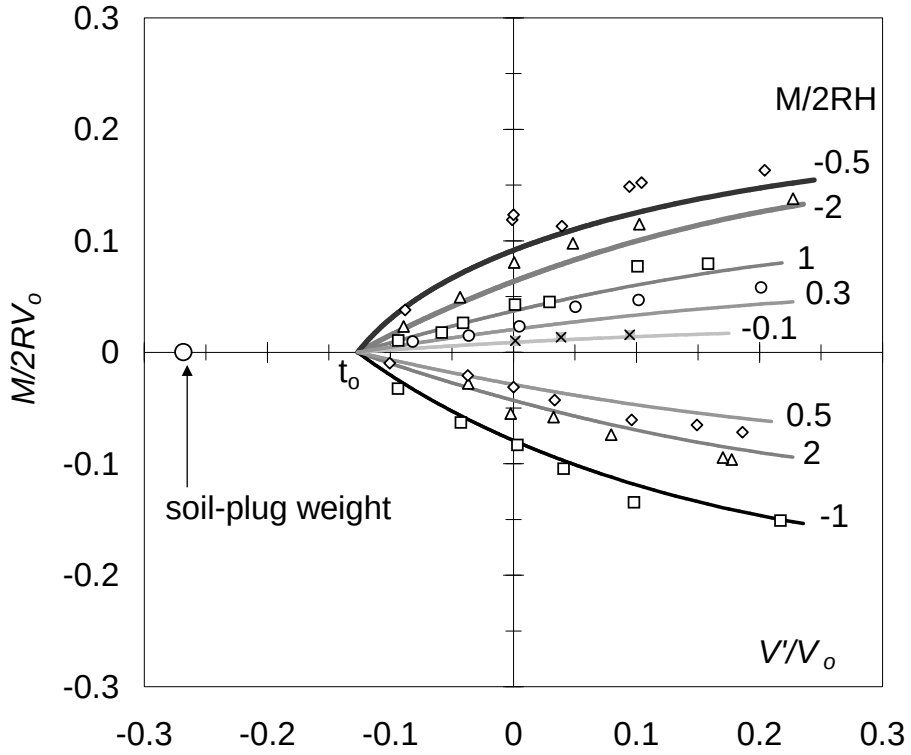

Figure 5.13: Normalised yield points in the $\frac{M}{2RV_o} - \frac{V'}{V_o}$ plane and expression (5.28) fitted for caisson A

ever, a direct comparison of these parameters with the ones obtained for caisson A is not possible because the scaling does not match for the caisson wall thickness t. Villalobos *et al.* (2005) point out that V_o is, amongst other parameters, a function of t and because of that m_o and h_o obtained for both caissons cannot be directly compared.

An option to compare both caissons without the bias of the thickness, is for example instead of repeating the testing, to recalculate V_o for caisson B as presented in Chapter 4, but with the same thickness ratio of caisson A ($\frac{t}{2R} = 1.16$), which means to adopt t

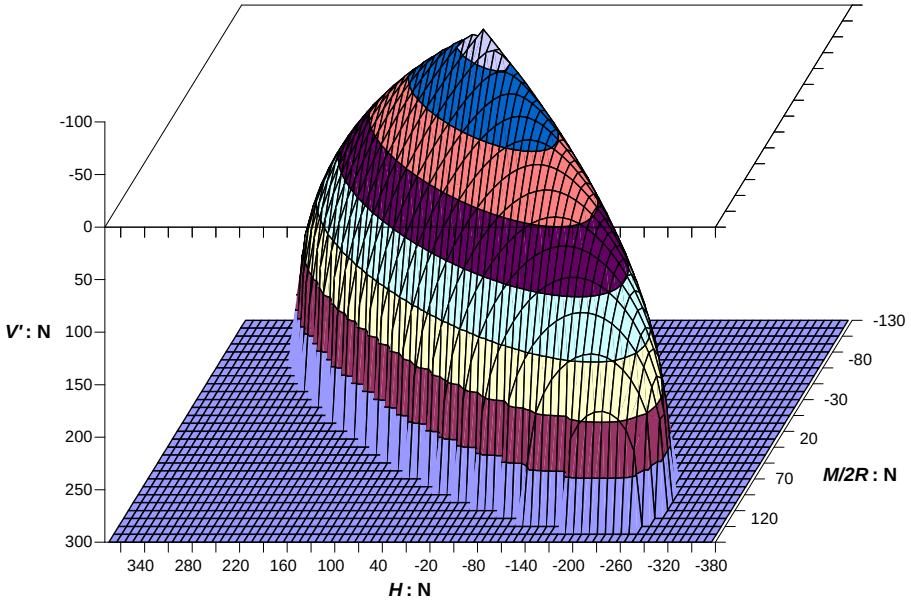

Figure 5.14: A 3D view of the yield surface for caisson A, showing the side of low vertical loads

= 2.4 mm instead of 3.4 mm. Recalculate means that V_o is first calculated to calibrate the installation model parameters ($K \tan \delta$) using the installation test results for caisson B and subsequently V_o is recalculated for $t = 2.4$ mm. A parallel line was found to the previously determined relationship between V_o and γ_d (or V_c - γ_d as shown in Chapter 4), which corroborates that V_o is a linear function of t. The results obtained from this exercise are shown in the last column of Table 5.6.

Figure 5.15(a) shows the range of values of the eccentricity e obtained in this study compared with previous values obtained for caissons with different aspect ratios. For aspect ratios from 0 to 0.5 a significant variation of eccentricity occurs according to the three sources of data. The results obtained in this study are shown in Figure 5.15(a) as average values (in circle) with the bars representing the variation which is a function of the vertical load ratio. It is clear that for caisson aspect ratios between 0.5 and 1 e tends to a fairly constant value.

The values of m_o and h_o as a function of the caisson aspect ratio are plotted in Figure 5.15(b). There are two values of m_o and h_o obtained in this study for $\frac{L}{2R} = 1$ due to a variation in thickness ratio, as presented in Table 5.6. Additionally, Figure 5.15(b)

shows values of m_o and h_o from the work of Cassidy (1999) and Byrne (2000). In spite of the scatter, both sets of h_o and m_o follow roughly similar trends (removing the point h_o for $\frac{L}{2R} = 0.66$). The scatter can be the result of differences in soil densities, whilst Cassidy and Byrne used dense sands, in the present study a loose sand was used. Moreover, the values of m_o and h_o obtained in this study correspond to yield surfaces that did not expand much further after installation. On the contrary, Byrne (2000) penetrated the caisson footings further after they were completely installed to simulate pre-loading as in jack-ups applications. Pre-loading implies higher values of V_o with which m_o and h_o are determined. However, these two reasons should be covered because V_o scales for the soil density and the shape of the yield surface is independent of its size. Therefore, a possible reason of the scatter should be sought in the caisson thickness ratio and in the mathematical formulation of the yield surface used.

The thickness ratio has a clear influence on the resulting values of m_o and h_o as observed in Figure 5.15(b) for the caisson with aspect ratio of one. Byrne (2000) did not include the tension capacity of caissons in the analysis, assuming a yield surface formulation as proposed by Butterfield and Gottardi (1994) for flat footings and also adopted by Martin (1994) for the study of spudcan footings. In the yield surface formulation presented here

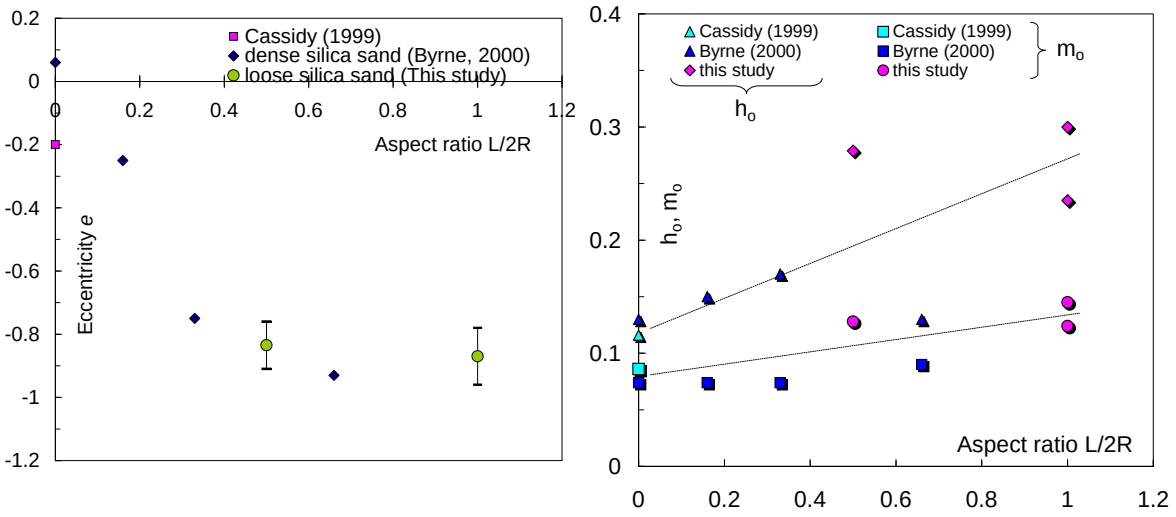

(a) Eccentricity e (b) h_o and m_o

Figure 5.15: Data with $\frac{L}{2R} = 0$ by Cassidy (1999); $\frac{L}{2R} = 0$, 0.16, 0.33 and 0.66 by Byrne (2000) and $\frac{L}{2R} = 0.5$ and 1 from this study

the parameter t_o accounts for the tension capacity.

5.4.2 Discussion

In section §5.2.1 the issue of decoupling elastic moment and elastic horizontal loads raised the existence of an elastic metacentre. A decoupling between plastic moment and plastic horizontal loads also occurs if the LRP is located at the plastic metacentre according to Houlsby (2003). Moreover, Houlsby (2003) points out that the parameters of the yield surface expression m_o, h_o and e change with the movement of the LRP. In spite of locating the LRP always at the caisson lid (see Figure 5.1) the issue of coupling is still present. The values of m_o and h_o represent a maximum of the intersection between the yield surface and the axes m and h respectively. But these intersection points are not really comparable for caissons with different aspect ratios since the eccentricity is different (Figure 5.15(a)). Consequently, load decoupling is necessary for an appropriate comparison of the data. This is achieved by eliminating the eccentricity from the yield surface expression. The expression for the location of the plastic metacentre can be derived as:

$$\frac{z_m}{2R} = -e\frac{m_o}{h_o} \tag{5.29}$$

h_{om} changes with the eccentricity as follows:

$$h_{om} = \frac{h_o}{\sqrt{1-e^2}} \tag{5.30}$$

However, m_o does not change, hence $m_{om} = m_o$ and Figure 5.15(b) still is valid. The variation of the metacentre-diameter ratio $\frac{z_m}{2R}$ with the caisson aspect ratio is shown in Figure 5.16(a). Using Cassidy's data and this study $\frac{z_m}{2R}$ increases asymptotically instead of linearly when using Byrne's data. Figure 5.16(b) shows the same h_o data presented in Figure 5.15(b) but referred to the metacentre as h_{om}. A better defined trend is found compared with the values of h_o in Figure 5.15(b), revealing that the use of a plastic metacentre improves the analysis. However, again Byrne's data follow a linear trend rather than a more asymptotic trend as the rest of the data.

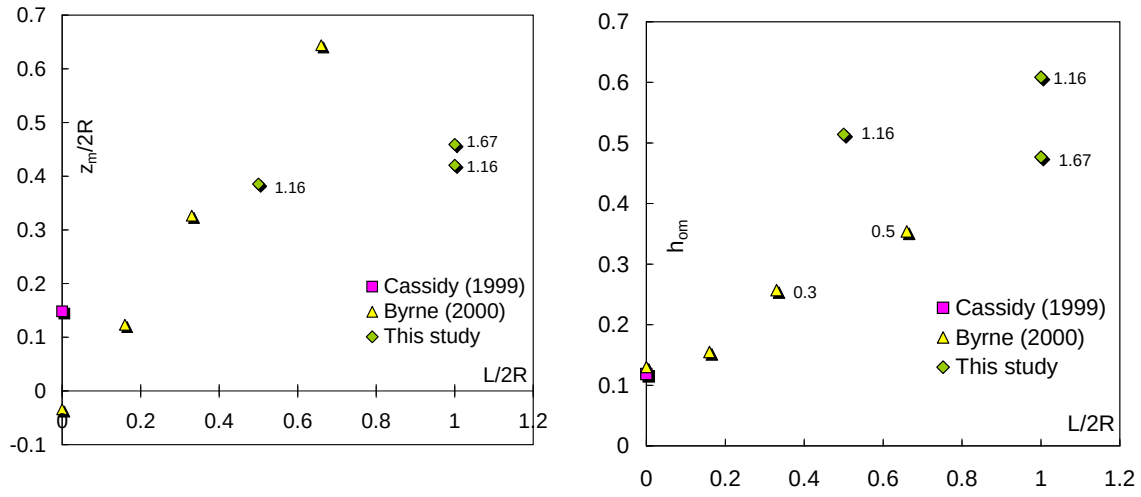

(a) Plastic metacentre (b) h_o at the metacentre $\Rightarrow h_{om}$

Figure 5.16: Data with $\frac{L}{2R} = 0$ by Cassidy (1999); $\frac{L}{2R} = 0$, 0.16, 0.33 and 0.66 by Byrne (2000), and $\frac{L}{2R} = 0.5$ and 1 by this study, showing $\frac{t}{2R}$ next to data points

5.4.3 Flow rule

The study of footing displacements is extremely important in geotechnical engineering since foundation designs are not only controlled by ultimate limit states, but also by displacements. Alternatively, stresses and loads are calculated from strains or displacements. In hyperplasticity theory as well as in classical plasticity theory the flow rule is the mathematical tool that allows modelling of incremental plastic displacements at yield. Therefore, the testing of caissons was intended to provide the information required to calibrate and validate the flow rule for hyperplasticity theory. With this objective, incremental plastic displacements at yield have been determined by subtracting the elastic components from the measured total displacements. The plastic displacement increments were obtained subtracting the measured displacements to estimated elastic displacements using equation (5.7) as follows:

$$\begin{Bmatrix} \dot{w}^p \\ \dot{\theta}^p \\ \dot{u}^p \end{Bmatrix} = \begin{Bmatrix} \dot{w} \\ \dot{\theta} \\ \dot{u} \end{Bmatrix} - \begin{bmatrix} \frac{1}{K_V} & 0 & 0 \\ 0 & \frac{K_H}{D} & -\frac{K_{MH}}{D} \\ 0 & -\frac{K_{MH}}{D} & \frac{K_M}{D} \end{bmatrix} \begin{Bmatrix} \dot{V} \\ \dot{M} \\ \dot{H} \end{Bmatrix} \tag{5.31}$$

where D is given by equation (5.8) and K_V, K_H, K_M and K_{MH} are the stiffness coefficients (see equation (5.6)), the shear modulus G is implicit in the stiffness coefficients.

The values of G adopted were firstly based on the expressions presented in section §5.2.1 and secondly slightly adjusted based on the results (initial part of the load-displacement response). Values of G between 0.5 MPa and 2 MPa were used in the calculations. The resulting magnitude of elastic displacements represented a very small proportion of the total displacements. Straight lines were fitted to determine plastic displacement increments as the ratios of $\frac{\dot{u}^p}{2R\dot{\theta}^p}$ and $\frac{\dot{w}^p}{2R\dot{\theta}^p}$. These straight lines could be fitted even in cases when the plastic displacements changed drastically from an initial positive direction to a negative direction. This occurred for negative load ratios $\frac{M}{2RH}$ between -0.5 and -0.1 (see Figure 5.5(c), although in this figure total displacements are shown, the plastic displacements do not considerably differ).

Figure 5.17 depicts the same yield surface previously shown in Figure 5.10 but with arrows on each yield point that represent the velocity vectors. They represent the incremental plastic displacement directions in the $\frac{M}{2RV_o} - \frac{H}{V_o}$ plane; only three vertical load ratios $\frac{V}{V_o}$ are shown for clarity. There are two sets of arrows, the black arrows were obtained from the experiments and the grey arrows are normal to the yield surface which represents the case of an associated flow rule.

The flow rule has been expressed by the following relationship between $2R\dot{\theta}^p$ and $\dot{u}^p$:

$$\frac{2R\dot{\theta}^p}{\dot{u}^p} = \frac{a_M h_o(m - eh)}{a_H m_o(h - em)} \tag{5.32}$$

An associated flow rule is achieved with expression (5.32) when the association factors a_M and a_H are equal. Figure 5.18 shows measured and calculated results plotted in the π plane as $\tan^{-1}\frac{\dot{u}^p}{2R\dot{\theta}^p}$ *versus* $\tan^{-1}\frac{M}{2RH}$ using $a_M = a_H$ in (5.32). Then, it is clear that an associated flow rule is able to capture the measured results in this plane. This reaffirms previous findings by other researchers. For instance, Martin (1994) confirms the hypothesis of normality to the yield surface in the $\frac{M}{2RV_o}$ - $\frac{H}{V_o}$ plane for experimental results with spudcan footings in clay. In addition, Gottardi *et al.* (1999) reveal that an associated flow rule captures adequately test results using a circular flat footing on sand. It is also

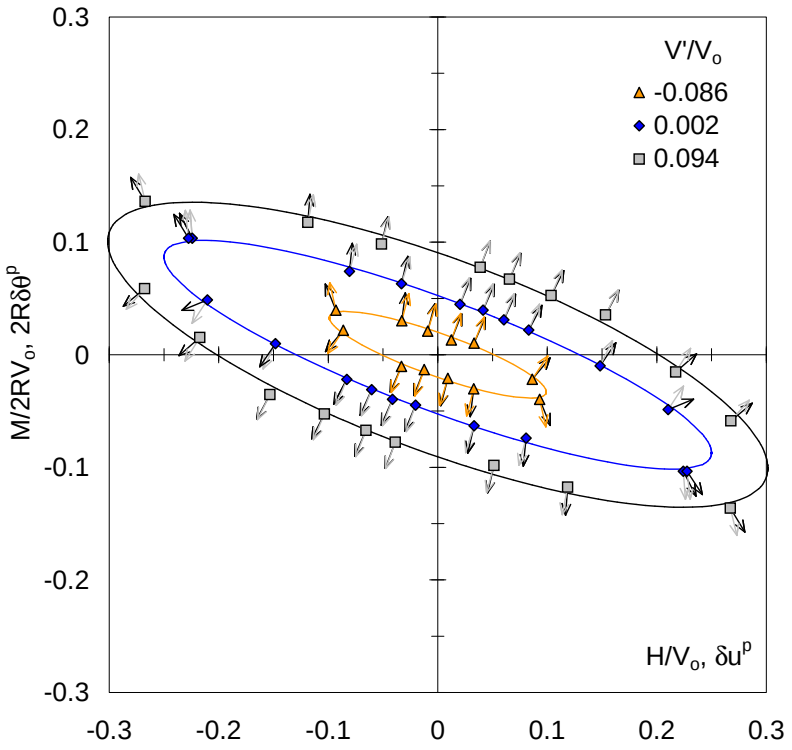

Figure 5.17: Yield points with incremental plastic displacement vectors obtained from tests (in black) and normal vectors (in grey) for caisson A (taken from Villalobos *et al.*, 2004b)

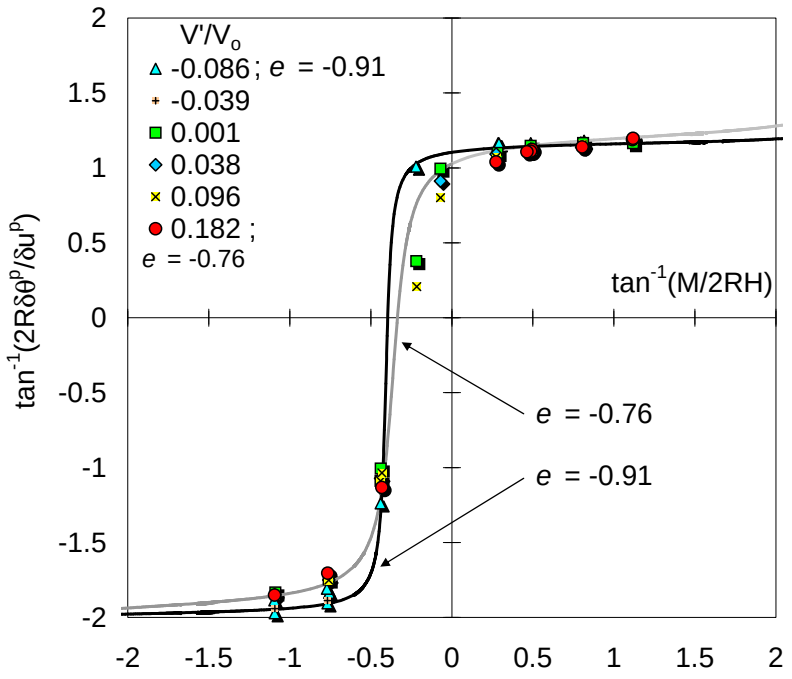

Figure 5.18: Experimental and theoretical predictions of incremental plastic displacement ratios in the π plane for caisson A

interesting to observe in Figure 5.18 the improvement of the flow rule prediction using the variation of the eccentricity for the two extreme cases of vertical load ratio.

An expression was developed to transform the measured results in terms of the ratios $\frac{\dot{u}^p}{2R\dot{\theta}^p}$ and $\frac{\dot{w}^p}{2R\dot{\theta}^p}$ into the ratio between $\dot{w}^p$ and the radial displacement increment $\dot{q}^p$ (equation (5.23)), resulting in:

$$\frac{\dot{w}^p}{\dot{q}^p} = \frac{\dot{w}^p}{2R\dot{\theta}^p}\sqrt{\frac{1-e^2}{\left(h_o\frac{\dot{u}^p}{2R\dot{\theta}^p}\right)^2 + m_o^2 + 2eh_om_o\frac{\dot{u}^p}{2R\dot{\theta}^p}}} \tag{5.33}$$

To compare the above flow rule obtained from the experiments with the theoretical flow rule, the following expression was deduced:

$$\frac{\dot{w}^p}{\dot{q}^p} = \frac{\beta_{12}\left(\nu_1+t_o\right)^{\beta_1}\left(1-\nu_2\right)^{\beta_2}\left\{\frac{\beta_2 a_{V_2}}{1-\nu_2} - \frac{\beta_1 a_{V_1}}{\nu_1+t_o}\right\}\sqrt{\frac{1}{h_o^2} + \left(\frac{1}{m_o}\frac{M}{2RH}\right)^2 - \frac{2e}{h_om_o}\frac{M}{2RH}}}{\frac{a_H}{h_o\sqrt{1-e^2}}\left(\frac{1}{h_o} - \frac{e}{m_o}\frac{M}{2RH}\right)\sqrt{h_o^2 + \left(m_o\frac{2R\dot{\theta}^p}{\dot{u}^p}\right)^2 + 2eh_om_o\frac{2R\dot{\theta}^p}{\dot{u}^p}}} \tag{5.34}$$

where the ratio $\frac{2R\dot{\theta}^p}{\dot{u}^p}$ is given by 5.32. Figure 5.19 shows measured velocity vectors in the $Q-V'$ plane for three cases of $\frac{M}{2RH}$ ratios. Strong non normality is clearly observed as the velocity vectors seem to point almost vertical and parallel to the Q axis.

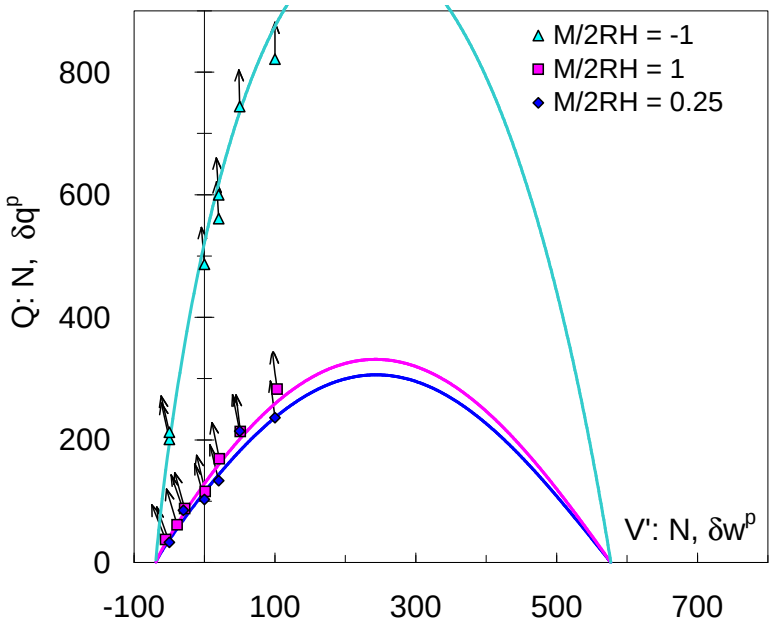

Figure 5.19: Experimental radial plastic displacement increments for three $\frac{M}{2RH}$ using caisson A

Figure 5.20 depicts the π plane $\tan^{-1}\frac{\dot{w}^p}{\dot{q}^p}$ - $\frac{V'}{V_o}$ including the experimental results using expression 5.33 and theoretical curves obtained with equation (5.34). Five set of association factors were used to represent the data. In general the data follow a similar trend

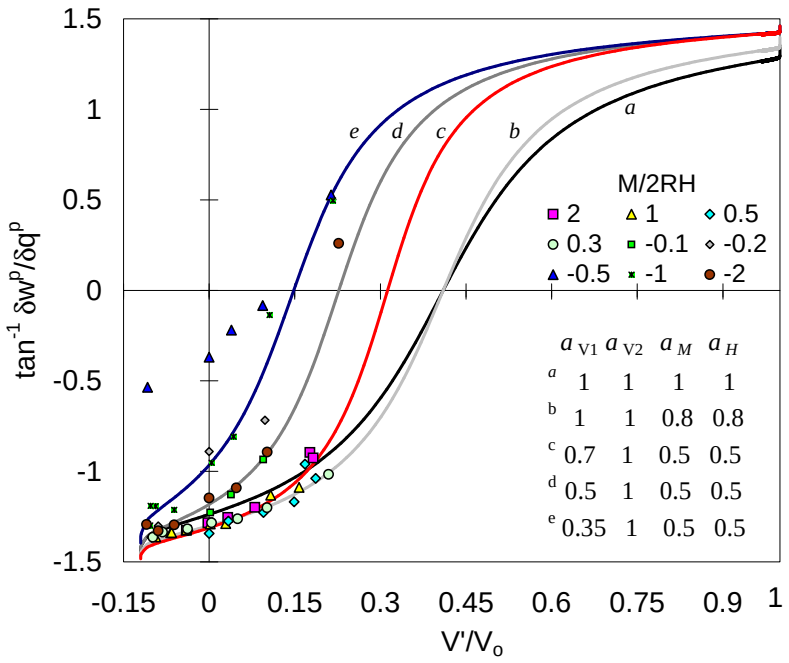

Figure 5.20: Experimental and theoretical predictions of incremental plastic displacement ratios in the π plane with variation of the association factors for caisson A

for positive load ratios which reflects a constant decreasing of the caisson uplift with $\frac{V'}{V_o}$, deviating for negative load ratios where a drastic reduction in uplift and even caisson settlement occur. An associated flow rule is obtained when $a_{V_1} = a_{V_2} = 1$. Figure 5.20 also shows that a non-associated flow rule is obtained with variations of a_{V_1} below unity, in this case, whilst keeping $a_{V_2} = 1$. The association factor $a_{V_2} = 1$ is a compromise due to the lack of results from this study for high vertical loads. In order to determine caisson response with accuracy it is necessary to carry out a parametric study to evaluate which set of association factors provides the best prediction.

5.4.4 Validation

An assessment of the hyperplastic model using the parameters already obtained is necessary to evaluate the performance of the model against experimental results. The simple case of a single yield surface and isotropic hardening is used for an initial validation. Test FV1_1_2A was chosen and the soil properties and test parameters for this test are summarised in Tables 4.1 and 5.1. Additionally, the following parameters as previously determined (Table 5.6) were used: $m_o = 0.279$, $h_o = 0.128$, e = -0.84 and $t_o = 0.12$. The chosen sets of association factors were those of b and c shown in Figure 5.20, where the

only constraint was that a_M and a_H should be equal to give an associative flow rule in the $M - H$ plane.

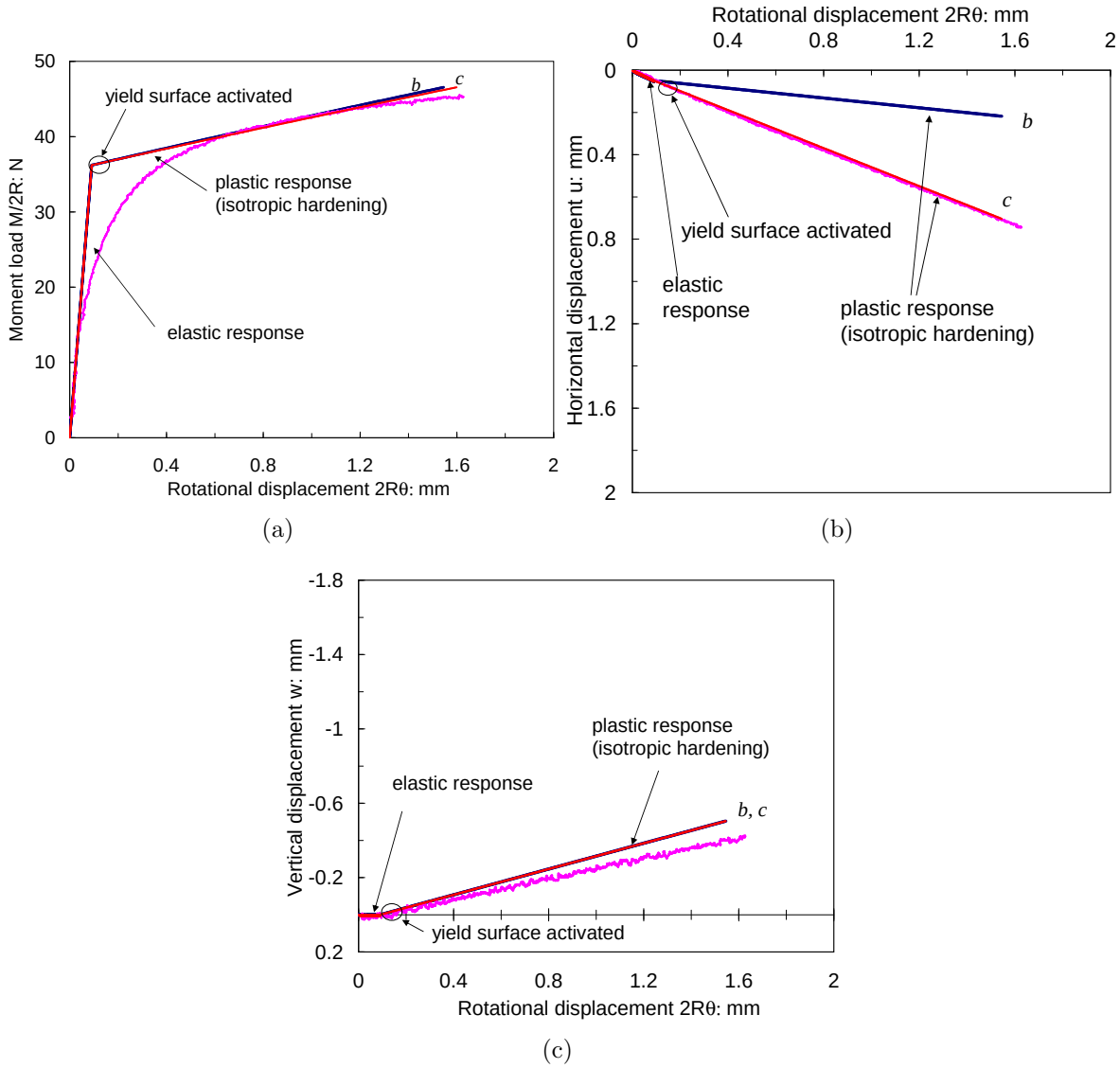

Figure 5.21: Measured and calculated response for caisson A under the load ratio $\frac{M}{2RH} = 1$ at constant vertical load $V' = 50$ N

An elastic shear modulus $G = 1$ MPa was used in the calculations. Figure 5.21(a) shows the measured and calculated $\frac{M}{2R} - 2R\theta$ response, noting immediately the poor modelling of the transition between 'elastic' and 'fully plastic' response. Initially the load path proceeds inside the yield surface resulting in a pure elastic response until the yield surface is reached. Then, yield occurs and further increase in the moment load causes the expansion of the yield surface. There is a good prediction of the measured vertical displacement w as shown in Figure 5.21(c), although it is slightly overestimated. However, Figure 5.21(b) shows that the theory gives a better prediction of the measured horizontal displacement

u using the set of association factors c instead of b (Figure 5.20). It is worth mentioning that the theoretical calculations are more sensitive to the association factors than any other parameter. Moreover, the parameter selection does not follow the sequence and magnitudes proposed by Nguyen-Sy (2006) following the results from Model B and Model C, where $a_{V1} = 0.297$, $a_H = a_M = 0.7$, and $a_{V2} = 1$. This selection of association factors for flat footings and spudcan footings in sand and clay follows the sequence: $0 < a_{V1} \leq a_H, a_M \leq a_{V2} \leq 1$. Whilst a value of $a_{V1} > a_H, a_M$ was used in the previous example. From this particular example, caisson foundations seem to deviate from the pattern of association factors for spudcan and flat footings.

5.5 CYCLIC COMBINED LOADING TESTS

5.5.1 Introduction

The cyclic nature of the maritime and environmental loadings was pointed out in Chapter 1. For this reason, an important issue in this investigation was to study the response of caisson footings under repeated loading. The purpose of the experiments was not to reproduce exactly the offshore cyclic loadings during storm events, but to identify important patterns of foundation behaviour that contribute towards modelling and design. In particular, it has been demonstrated that the hyperplasticity theory is suitable to modelling the cyclic behaviour of soils (Puzrin and Houlsby, 2001; Einav, 2005; Nguyen-Sy, 2006).

In practical terms, cyclic moment loading tests can be seen as a continuation of monotonic tests, where instead of applying a one-directional rotation or translation, several rotations of increasing amplitude are applied by simultaneously switching the direction. Byrne (2000) concludes that no major differences exist between monotonic and cyclic tests in terms of $\frac{M}{2R} - 2R\theta$ response (using smaller model caissons in a very dense oil-saturated Baskarp cyclone sand). Furthermore, no rate effect was found even though monotonic tests were performed at a much slower rate than the cyclic tests. However, there was not

a clear conclusion about the vertical displacements caused by cyclic loading. In addition, symmetrical loading tests were mostly preformed, whilst the environmental forces normally have a predominant direction. It was important to explore loading cases where the rotational displacements are not completely recovered.

A series of 45 combined loading tests were performed in the laboratory for the investigation of cyclic response of caisson foundations. Test information is summarized in Tables 5.7 and 5.8, where the minimum moment load $\frac{M_{min}}{2R}$ was obtained in the first cycle, whereas the maximum $\frac{M_{max}}{2R}$ in the tenth cycle (otherwise indicated). The net or total vertical displacement during each test is w_t, where a negative value corresponds to upward movement and positive to settlement. In the majority of the tests caissons were

Table 5.7: Summary of cyclic tests undertaken using caisson A

Test	V' N	$\frac{V'}{\gamma_d(2R)^3}$	V_o N	R_d %	γ_d kN/m^3	$\frac{M}{2RH}$	$\frac{M_{min}}{2R}$ N	$\frac{M_{max}}{2R}$† N	w_t mm
FV127_23_3	-30	-0.08	550	18	15.10	1	5, -6	18^{9}, -19	-16.8
FV108_21_3	3	0.01	483	12	14.96	2	18, -15	36^{8}, -36	-6.3
FV78_13_2	4	0.01	750	41	15.73	1	15, -17	38^{6}, -36^{7}	-7.6
FV81_14_3	4	0.01	726	46	15.85	0.5	23, -8	31^{5}, -28^{7}	-8.2
FV85_15_3	4	0.01	783	50	15.99	0.25	18, -8	24^{6}, -21^{6}	-9
FV86_16_3	2	0.01	458	18	15.11	0.25	16, -8	18^{6}, -18	-7.8
FV111_22_3	3	0.01	557	23	15.23	-0.1	-2, 1	10, -10	-2.6
FV113_22_3	6	0.02	530	23	15.23	-0.25	5, -8	44, -47	-0.3
FV73_12_2	31	0.08	830	46	15.87	1	22, -22	54, -52	-2.8
FV82_14_3	27	0.07	784	46	15.85	0.5	24, -7	40^{9}, -36	-4
FV87_16_3	19	0.05	461	18	15.11	0.25	17, -8	22^{8}, -21	-4
FV90_17_3	13	0.03	463	15	15.03	-2	17, -14	66, -60	-2.5
FV79_13_2	54	0.14	730	41	15.73	1	22, -21	56, -57	-1.7
FV83_14_3	51	0.13	730	46	15.85	0.5	31, -6	46, -44	-1.5
FV88_16_3	59	0.15	503	18	15.11	0.25	23, -9	31, -30	-1
FV77_13_2	43	0.11	906	41	15.73	-1	10, -10	123, -114	-0.3
FV80_13_2	110	0.28	821	41	15.73	1	30, -26	73, -72	-0.2
FV84_14_3	101	0.25	795	46	15.85	0.5	25, -9	58, -56	0.1
FV89_16_3	100	0.26	478	18	15.11	0.25	25, -8	36, -36	0.8
FV109_21_3	193	0.51	487	12	14.96	2	24, -39	89, -90	3.2
FV104_20_3	182	0.48	480	12	14.95	1	26, -21	77, -76	3.2
FV107_21_3	185	0.49	460	12	14.96	0.25	23, -19	45, -45	3.4
FV105_20_3	283	0.75	480	12	14.95	1	22, -25	92, -93	3.6
FV106_21_3	385	1.02	460	12	14.96	0.5	26, -29	88, -89	4.2
FV130_24_3	2	0.00	582	21	15.17	1	20	41	-1.3
FV132_24_3	3	0.01	513	21	15.17	1	16	38	-1.4
FV121_23_3	11	0.03	521	18	15.10	0.25	17	22^{7}	-2.9
FV123_23_3	9	0.02	534	18	15.10	0.25	8, -8	23^{13}, -22^{17}	-10
FV125_23_3	17	0.04	560	18	15.10	0.25	17, -15	26^{15}, -26^{15}	-7.7
FV136_24_3	11	0.03	540	21	15.17	-0.5	-35	-151	-0.05
FV134_24_3	47	0.12	528	21	15.17	-0.25	-19	-66	-0.2

†numbers up indicate cycle at which M_{max} was reached

Table 5.8: Summary of cyclic tests undertaken using caisson B

Test	V' N	$\frac{V'}{\gamma_d(2R)^3}$	V_o N	R_d %	γ_d kN/m^3	$\frac{M}{2RH}$	$\frac{M_{min}}{2R}$ N	$\frac{M_{max}}{2R}$ N	w_t mm
FV124_23_3	-2	-0.02	467	18	15.10	2	19, -38	65, -68	-4.9
FV102_20_3	3	0.02	428	12	14.95	1	26, -25	59, -55	-5
FV120_23_3	-1	-0.01	421	18	15.10	0.5	24, -16	36, -38	-6.2
FV128_23_2	6	0.05	540	18	15.10	0.25	12, -15	28, -29	-5.7
FV110_22_3	0	0.00	443	23	15.23	-0.1	-1, 1	-6, 6	-2
FV112_22_3	-3	-0.03	433	23	15.23	-0.25	-7, 4	-24, 24	-1.9
FV115_22_2	19	0.15	600	23	15.23	1	27, -31	64, -63	-2.3
FV117_22_3	46	0.36	469	23	15.23	1	34, -24	62, -65	0.6
FV126_23_3	95	0.75	459	18	15.10	2	43, -33	89, -88	2.9
FV119_22_3	85	0.67	557	23	15.23	1	35, -33	75, -76	1.6
FV122_23_3	89	0.70	443	18	15.10	0.5	27, -27	56, -53	1.9
FV133_24_3	20	0.16	467	21	15.17	-0.25	-15.8	-31.4	-1.2
FV135_24_3	17	0.13	470	21	15.17	-0.5	-34.4	-113.7	-0.7
FV129_24_3	48	0.37	465	21	15.17	1	30, -19	73, -64	0.1

rotated symmetrically with respect to the centre of the caisson. A preliminary analysis of these experiments was carried out by Villalobos (2004). However, a few tests shown at the bottom of Tables 5.7 and 5.8 were not symmetrically rotated, also referred to as one-way cyclic loading tests. The whole series of tests is reported by Villalobos *et al.* (2004a). This section presents representative tests and draws relevant conclusions from the analysis of all the tests.

5.5.2 Cyclic moment-rotation response

A computer controlled *VMH* loading rig was used to carry out the testing, using caissons A and B and a dry, loose, white Leighton Buzzard sand (see Chapter 2 for details). Tests were conducted holding a low vertical load whilst a cyclic rotational or lateral displacement of increasing amplitude was applied until a maximum displacement. In this section it is not intended to reproduce a loading path resembling field conditions, but to find foundation response patterns which can be incorporated in the modelling.

Figure 5.22(a) shows a test with ten rotational cycles applied to caisson A at a rate of $2R\dot{\theta} = 0.02$ mm/s. The same test is shown in Figure 5.22(b), but in a $H - u$ plot, where it is observed that u increases less than $2R\theta$ in each cycle. Figures 5.23(a) and 5.23(b) shows another test with ten rotational cycles, but applied to caisson B; in this

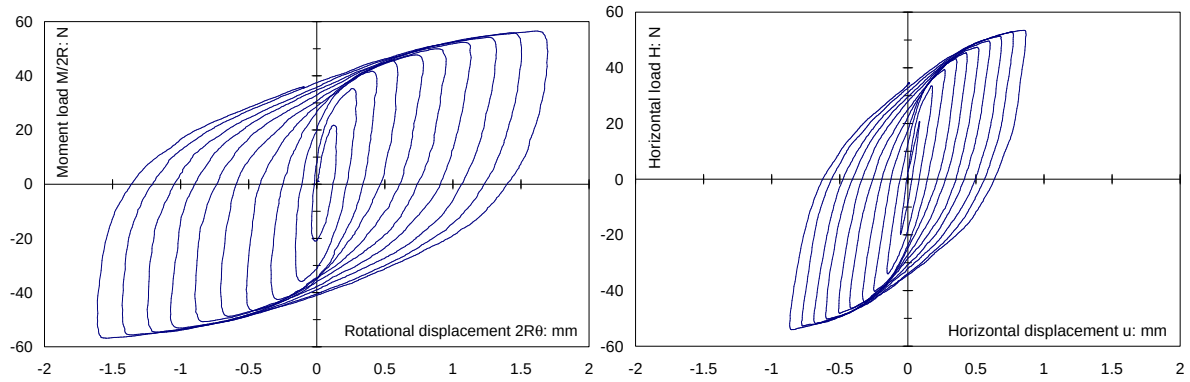

(a) Test FV79_13_2A (b) Test FV79_13_2A

Figure 5.22: Cyclic rotational response under constant vertical load $V' = 54$ N at $\frac{M}{2RH} = 1$

case u is similar to $2R\theta$. As a consequence, a larger area is enclosed by the cycle loops. Another important feature of these results is that the response is hysteretic and stiffness degradation during each cycle is observed.

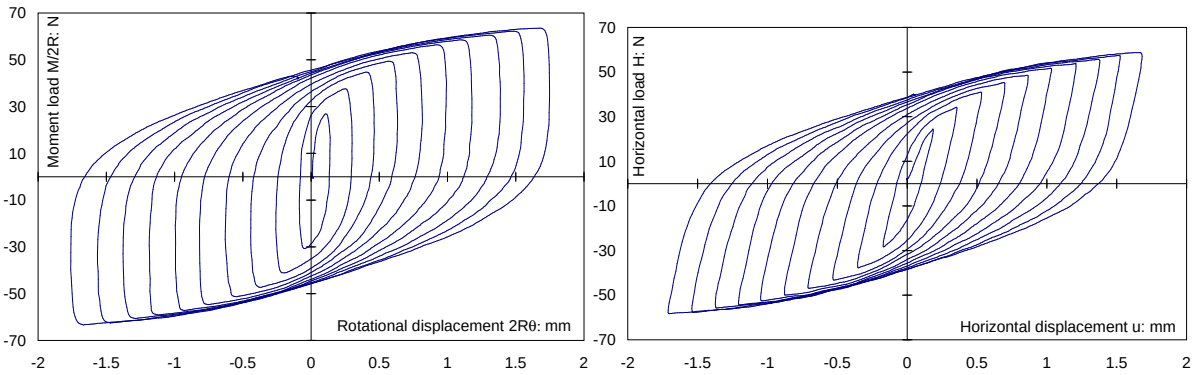

(a) Test FV115_22_2B (b) Test FV115_22_2B

Figure 5.23: Cyclic rotational response under constant vertical load $V' = 19$ N at $\frac{M}{2RH} = 1$

Hysteresis is a phenomenon observed in soils that experience cyclic loading. Therefore, a foundation cyclically loaded naturally manifests this phenomenon. In a load-displacement curve hysteresis is recognised as loops where the loading and unloading curves do not coincide, albeit sharing the points of load reversal. Masing (1926) indicated that the property of pure kinematic hardening allows the prediction of unloading and reloading response once the initial loading curve is known. The first Masing rule states that the tangent slope of the reloading curves is identical to the tangent slope of the initial curve. The second Masing rule states that the shape of unloading and reloading curves is the same as that of the doubled initial curve. Figure 5.24 confirms that the first and second Masing rule (for test FV79_13_2A) are obeyed.

To compare different cyclic loading tests peak load values and displacements at peak in each cycle were obtained as shown in Figure 5.25. Knowledge of these peak values allows a 'backbone' curve to be defined, which is used in modelling to generate cyclic loops. The importance of obeying the Masing rules has favourable modelling implication since knowing the initial loading any subsequent unloading-reloading can be reproduced. In addition, the backbone curve can be reproduced symmetrically during positive and negative loads. Figure 5.25 shows that experimentally symmetry is fairly achieved.

The minimum and maximum 'peak' moment capacity listed in Tables 5.7 and 5.8 are normalised and plotted in Figures 5.26(a) and 5.26(b) as functions of the normalised vertical load and the load ratio. It is clear that independent of the load ratio the maximum moment capacity increases with the vertical load. However, the increase of the minimum moment capacity obtained in the first cycle with the vertical load is less pronounced and reach a threshold. These figures show only results from positive load ratios, the few data for negative load ratios showed lower values of minimum peak moment capacity and higher maximum peak moment capacity. Moreover, higher moment capacity was obtained for the caisson with aspect ratio of one. Therefore, the normalised moment should include the aspect ratio (or skirt length L) to compare results from different caissons.

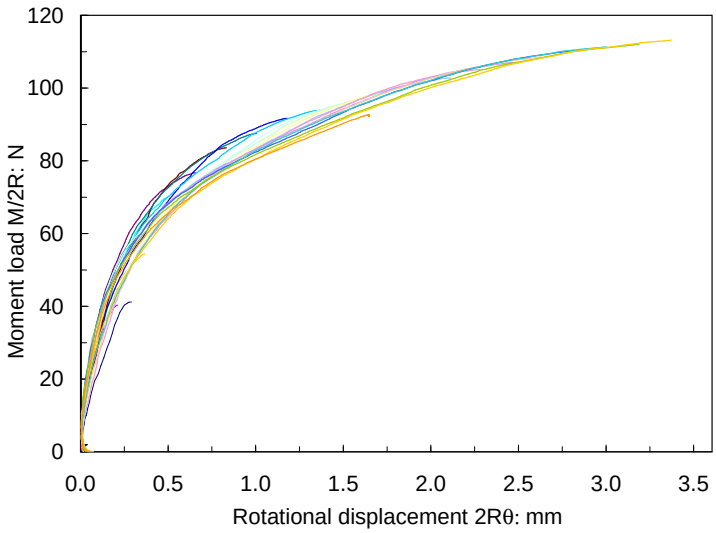

Figure 5.24: Proof of the first and second Masing rule (test FV79_13_2A)

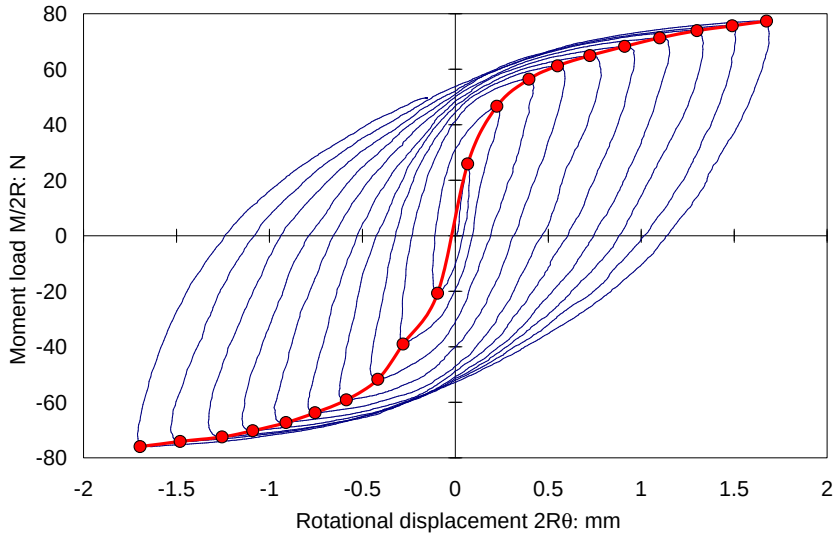

Figure 5.25: Backbone curve of test FV104_20_2A showing peak points

Tests with increasing constant vertical loads from -50 N to 200 N, for a loading ratio $\frac{M}{2RH}$ = 1 are shown in Figure 5.27(a) as the dimensionless quantity $\frac{M}{\gamma_d(2R)^4}$ and θ in radians. There is an asymptotic moment resistance at the end of the tests with V' = -50 N and 0 N. On the other hand, the remainder of the tests show an increase in their moment resistance after each cycle. For clarity only two monotonic tests have been plotted together with the cyclic tests for comparison. Byrne's (2000) conclusion is confirmed since no great difference is observed between monotonic and cyclic curves. This is not very surprising since the test history is identical, *i.e.* a series of cycles with monotonically increasing

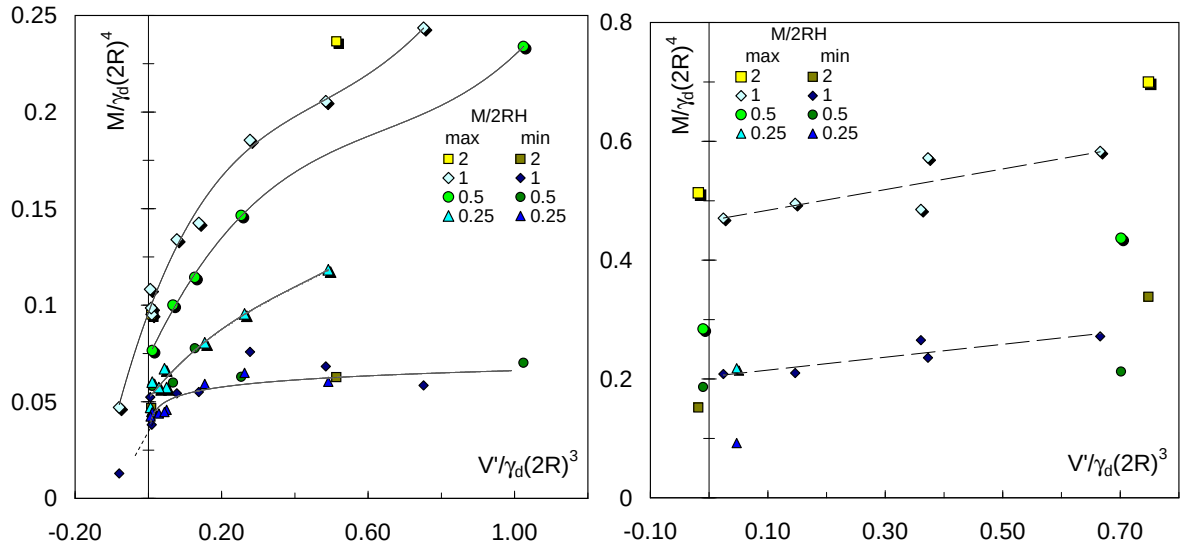

(a) Caisson A, $\frac{L}{2R} = 0.5$ (b) Caisson B, $\frac{L}{2R} = 1$

Figure 5.26: Variation of the normalised moment capacity (minimum and maximum peaks) with the normalised vertical load and with the load ratio

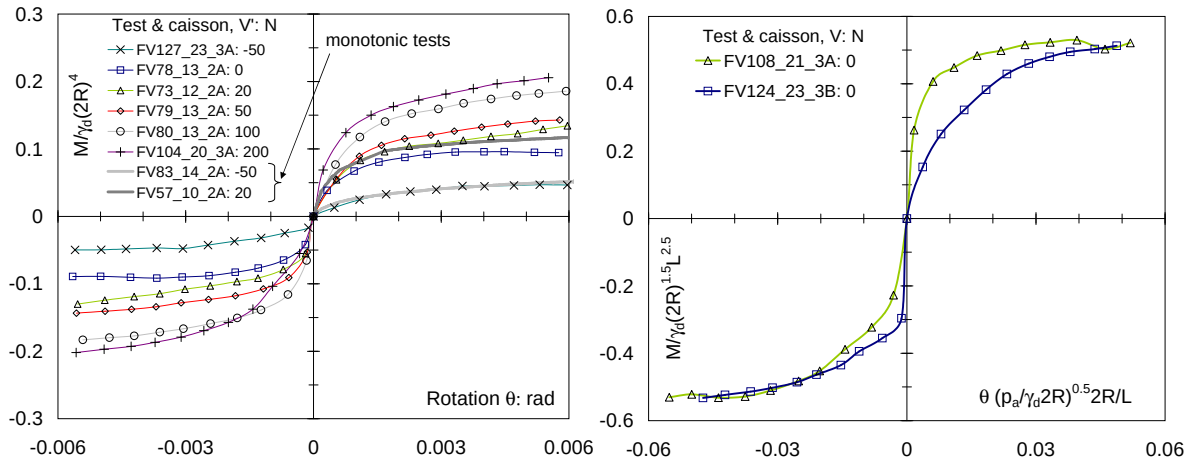

(a) Caisson A, $\frac{L}{2R} = 0.5$ under $\frac{M}{2RH} = 1$ (b) Caisson A and B, $V' = 0$ N and $\frac{M}{2RH} = 2$

Figure 5.27: Peaks of cyclic moment load versus rotational displacement comparing (a) different constant vertical loads. Note the presence of two monotonic tests, and (b) curves from caissons A and B

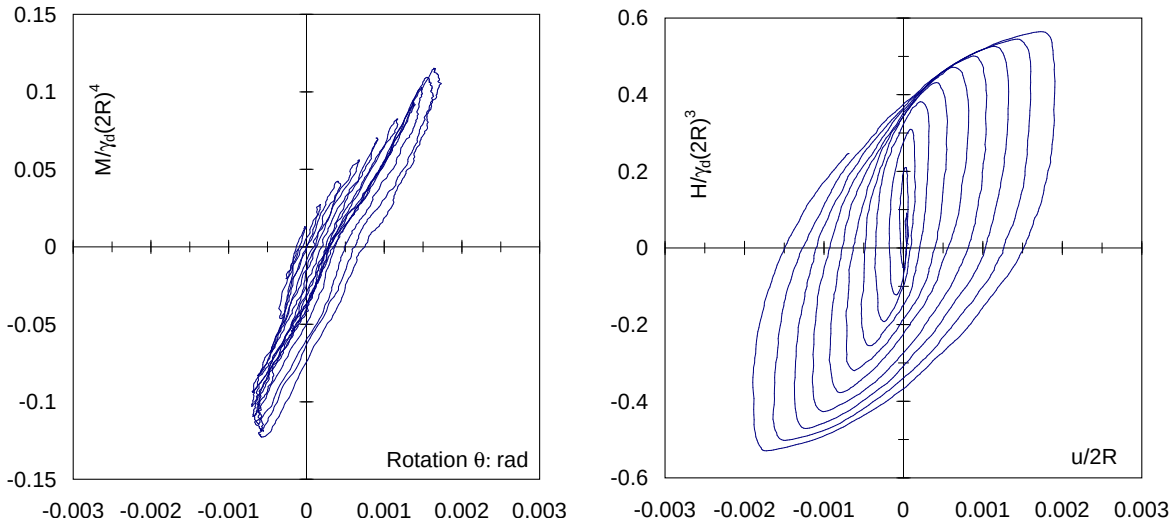

(a) Normalised moment-rotation (b) Normalised horizontal load-displacement

Figure 5.28: Test FV113_22_3A cycled under $\frac{M}{2RH}$ = -0.25 and $V' = 6$ N

amplitude, such that virgin soil is always yielding at the end of a new loading or reverse cycle. Therefore, it is not surprising that the peaks fall close to the backbone curve for a single one-way rotation. Furthermore, an even more relevant conclusion for caisson design is the favourable effect of the increase of V' on the caisson moment capacity. Figure 5.27(b) compares the cyclic response of caissons with different aspect ratios. The scaling expressions used and shown in the figure were found to better capture the effect of the skirt length. Strictly, in section §5.1 the moment was found to be a function of L^3, but in view of the experimental results a better agreement was achieved scaling by $L^{2.5}$ instead.

Differences appear at the beginning of the cyclic tests and more significant to the right hand side mostly due to disturbance of the sand sample by a previous monotonic tests. But in the left hand side a better agreement is found.

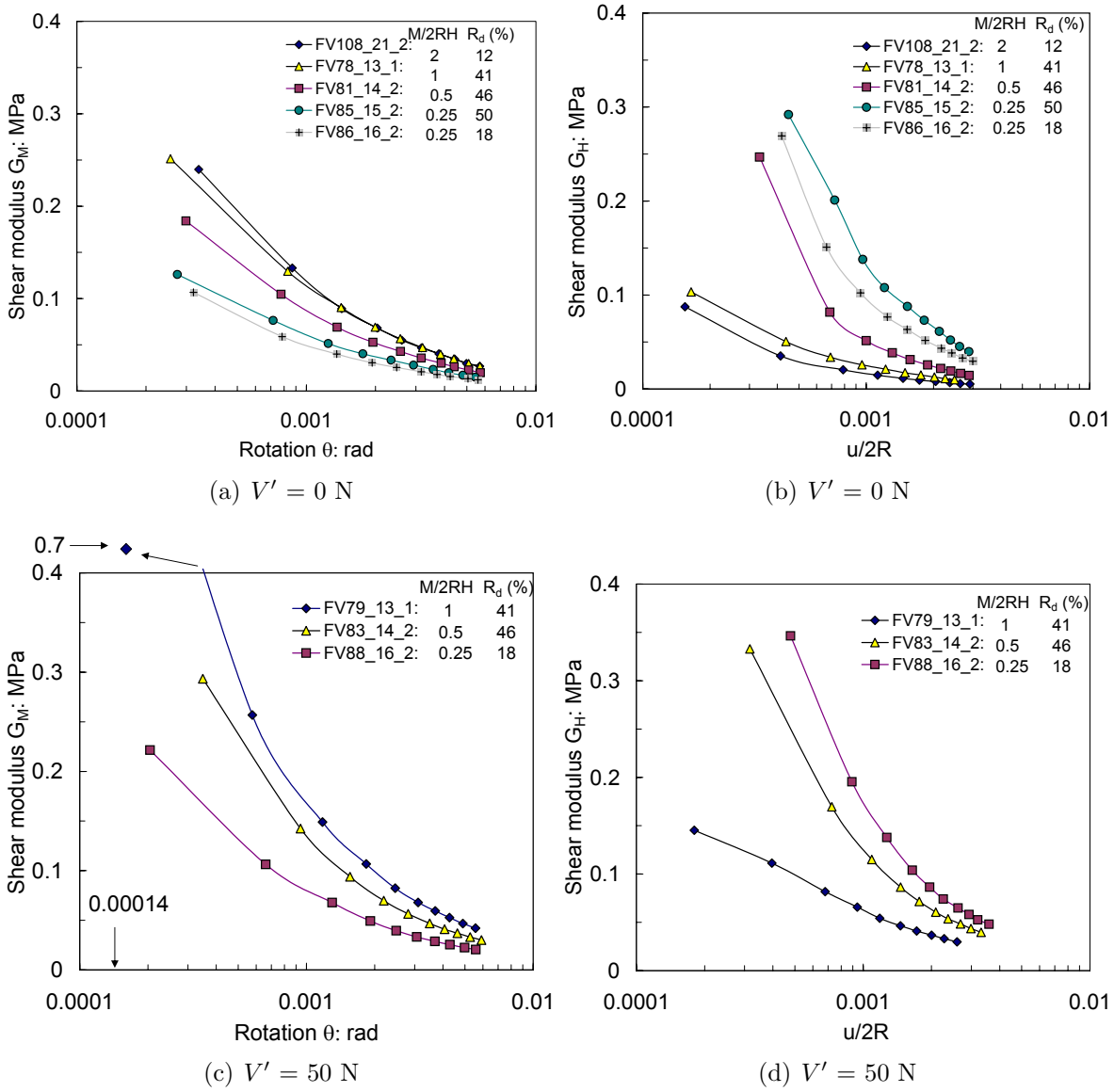

(a) $V' = 0$ N (b) $V' = 0$ N

(c) $V' = 50$ N (d) $V' = 50$ N

Figure 5.29: Secant shear modulus variation with rotation and horizontal displacement

Figure 5.28(a) shows a lateral cyclic tests with a much higher horizontal load than moment load as well as having opposite directions. Under these conditions no open loops were developed during cycling. However, the $H - u$ response possesses hysteresis as it can be observed in Figure 5.28(b).

The degradation of the foundation stiffness is caused by the appearance of plastic displacement. From soil dynamics studies the variation of shear stiffness with the shear

strain is well known. However, the curves found in the technical literature are not directly applicable to problems of soil-footing interaction. The values of G were obtained using equations (5.5) and (5.6), where G can be expressed as a function of the caisson radius, moment and horizontal load, rotation and horizontal displacement and dimensionless stiffness coefficients. Two expressions for G can be deduced, one depending on the moment and the other depending on the horizontal load. Since a secant modulus was calculated peak loads and the corresponding displacements were taken as shown in Figure 5.25. Figures 5.29(a) and (c) are examples of secant shear moduli G obtained from cyclic $\frac{M}{2R} - 2R\theta$ curves as a function of the footing rotation. Figures 5.29(b) and (d) show secant shear moduli G obtained from cyclic $H - u$ curves as a function of the normalised lateral displacement $\frac{u}{2R}$. These figures show clearly the reduction of the secant shear modulus after each cycle. The initial plateau well known in soil dynamics to appear for very small deformations corresponds to the elastic G. However, larger values of G were not captured from the measurements. Values of G that correspond to elastic response were estimated as between 0.5 MPa and 2 MPa.

5.5.3 Non-symmetric moment loading tests

The symmetry in the loading regime is an idealization that assists as a starting point in the calibration and validation of numerical models. Moreover, the offshore loading regime is not symmetric and loads are more likely to be predominant in one direction. Tests were performed to generate non-symmetrical cyclic response instead of applying symmetrical rotations or lateral displacements (by adding to the current unloading-reloading rotations the previous unloading-reloading rotations plus the initial rotation). Figure 5.30(a) compares the response of a non-symmetric test with a symmetric test. Peaks of both tests follow a similar trend, at least until both curves are comparable. In addition, the tenth cycle loop of the symmetrical test is overlapped exactly at the tenth cycle of the non-symmetrical test. Both tenth cycle loops coincide in the unloading, but not in the reloading where they are close each other in the initial part, albeit they differ at the end of the reloading. The fact that rotation after $2R\theta = 1.6$ mm is not experienced by the

symmetrical test influences the response in reloading but not in unloading.

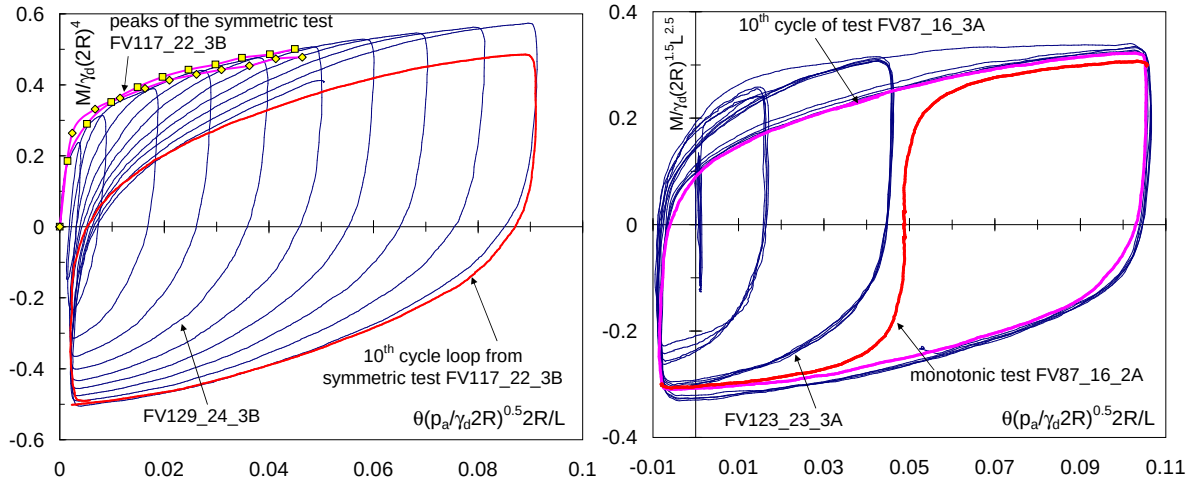

(a) $\frac{L}{2R} = 1$, $\frac{M}{2RH} = 1$ and $V' = 50$ N (b) $\frac{L}{2R} = 0.5$, $\frac{M}{2RH} = 1$ and $V' = 19$ N

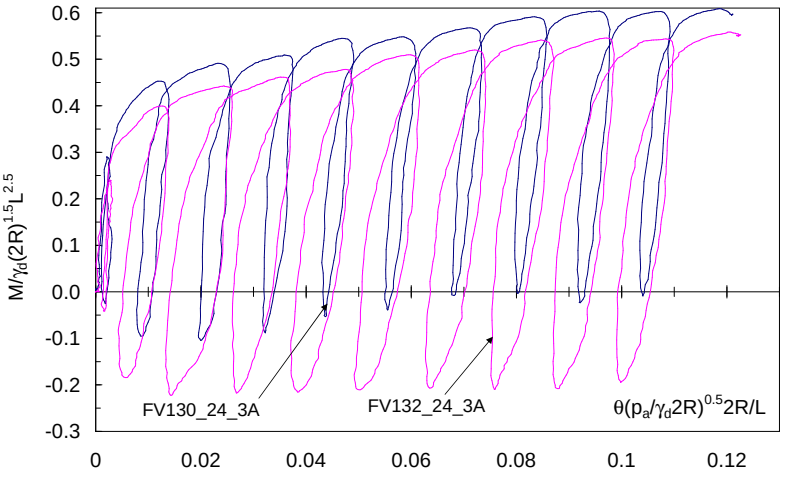

(c) $\frac{L}{2R} = 0.5$, $\frac{M}{2RH} = 1$ and $V' = 2$ N

Figure 5.30: (a) Non-symmetric test FV129_24_3B comparing with peaks and tenth cycle loop of symmetric test FV117_22_3B, (b) non-symmetric 17 cycles test FV123_23_3A comparing with tenth cycle loop of symmetric test FV87_16_3A and with monotonic test FV87_16_2A, and (c) one-way cyclic loading tests FV130_24_3A and FV132_24_3A

A 17 cycles test (in groups of 3, 4, 5 and 5 cycles) was performed to investigate the effect of repeating cycles under the same amplitude. Figure 5.30(b) shows that no significant difference in the load-displacement response is found in cycles with the same amplitude. Moreover, Figure 5.30(b) compares this test with another two tests under similar conditions, but different loading regimes. Test FV87_16_2A corresponds to monotonic loading and test FV87_16_3A to symmetric cyclic loading. To compare the last five cycles of the non-symmetric test with the tenth cycle of the symmetric test and the monotonic test the curves were overlapped and for the latter the negative moment load replicated. The

monotonic test can be used as backbone curve not only for a symmetric cyclic response, but also for the non-symmetric cyclic response.

Figure 5.30(c) illustrates the case of unloading to a constant rotation smaller than the next reloading rotation. As a consequence the caisson tilts steadily after each cycle without passing through the origin as shown in Figures 5.30(a) and 5.30(b). Two tests are shown in Figure 5.30(c), the unloading rotation magnitude being the only difference. As a result of the shorter rotation amplitude the caisson moment capacity is higher than that shown in Figure 5.30(b), and compares fairly well with the results shown in Figure 5.30(a). A monopod caisson foundation of an offshore wind turbine is more likely to be under this type of loading regime. Therefore, if a caisson undergoes a series of extreme events as the last nine cycles shown in Figure 5.30(c) large irrecoverable rotations should be expected. It is important then to avoid this detrimental irrecoverable deformation of the foundation. To this end, the caisson foundation response should not occur beyond the first cycle shown in Figure 5.30(c). To ensure this the caisson design should restrict any reduction of foundation stiffness that could cause large irrecoverable rotations.

5.5.4 Cyclic vertical displacement response

In the above section it has been demonstrated that the moment capacity of a caisson is independent of the loading regime for similar rotation amplitudes for a small number of cycles, *e.g.* 10 cycles. Kelly *et al.* (2006) scale the cyclic moment load and rotational displacement response to compare results from displacement controlled laboratory tests and load controlled field trials. However, Byrne (2000) and Kelly *et al.* (2006) do not show the effect of monotonic and cyclic loading on the vertical displacement response.

The total vertical displacement w_t listed in Tables 5.7 and 5.8 is plotted in Figures 5.31(a) and 5.31(b) as a function of the normalised vertical load $\frac{V'}{V_o}$ and the load ratio $\frac{M}{2RH}$. It can be observed clearly a transition of the caisson movement from upward to downward. The change from uplift to settlement occurs at $\frac{V'}{V_o} = 0.13$ for caisson A and at 0.10 for

caisson B. For the normalisation $\frac{V'}{\gamma_d(2R)^3}$ the transition was found to be at 0.25 and at 0.35 respectively. The values of 0.13 and 0.1 are lower than those extrapolated from the monotonic moment tests ($\frac{V'}{V_o} \approx 0.3$, see Figure 5.20). The implication of this transition are discussed in the following with examples of test results.

Figure 5.32 shows the evolution of the vertical displacement w with the rotational displacement $2R\theta$ for three tests with similar characteristics, but performed under different vertical loads V' (20 N, 100 N and 200 N). For the test under $V' = 20$ N the caisson's upward movement is steady with negligible recovery. The final uplift of caisson A monotonically rotated (test FV27_3_2A) was less than 0.8 mm (see Figure 5.3(d)). Whilst the total uplift of caisson A cyclically rotated under $V' = 20$ N shown in Figure 5.32 is almost 3 mm. This reveals that the caisson upward movement obtained in a monotonic loading can be totally different from that obtained in a cyclic loading.

From Tables 5.1 and 5.2 test FV31_4_2A had a final uplift under $V' = 100$ N of $w_f \approx \frac{\delta w^p}{2R\delta\theta^p} \cdot 2R\theta_f$ = -0.25 · 1.65 = -0.4 mm. This compares very well with the final uplift observed in Figure 5.32 for the test under $V' = 100$ N. After an initial small uplift the caisson rocks following the same trajectory in each cycle returning always to the same

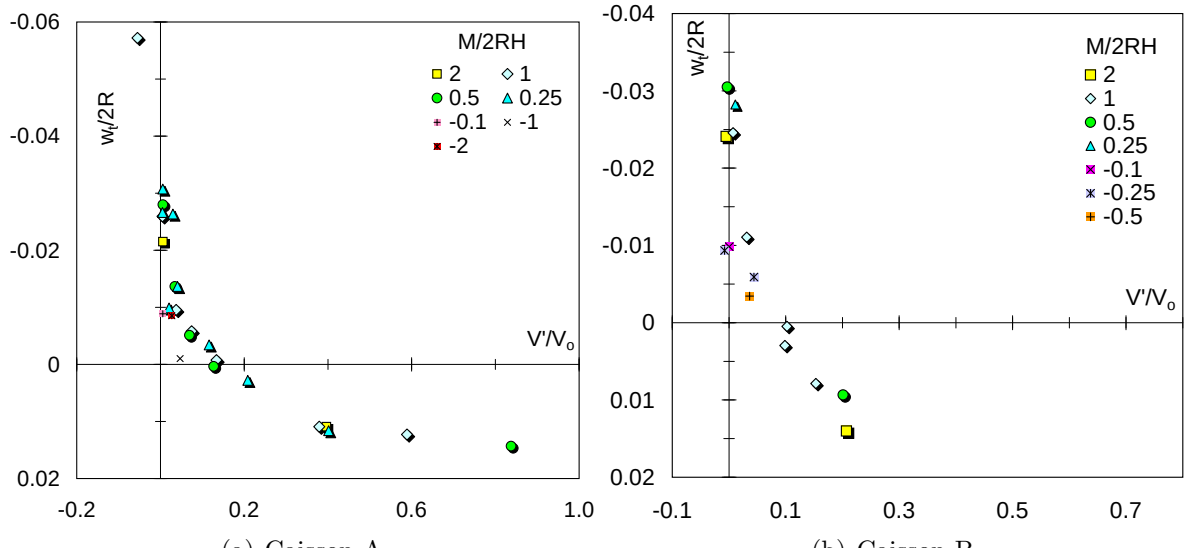

(a) Caisson A (b) Caisson B

Figure 5.31: Variation of the total vertical displacement with the normalised vertical load $\frac{V'}{V_o}$ and load ratio $\frac{M}{2RH}$

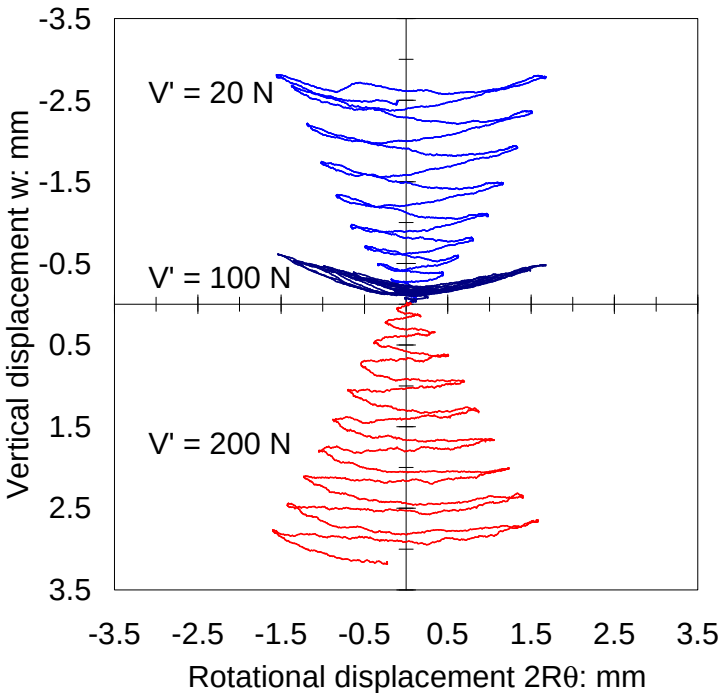

Figure 5.32: Ten cycles tests under $\frac{M}{2RH} = 1$. Test FV73_12_2A, $V' = 20$ N; test FV80_13_2A, $V' = 100$ N; test FV104_20_3A, $V' = 200$ N

point in the center. This absence of net vertical movement after each cycle has important implications in modelling, since it gives evidence of the parallel point. The parallel point derives its name from the fact that a velocity vector located in the parallel point has no vertical displacement component, therefore the velocity vector becomes parallel to the deviatoric load or radial displacement axis. Due to the zero increment of the plastic vertical displacement the yield surface size does not change. Furthermore, the parallel point establishes the boundary between heave and settlement of the footing (Cassidy, 1999), and the loading regime does not influence the caisson vertical movement response.

The third test carried out under $V' = 200$ N shows the steady settlement of the caisson during each cycle. Although no monotonic test was performed at $V' = 200$ N, it is believed that the final w will not reach more than a 1 mm if the slope of the first cycle shown in Figure 5.32 were followed. The effect of V' on the development of heave or settlement is also illustrated in Figure 5.33(a), where the w values correspond to reversals coinciding with the peak moment loads (Villalobos, 2004). Figure 5.33(b) shows that for caisson B the parallel point is located at a vertical load of about 50 N (test FV129_24_3B,

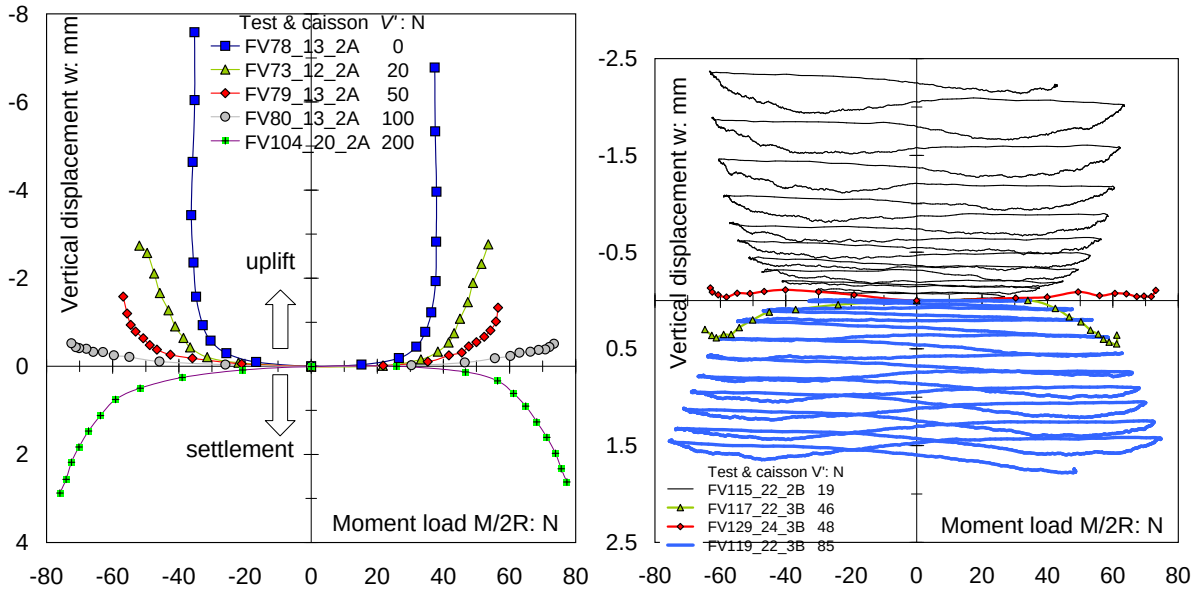

(a) Caisson A, $\frac{L}{2R} = 0.5$, $\frac{M}{2RH} = 1$ (b) Caisson B, $\frac{L}{2R} = 1$, $\frac{M}{2RH} = 1$

Figure 5.33: Vertical displacement *versus* moment load showing peaks and curves

$V' = 48$ N). Figures 5.34(a) and 5.34(b) show the vertical displacement of two tests for the last four and three cycles respectively. The trajectory of the curves follows the sequence illustrated by the arrows, although non-symmetry is visible in Figure 5.34(a) due to the non symmetric loading. Unloading and reloading reproduce the same trajectories but for opposite moment loads. A caisson rocking with increasing amplitude of rotation and far from the parallel point increases its net vertical displacement after each cycle.

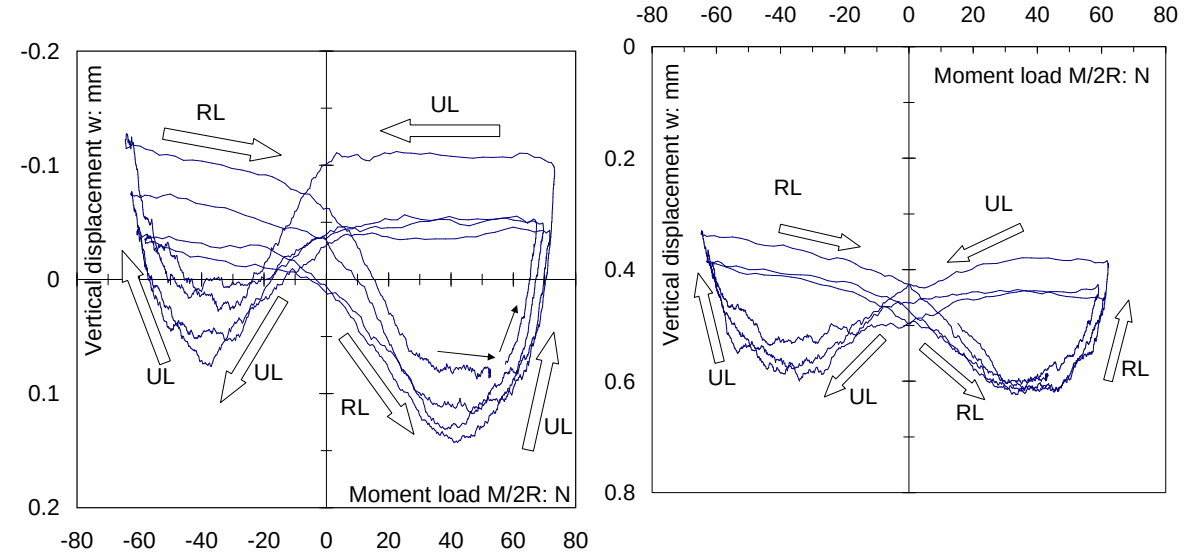

(a) Test FV129_24_3B (b) Test FV117_22_3B

Figure 5.34: Vertical displacement *versus* moment load showing trajectories under reloading RL and unloading UL

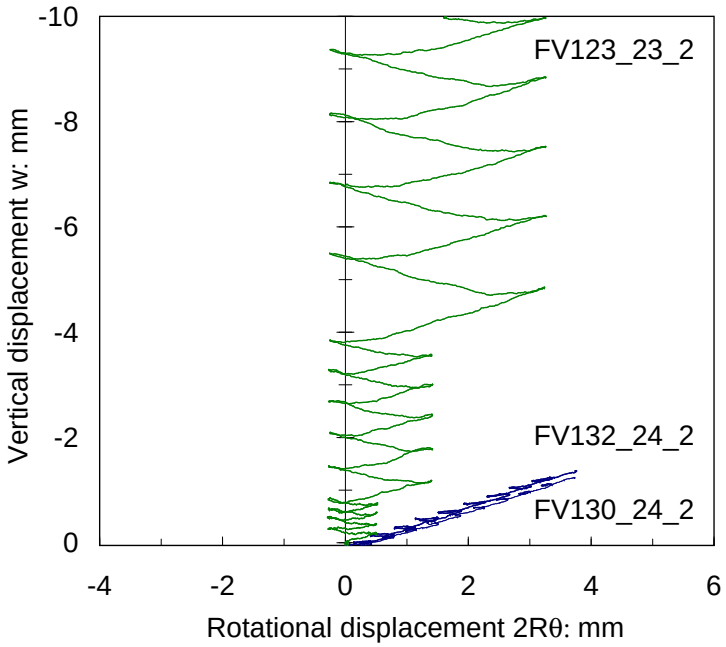

Figure 5.35: Vertical displacement *versus* rotational displacement for tests FV130_24_2, FV132_24_2 and FV123_23_2 with caisson A under $\frac{M}{2RH} = 1$ and $V' = 0$ N

However, if the amplitude of rotation is kept constant, but the caisson increases its tilt in each cycle as shown in Figure 5.30(c) the vertical displacement response resembles a monotonic loading regime. Figure 5.35 shows that despite the large rotation suffered by the caisson under $V' = 0$ N the net vertical displacement is less than -1.5 mm, much less than the -7 mm reached in test FV78_13_2A (Figure 5.33(a)). As mentioned before, this type of loading is more likely to be encountered offshore, therefore, large caisson uplifts due to large rotation amplitudes are less probable to occur under low V'.

5.6 CONCLUSIONS

A series of drained monotonic and cyclic rotational and translational tests under constant vertical load were carried out using model caissons in loose, dry sand. A combined loading system was applied to caissons of two different aspect ratios to study their behaviour. The results obtained allow expressions for the yield surface and flow rule to be established within hyperplastic models.

5.6.1 Monotonic moment capacity

The highest foundation resistance was found for moment and horizontal loads applied in opposite directions for a load ratio around -0.5. However, for design purposes the worst loading condition was found for moment and horizontal loads having the same direction of application. In order to investigate a wider loading spectrum it was necessary to study various load ratios.

Moment test results proved that the moment resistance is a function of the vertical load and the caisson aspect ratio. Caisson uplift was observed in tests with low vertical load, diminishing with the increase of the vertical load.

Rotational and translational tests were performed on caissons, including the application of tension loads. It is concluded that a caisson can resist moment loads even under such unfavourable conditions. This evidence was incorporated within the yield surface expression by means of the tension parameter t_o.

The yield surface formulation can capture appropriately the measured yield points at low vertical loads by including the tension parameter t_o. In addition, the caisson thickness ratio was found to affect the yield surface parameter values. The use of the plastic metacentre decouples the moment and horizontal loads, which eliminates the eccentricity bias when comparing the yield surface dimension parameter h_o.

Related to the flow rule, it was found that an associated flow rule can describe incremental rotational and horizontal displacements, but a non-associated flow rule was necessary for the appropriate description of vertical displacement increments. Additional tests would be required in case of studies with high vertical loads to determine the parameter a_{V_2} and also the yield surface parameter β_2.

5.6.2 Cyclic moment capacity

From the analysis of cyclic moment loading, it was possible to note more clearly the effect of the vertical load on the moment capacity. A higher moment resistance was obtained when the vertical load was increased in a similar way as with monotonic loading. However, the caisson upward movement was found not to be comparable with that obtained from monotonic tests. A much larger uplift of the caisson was observed for very low vertical loads. However, the caisson reached a transition state where no further uplift occurred and settlement developed instead. This transition state was referred as the parallel point and was found to be at values of $\frac{V'}{V_o} = 0.13$ and 0.10 for caisson aspect ratios of 0.5 and 1 respectively. However, results from the monotonic moment loading tests suggest a value of $\frac{V'}{V_o} \approx 0.3$.

Cyclic tests proved to obey the Masing's rules, which has important implications in modelling. In addition, monotonic tests can be used to construct a backbone curve according to comparisons with cyclic tests under similar conditions. Stiffness degradation during each cycle was observed. The secant shear modulus G diminished with the increase in rotation and horizontal displacement respectively.

Further investigation is necessary to include the effect of caisson installation by suction on the monotonic and cyclic moment response. In particular, the study of partially drained and undrained conditions to assess how the pore fluid pressure may affect or not the caisson loading response.

From the yield surface determined multiple yield surfaces of different sizes can be generated to model monotonic or cyclic behaviour. A preliminary study using a hyperplastic model with one yield surface and isotropic hardening showed that the modelling of the incremental response was sensitive to the association factors. Further parametric studies are necessary to calibrate and validate hyperplastic models.